

LIGHTNING AND IONOSPHERIC REMOTE SENSING
USING VLF/ELF RADIO ATMOSPHERICS

A DISSERTATION

SUBMITTED TO THE DEPARTMENT OF ELECTRICAL ENGINEERING

AND THE COMMITTEE ON GRADUATE STUDIES

OF STANFORD UNIVERSITY

IN PARTIAL FULFILLMENT OF THE REQUIREMENTS

FOR THE DEGREE OF

DOCTOR OF PHILOSOPHY

By

Steven Andrew Cummer

August 1997

© Copyright 1997
by
Steven Andrew Cummer

I certify that I have read this thesis and that in my opinion it is fully adequate, in scope and in quality, as a dissertation for the degree of Doctor of Philosophy.

Umran S. Inan
(Principal Adviser)

I certify that I have read this thesis and that in my opinion it is fully adequate, in scope and in quality, as a dissertation for the degree of Doctor of Philosophy.

Timothy F. Bell

I certify that I have read this thesis and that in my opinion it is fully adequate, in scope and in quality, as a dissertation for the degree of Doctor of Philosophy.

Albert Macovski

Approved for the University Committee on Graduate Studies:

Dedication

To my parents
Reid and Julie
and to my wife
Catharine

Abstract

Lightning discharges radiate the bulk of their electromagnetic energy in the Very Low Frequency (VLF, 3–30 kHz) and Extremely Low Frequency (ELF, 3–3000 Hz) frequency ranges. This energy, contained in impulse-like signals called radio atmospherics or sferics, is guided for long distances by multiple reflections from the ground and lower ionosphere. These two facts suggest that observed sferic waveforms radiated from lightning and received at long distances (>1000 km) from the source stroke contain a great deal of information about both the state of the ionosphere along the propagation path and the dynamics of the current in the lightning return stroke. The aim of this dissertation is to develop and implement the necessary techniques to use sferic observations to determine the characteristics of the ionosphere and lightning.

In order to accurately interpret observed sferic characteristics, a detailed model of sferic propagation is required. Such a model is developed, based on a frequency-domain subionospheric VLF and ELF propagation code, and with it the detailed spectral characteristics of VLF (>1.5 kHz) sferics are shown to depend primarily on the propagation-path-averaged ionospheric D region electron density profile, in the range of electron densities of 10^0 – 10^3 cm^{-3} . To infer this D region density from VLF sferic observations, a model ionosphere is iteratively varied to find the model spectrum that agrees best with an observed sferic spectrum composed of the average of many individual sferic spectra. In most nighttime cases, the quality of the agreement allows the height of an exponentially-varying electron density profile to be inferred with a precision of 0.2 km.

Since the general sferic waveform depends on the source current-moment waveform as well as the ionospherically-controlled propagation, the former quantity can

be measured for individual discharges from observed sferics. Of particular interest are those lightning discharges associated with mesospheric optical emissions known as sprites. Earlier work has shown that sprite-producing discharges contain large amplitude, slowly-varying current components, which can transfer a great deal of charge from the cloud to the ground. This result agrees with existing theories in which sprites are directly or indirectly created by large quasi-static electric fields produced by large vertical charge movements.

In this work, the vertical charge-moment change in sprite-producing discharges is measured quantitatively. By using a robust deconvolution technique, source current-moment waveforms are extracted from individual observed ELF (<1.5 kHz) sferics and a modeled ELF propagation impulse response. The source current-moment waveforms over the first 10 ms of the discharge were inferred from 15 different sprite-producing sferics. The majority of these discharges involved smaller total charge-moment changes than predicted by the runaway electron model of sprite production, while two examples studied in detail show that low altitude (~ 60 km) optical emissions are produced with a smaller vertical charge-moment change than predicted by the quasi-electrostatic heating model of sprite production. One of these two cases also showed a charge-moment change insufficient to create optical emissions by the runaway electron model, which suggests that mechanisms not considered in these models may play a role in sprite production.

Acknowledgments

There are many people without whom this work would not have been possible. The support and assistance of my adviser Umran Inan and my associate adviser Tim Bell have been pivotal, and they both deserve many thanks. I would also like to thank Professor Robert Gray for chairing my orals committee, Professor Howard Zebker for serving on my orals committee, and Professor Albert Macovski for generously agreeing to be the third reader for my dissertation on short notice. Tony Fraser-Smith deserves thanks for allowing us the use of his ELF/VLF radiometer for our VLF and ELF recordings. Dr. F. Perry Snyder of NCCOSC/NRaD generously provided assistance in my attempts to modify the LWPC model to do what I needed it to do.

My tenure in the VLF group has lasted almost 6 years. Because the number of people with whom I've interacted is large enough that I know I would forget a few were I to try to thank each individually, I'd like to issue a bulk thank you to everyone. I owe extra thanks to Jerry Yarbrough and Bill Trabucco for their help with the acquisition and analysis of the Stanford VLF/ELF Radiometer data, and to Steve Reising for data analysis help and for obtaining data from the National Lightning Detection Network. Chris Barrington-Leigh's expertise and assistance with the video observations has been invaluable. Victor Pasko provided lots of help in my attempts to compare the observations in my thesis to theoretical predictions. Mike Johnson deserves credit for pointing me to the deconvolution method used in this work and for general hardware help, and Dave Lauben has provided lots of assistance on the software side.

Special thanks go to my wife, Catharine, who has been especially patient during the past three weeks while I wrote the bulk of this dissertation, and whose circadian

rhythm has been about three hours out of phase with mine, temporarily reducing the amount of time we spend together to far less than either of us would like.

My parents, Reid and Julie, made many sacrifices over the years that have allowed me to achieve what I have achieved. I owe most of it to them.

Steve Cummer

This research was supported by the Office of Naval Research through grants N00014-93-1-1201 and N00014-95-1-1095, by the Air Force Office of Scientific Research through grant F49620-97-1-0468, and by the Air Force Phillips Laboratory through grant F19628-96-C-0149.

Contents

Dedication	iv
Abstract	v
Acknowledgments	vii
1 Introduction	1
1.1 Radio Atmosphericics	2
1.2 The Ionosphere	4
1.3 Lightning and Sprites	6
1.4 Contributions	9
2 Electromagnetic Wave Propagation in the Earth-Ionosphere Waveguide	11
2.1 Simplified View of Propagation of Transient Pulses in a Waveguide	11
2.2 Wave Propagation in a Cold Plasma	15
2.3 VLF/ELF Propagation Theory	17
2.4 Budden's Waveguide Theory	18
2.4.1 Derivation of Budden's Theory	18
2.4.2 Correction for Spherical Earth	22
2.4.3 Excitation and Height-Gain Functions	23
2.5 Implementation in LWPC	25
2.5.1 PRESEG	26
2.5.2 MODEFNDR	26

2.5.3	FASTMC	27
2.6	Parameters of the Sferic Propagation Model	27
2.6.1	Ionospheric Electron Density	28
2.6.2	Ionospheric Collision Frequency	28
2.6.3	Lightning Return Stroke Waveform	30
2.7	Sample Calculation	31
2.7.1	Sferic Spectrum	31
2.7.2	Sferic Waveform	34
3	<i>D</i> Region Measurements using VLF Sferics	36
3.1	VLF Sferic Observations	37
3.1.1	Sample VLF Sferics	37
3.1.2	Data Acquisition	41
3.2	Theoretical Effects of Ionospheric Parameters on VLF Propagation	42
3.2.1	Electron Density Profile	43
3.2.2	Minimum and Maximum Electron Density	48
3.2.3	Positive and Negative Ions	51
3.2.4	Ionospheric Inhomogeneities	53
3.2.5	Collision Frequency Profile	55
3.2.6	Ground Altitude	58
3.3	Description and Example of <i>D</i> Region Measurement Technique	59
3.3.1	Noise Reduction with Late-Time Filtering	62
3.3.2	Sferic Averaging Procedure	62
3.3.3	Spectrum Matching Procedure	64
3.4	Two Case Studies	71
3.4.1	Simultaneous, Multiple Location Ionospheric Measurements	71
3.4.2	Ionospheric Measurements During Sunset	75
4	Lightning Current-Moment Measurements	80
4.1	Measurement Technique	82
4.2	ELF Sferic Observations	84
4.2.1	Data Acquisition	84

4.2.2	Removal of Power Line Interference	85
4.3	Modeling the ELF Impulse Response	87
4.3.1	The Dependence of QTEM-Mode Propagation on the E and F Region Electron Density Profiles	87
4.3.2	Choosing the Right ELF Impulse Response	89
4.3.3	Filtering the ELF Impulse Response	90
4.4	Deconvolution	93
4.4.1	Technique	93
4.4.2	Deconvolution Tests	97
4.5	Current-Moment Waveforms Extracted from Sprite-Producing Sferics	103
4.5.1	Sprite-Producing Discharge at 04:09:19.536 UT	103
4.5.2	Sprite-Producing Discharge at 05:31:30.109 UT	105
4.5.3	Sprite-Producing Discharge at 05:25:17.063 UT	106
4.5.4	Charge-Moment Change in 15 Sprite-Producing Discharges . .	108
5	Summary and Suggestions for Future Work	113
5.1	Summary	113
5.2	Suggestions for Further Work	116
5.2.1	Inhomogeneous VLF Propagation Modeling	116
5.2.2	Sferic-Based Detection of Ionospheric Disturbances	117
5.2.3	Fast Lightning Current Measurements	119
5.2.4	E Region Ionospheric Measurements from ELF Sferics	119
5.2.5	More Refined D Region Measurements	120
A	Numerical Inverse Fourier Transform	121

List of Tables

2.1	Receiver excitation functions for 4 output field components.	25
3.1	Four sferic source regions and the return stroke parameters used to calculate the modeled spectra.	71
4.1	Video time and NLDN-recorded characteristics of 15 sprite-producing discharges.	110

List of Figures

1.1	Variation of ionospheric electron density and neutral atmospheric temperature with altitude.	5
2.1	Time domain analysis of propagation in a simple waveguide.	13
2.2	Frequency domain analysis of propagation in a simple waveguide.	15
2.3	Coordinate system for the waveguide and demonstration of equivalent image source.	20
2.4	Normalized height-gain functions for two different modes at 10 kHz.	24
2.5	A representative midlatitude nighttime electron density profile.	28
2.6	Electron-neutral and ion-neutral (both positive and negative) collision frequency profiles.	29
2.7	The model lightning current-moment waveform and amplitude spectrum.	32
2.8	Modeled sferic amplitude spectrum from 0-40 kHz.	33
2.9	Modeled sferic waveform.	34
3.1	Spectrogram and waveform of a representative large sferic.	39
3.2	Unusual sferics received at Stanford on July 24, 1996.	40
3.3	Measured impulse response and frequency response of anti-aliasing filter in the data acquisition system.	42
3.4	A comparison of sferic spectra for two nighttime ionospheres with different values for h'	45
3.5	A comparison of sferic spectra for two nighttime ionospheres with different values for β	46
3.6	A comparison of sferic spectra for three different daytime ionospheres.	47

3.7	Theoretical sferic spectra demonstrating the effect of nighttime N_e^{min} and N_e^{max} on VLF sferic propagation.	50
3.8	Theoretical sferic spectra demonstrating the effect of daytime N_e^{min} and N_e^{max} on VLF sferic propagation.	51
3.9	Theoretical sferic spectra demonstrating the effect of ions on nighttime VLF sferic propagation.	52
3.10	A comparison of homogeneous and inhomogeneous sferic propagation.	54
3.11	Another comparison of homogeneous and inhomogeneous sferic propagation.	56
3.12	Two sferic spectra demonstrating the effect of a factor of two collision frequency increase on nighttime VLF sferic propagation.	57
3.13	Two sferic spectra demonstrating the effect of a factor of two collision frequency increase on daytime VLF sferic propagation.	58
3.14	Map showing the sferic receiver location (Stanford) and the lightning source region on July 22, 1996, 0415-0445 UT.	60
3.15	Typical large and small sferic waveforms and spectra from lightning discharges on July 22, 1996.	61
3.16	Demonstration of >10 kHz noise reduction using late-time filtering.	63
3.17	Examples of acceptable and unacceptable sferic onsets.	65
3.18	Average sferic waveform and spectrum calculated from 59 individual sferics.	66
3.19	Demonstration of spectral detail extraction.	68
3.20	Extraction of ionospheric parameters from measured spectral details.	69
3.21	Final agreement between theory and observation.	70
3.22	Observed and best fit theoretical sferic spectra on July 22, 1996 from 0415-0445 UT.	73
3.23	Multi-location ionospheric measurement.	74
3.24	Map of propagation path and day-night terminator location on May 25, 1997.	76
3.25	Evolution of observed average sferic spectrum on a single propagation path as the terminator moves west across the path.	77

3.26	Single-location ionospheric measurement.	79
4.1	Frequency response of filter used to remove all non-QTEM sferic components.	84
4.2	Noise removal from ELF sferics.	86
4.3	Demonstration of dependence of ELF impulse response on the ionosphere.	88
4.4	Determining the E and F region electron density profile at 04:37:32.532 UT.	91
4.5	Determining the E and F region electron density profile at 05:24:48.110 UT.	92
4.6	Outline of the CLEAN algorithm.	95
4.7	Testing the CLEAN-based deconvolution with a known slow source current.	98
4.8	Testing the CLEAN-based deconvolution with a known fast source current.	99
4.9	Testing the CLEAN-based deconvolution with a known nearly-constant source current.	100
4.10	The theoretical step response of the ELF propagation system, including the high-pass filter described in Section 4.3.3.	102
4.11	Observed sprite and sferic on July 24, 1996, at 04:09:19.536 UT. . . .	104
4.12	Observed sprite and sferic on July 24, 1996, at 05:31:30.109 UT. . . .	107
4.13	Observed sprite and sferic on July 24, 1996, at 05:25:17.063 UT. . . .	109
4.14	Extracted cumulative charge-moment change over 10 ms in 15 sprite producing discharges.	111
5.1	Sferic measurements which indicate a strongly inhomogeneous ionosphere.	118
A.1	Demonstration of approximation of smooth spectrum by a sum of piecewise-linear pulse pairs.	122

Chapter 1

Introduction

Radio atmospherics are the electromagnetic signals launched by individual lightning discharges. Lightning radiates electromagnetic energy over an extremely wide bandwidth, from a few Hz [Burke and Jones, 1992] to many tens of MHz [Weidman *et al.*, 1986]. However, because of the time scales and spatial extent of the radiating current, most of this energy is radiated in the Very Low Frequency (VLF, 3–30 kHz) and Extremely Low Frequency (ELF, 3–3000 Hz) bands. VLF and ELF energy radiated near the ground does not spread out as though it were propagating in free space; rather, it is reflected by the conducting region of the atmosphere known as the ionosphere and by the ground. The radiated ELF/VLF energy thus propagates in a guided fashion between these two boundaries, which form what is known as the Earth-ionosphere waveguide. This guided propagation occurs with low attenuation rates at VLF and ELF frequencies (a few dB per 1000 km), allowing VLF and ELF radio atmospherics (or sferics, for short) to be observed literally around the world from a single source lightning discharge. The characteristics of individual sferics observed at a given site are thus controlled by the source lightning discharge and the propagation effects introduced by the Earth-ionosphere waveguide. This dissertation focuses on using observed sferics to extract information about both of these factors.

1.1 Radio Atmospherics

The early days of sferic research, from the 1930's to the 50's, were primarily a period of discovery. An excellent early paper on sferics was produced by *Burton and Broadman* [1933], whose VLF observations uncovered two distinct emissions, which they classified based on their apparent sound when played on a loudspeaker as “swishes” and “tweeks”. Through a dynamic spectral analysis, they showed the difference in dispersion characteristics between the two signals. The “tweek” waveform showed a sharp frequency cutoff and long tail near 1.7 kHz, and Burton and Broadman correctly attributed this feature as being the result of propagation of a transient signal launched from the ground and propagating in a waveguide with an upper boundary altitude from 61–85 km (depending on the time of day) which determines the observed cutoff frequency. Their “swishes” are what are now referred to as “whistlers” [*Helliwell*, 1965], which were reported earlier by *Barkhausen* [1930] and *Eckersley* [1925]. Burton and Broadman realized, however, that one of Barkhausen's theories for the production of whistlers (repeated reflection from an ionospheric boundary) was in fact the proper mechanism for tweeks. The correct theoretical explanation for whistlers would not be published until much later by *Storey* [1953], who proposed that they are VLF signals radiated by lightning that have propagated over extremely long distances through the Earth's magnetosphere and have been strongly dispersed by the nature of electromagnetic propagation in this ionized medium.

After the origin of sferics (and tweeks) was established, research focused on the variability of sferic waveforms, in which the occurrence rates of different sferic classes were studied as functions of time of day, arrival bearing, and propagation distance [e.g. *Horner and Clarke*, 1955; *Chapman and Pierce*, 1957]. At the same time, there was a great deal of interest in understanding the details of VLF propagation in the Earth-ionosphere from the practical standpoint of long-distance communication. Transatlantic transmissions at frequencies under 100 kHz were in fairly common use by the onset of World War I [*Watt*, 1967, p. 120]. However, the exact nature of the upper waveguide boundary was not well understood at the time. While fixed, man-made transmitters were put to good use in studying VLF propagation [e.g. *Bracewell*

et al., 1951], sferics were also used to study propagation over a wide frequency range. *Chapman and Marcario* [1956] determined mean attenuation rates for VLF propagation as a function of frequency from observations of sferics from different source ranges, which showed multi-mode propagation behavior for frequencies above ~ 1.5 kHz. *Jean et al.* [1960] and *Taylor* [1960] used observations of the same sferic at different locations to study VLF attenuation rates and phase characteristics, respectively. There were some early efforts to measure the reflection height of the lower ionosphere from observations of tweeks with very well-defined tail pulses [*Mallinckrodt*, 1949], but this technique could only be applied to a small subset of observable sferics.

There has been comparatively little recent work with VLF sferics. Some work has focused on measurements and theoretical understanding of the long-delayed sferic components which form the “tweek” [*Yamashita*, 1978; *Ryabov*, 1992; *Yedemsky et al.*, 1992]. Other research has used measured sferics to determine the distance and geographic bearing to the source discharge and to estimate the ionospheric reflection altitude along the propagation path [*Kumar et al.*, 1994; *Hayakawa et al.*, 1994; *Hayakawa et al.*, 1995]. *Rafalsky et al.* [1995] employed a technique similar to that used in this dissertation to infer the effective ionospheric reflection height from sferic observations, but the precision of the method was somewhat limited by the fact that the precise source locations were not known (although the distance was also inferred using the same sferic observations).

The theoretical and experimental study of the propagation of ELF sferics, though fundamentally similar to VLF sferic propagation, generally has been treated separately in the literature. *Jones* [1974] published an extensive bibliography of experimental measurements of ELF propagation characteristics using natural sources (primarily lightning). One study not in this bibliography that merits mention is *Hepburn* [1955], which is a comprehensive experimental study of ELF “slow-tail” waveforms, so called because of their temporal separation from the VLF portion of the sferic due a slower group velocity for the ELF frequency components [*Wait*, 1962; *Sukhorukov*, 1992]. Recent work in this area by *Burke and Jones* [1992] used measurements of sferics below 50 Hz to deduce ELF propagation parameters for these frequencies.

1.2 The Ionosphere

The ionosphere is defined as the region of the atmosphere where, through various ionizing processes, there exist a significant number of free electrons and ions. It is the presence electrons and ions which effectively make the ionospheric medium a conductor which reflects VLF and ELF waves propagating in the Earth-ionosphere waveguide.

Figure 1.1 shows a typical altitude distribution of free electrons in the ionosphere for both day and night. The altitudes of the atmospheric regions defined by their neutral temperature are also shown for comparison. As shown in the figure, the ionosphere is divided into regions commonly designated the *D*, *E*, *F1*, and *F2* regions. Different wavelengths of solar radiation (from ultraviolet to X-rays) are the source of many of the free electrons during daytime [Hargreaves, 1992, p. 222], which explains the significant difference between the daytime and nighttime ionosphere. Non-solar ionizing sources, such as precipitating energetic electrons, meteoric ionization, and cosmic rays, maintain the free electron concentration at night [Hargreaves, 1992, p. 231].

The ionosphere is far from static, and the study of ionospheric dynamics through various means is a major component of space science. Because of the varying altitudes and electron densities of the ionospheric regions, different techniques are capable of probing the different regions. Swept-frequency pulse sounding, called an ionosonde, was the first technique employed and is still used today [Hargreaves, 1992, p. 61]. Under optimal conditions, the delay in the reflected signal as a function of frequency gives an almost direct measure of the electron density as a function of altitude. Ionosondes can probe the *E* and *F* regions, but no echo is produced at the lower frequencies (<500 kHz) required to probe the lower electron densities in the *D* region [Rishbeth and Garriott, 1969, p. 58].

A more recently developed (though still almost 40 years old) ionospheric measurement technique is incoherent scatter radar (ISR) [Evans, 1969]. Unlike an ionosonde, it can probe the ionosphere above the *F2* region electron density maximum, and it is also capable of measuring quantities other than the electron density, such as ion and electron temperatures [Evans, 1969]. However, since incoherent scatter radar returns

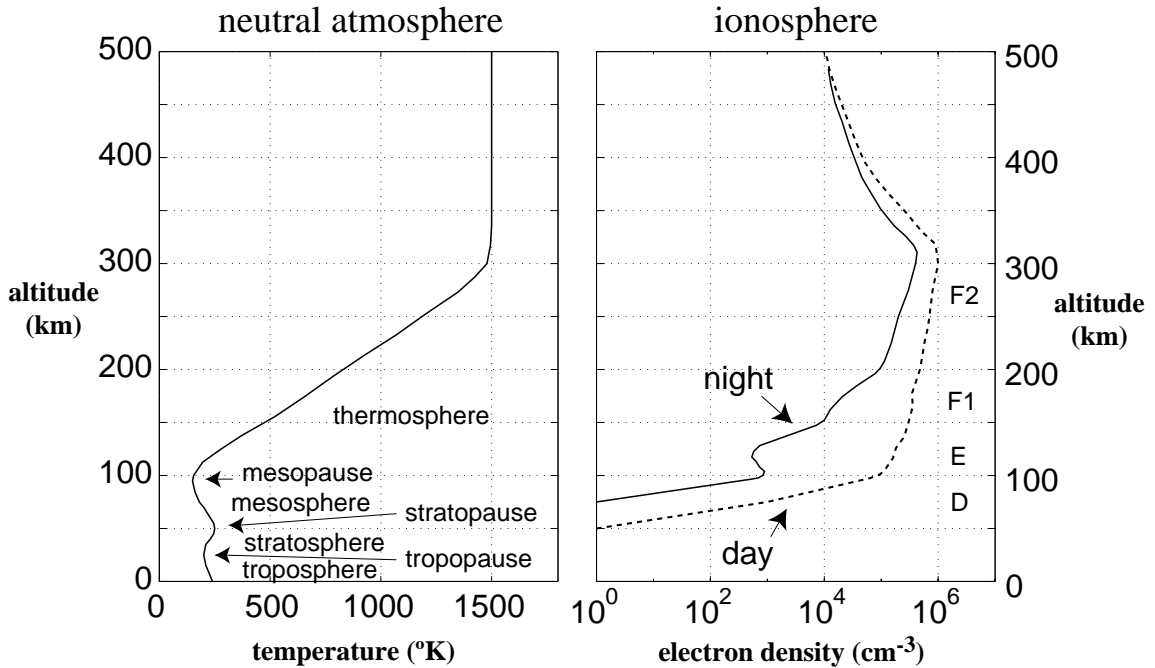


Figure 1.1: Typical variation of ionospheric electron density and neutral atmospheric temperature with altitude (adapted from *Hines et al.* [1965, p. 6]).

are rather weak, a high-power transmitter, large antenna, and sophisticated signal processing are required for the measurement, making such a facility large and expensive [Hargreaves, 1992, p. 81]. It is also difficult to measure electron densities below $\sim 10^2 \text{ cm}^{-3}$ using ISR [Mathews et al., 1982].

Measurements of the *D* region ($\sim 60\text{--}90 \text{ km}$) electron density are difficult to make. The usual radio techniques (i.e. ionosonde and ISR) do not work well, and the region is too low for satellites yet too high for balloons. A convenient summary of *D* region measurement techniques can be found in Sechrist [1974]. Rockets can be used either with Langmuir probes to make in-situ electron density measurements or with HF transmitters, the signals from which are received on the ground and used to infer the electron density of the medium through which the signals propagated [Mechtly et al., 1967]. A method similar to this rocket radio technique is the partial reflection technique, in which vertically-incident MF or HF signals launched from the

ground are reflected by irregularities in the D region, and based on the wave characteristics of the reflected signal the electron density profile of the medium can be obtained [Belrose and Burke, 1964]. The fact that VLF waves are almost completely reflected by the D region makes them a useful tool for measuring electron densities in this altitude range. Steep and oblique incidence VLF and LF radio wave reflection data has been inverted to derive D region electron density profiles [Deeks, 1966; Thomas and Harrison, 1970].

In this work, a D region measurement technique is developed using long-distance VLF propagation effects measured in sferics. The D region is the upper boundary of the Earth-ionosphere waveguide, and sferic characteristics thus contain information about this boundary. This sferic technique is significantly different from those mentioned above in that it is not a point measurement; rather, it is sensitive to the average electron density profile across the entire path, making it uniquely capable of large-scale measurements. In a similar manner, single frequency VLF propagation measurements have been used to estimate D region electron density parameters along a given propagation path [Bickel *et al.*, 1970; Thomson, 1993].

1.3 Lightning and Sprites

There are many individual processes involved in a single lightning discharge, not all of which are well understood. For the purposes of this work, the most important process is the return stroke of a cloud-to-ground (CG) lightning discharge (as opposed to an intra-cloud discharge), which occurs after a conducting channel (typically greater than 1 km in length) has electrically connected the ground and the charge in the cloud. It is the electrical current in the return stroke which is responsible for the transfer of charge from cloud to ground and for the radiation of the VLF and ELF sferics that form the basis of this dissertation. Typical current rise times of $\sim 8 \mu\text{s}$ and fall times of $\sim 500 \mu\text{s}$ which have been observed for negative CG discharges [Berger *et al.*, 1975] are responsible for the radiation in the VLF and ELF bands, and occasional “continuing currents” have been observed to last longer than 40 ms [Brook *et al.*, 1962]. For a thorough discussion of lightning processes and phenomenology, see Uman [1987].

The possibility of electrical discharges at high altitudes above thunderstorms was proposed long ago [Wilson, 1925], but their existence was not confirmed until recently when an image of an apparent above-thunderstorm discharge was captured on video [Franz *et al.*, 1990]. Since then, there has been an explosion of research in optical and radio measurements and theoretical modeling of these mesospheric optical emissions known as sprites [Lyons, 1996]. Proposed generation mechanisms for sprites include heating of ambient electrons by quasi-electrostatic (QE) thundercloud fields [Pasko *et al.*, 1997], runaway electron processes driven by the same QE fields [Bell *et al.*, 1995b; Roussel-Dupre and Gurevich, 1996; Taranenko and Roussel-Dupre, 1996; Lehtinen *et al.*, 1997], and heating by lightning electromagnetic pulses [Milikh *et al.*, 1995].

Sprites are observed in association with only a subset of intense cloud-to-ground lightning discharges [Boccippio *et al.*, 1995], in particular those discharges which radiate a large amount of electromagnetic energy in the ELF ($\lesssim 1.5$ kHz) range, indicative of continuing currents lasting over time scales of at least a few ms [Reising *et al.*, 1996]. This fact is in general agreement with both the QE and runaway models, in which rapid and large charge transfer during the discharge creates large quasi-electrostatic fields at ionospheric altitudes, thereby creating the optical emissions by heating the electrons or by initiating the upward runaway electron avalanche. Both of these processes are highly nonlinear and predict a threshold level for the charge-moment change in the lightning discharge necessary to create optical emissions. In the QE model, this threshold depends somewhat on the initial charge configuration in the cloud and on the ambient ionospheric electrical conductivity, but a minimum charge-moment transfer of 1000 C·km to create optical emissions at 75 km altitude is consistent with the theory [Pasko *et al.*, 1997]. A significantly smaller charge-moment change is necessary for optical emissions at higher altitudes, but even more is required for emissions at lower altitudes.

The charge-moment transfer required to produce significant optical emissions by the runaway electron process is less clear. In the work of Roussel-Dupre and Gurevich [1996] and Taranenko and Roussel-Dupre [1996], conductivity gradients in the vicinity of the cloud are neglected, which produces much higher electric fields in this region,

thereby allowing the runaway process to create significant optical emissions with less total charge-moment transfer than if this conductivity were accounted for. These two studies respectively show optical emissions consistent with observations with charge-moment transfers of 1800 C·km in 10 ms and 1350 C·km in 5 ms. The treatment by *Lehtinen et al.* [1997] accounts for conductivity gradients near the cloud, which shows that 2250 C·km of charge-moment transfer in 1 ms is required to create significant runaway-related optical emissions.

Quantitative measurements of the actual vertical charge-moment transfer in sprite-producing discharges are needed to test the validity of these models. Most measurements of charge transfer in lightning return strokes have been made by directly measuring current when lightning strikes an instrument tower [*Berger et al.*, 1975] or an electrically-grounded rocket [*Hubert et al.*, 1984], and from multi-site electrostatic field measurements [*Krehbiel et al.*, 1979]. The difficulty in these measurements is a matter of practical placement of the sensors; direct rocket or tower observations must be made at the location of the lightning, and electric field observations must be made at most a few tens of kilometers from the charge center due to the rapid decay of the static component of the dipole electric field. Local measurements such as these would be difficult in the case of sprites, as their occurrence location and time are not known in advance.

Measurements of the vertical charge-moment change in sprite-producing discharges were first published by *Cummer and Inan* [1997], who compared predictions of the radiated fields at a remote site (~ 2000 km distant) with direct observations of ELF sferics launched by these discharges. The work presented in this dissertation is a slightly modified and improved version of this technique, in which the observed ELF sferics are deconvolved with a modeled ELF impulse response for propagation along the known sferic path to obtain the source current-moment waveform. *Burke and Jones* [1996] used a similar technique to infer the source current-moment waveform in lightning discharges from observed ELF sferics. However, their observations were limited to a frequency range of 5–45 Hz, limiting their measurements to only the slowest components of the source current, which are slower than many of those of

interest for the issue of sprite production. A specific functional form for the current-moment was assumed in the work of *Burke and Jones* [1996], while the deconvolution technique used in this work allows for a completely arbitrary waveform.

1.4 Contributions

The contributions of this dissertation are as follows:

- A model of VLF and ELF radio atmospheric propagation is developed, which is based on existing frequency-domain propagation models. This model incorporates a completely general anisotropic ionosphere, arbitrary source lightning orientation, arbitrary source lightning altitude, and arbitrary output field component.
- Based on this propagation model and VLF sferic observations, a new (and currently the only) technique for measuring large scale, propagation path-averaged electron densities in the nighttime *D* region (~ 70 -90 km) is developed. The agreement between modeled and measured sferic spectra is found to be quite good in many cases, allowing the extraction of the height (relative to the ground altitude) of a path-averaged exponential electron density profile to an accuracy of better than 0.2 km.
- Based on this propagation model and ELF sferic observations, a technique to infer the source current-moment waveforms (on time scales less than approximately 0.5 ms) in individual lightning strokes from ELF (~ 10 -1500 Hz) sferics is developed. This measurement is used to quantify the total vertical charge-moment change in cloud-to-ground lightning strokes which produce mesospheric-altitude optical emissions known as sprites. The majority of these discharges contained a smaller total charge-moment change than predicted by the runaway electron model of sprite production, while two examples studied in detail show that low altitude (~ 60 km) optical emissions are produced with a smaller charge-moment change than predicted by the quasi-electrostatic heating

model of sprite production. One of these two cases also showed a charge-moment change insufficient to create optical emissions by the runaway electron models, which suggests that mechanisms not considered in these models may play a role in sprite production.

Chapter 2

Electromagnetic Wave Propagation in the Earth-Ionosphere Waveguide

The basis for all of the work presented in this thesis is the measurement and modeling of the characteristics of electromagnetic wave propagation in the Earth-ionosphere waveguide. In order to infer lightning return stroke current waveforms and ionospheric *D* region electron densities as accurately as possible, the fundamental sferic observations must be interpreted using a sferic propagation model which is as realistic as possible, one in which all significant effects involved in the propagation are included.

In this chapter, the mathematical description of propagation in a general waveguide is developed and applied to the Earth-ionosphere waveguide, and the methods for inclusion of the different factors are discussed.

2.1 Simplified View of Propagation of Transient Pulses in a Waveguide

A simple, non-rigorous examination of transient propagation in a waveguide provides physical insight that is particularly useful in interpreting solutions obtained from a rigorous formulation of propagation in the Earth-ionosphere waveguide. In this analysis, many physical effects are ignored for the sake of simplicity. These details

are fully addressed in the complete theoretical model in Section 2.4.

The simple waveguide considered here is taken to be two-dimensional and planar, with perfectly reflecting walls separated by a distance h . An isotropically-radiating source on the surface of one of the walls is assumed to launch an impulsive signal. The signal detected by a receiver at a distance d from this source can be thought of in either the time domain or in the frequency domain.

In the time domain, the received signal can be thought of as a superposition of a series of rays which travel along straight lines and which reflect multiple times from the waveguide surfaces in traveling from the source to receiver. This concept is displayed in Figure 2.1a. One component of the signal travels directly from the source to the receiver (zero hops), another is reflected once from the upper surface (one hop), yet another is reflected twice (two hops), and so on. Because the rays travel at the speed of light, the propagation time from the source to the receiver of each is simply the total propagation distance r divided by c , the speed of light in free space. The rays with more hops propagate over longer distances and thus arrive later at the receiver. Also, the field strength associated with each ray attenuates as $1/r$, due to energy spreading. Remembering that the source is impulsive, the received signal is then a sequence of impulses, one for each ray. If $d \gg h$, then the first few impulses arrive very close in time, since the distance traveled for these rays is nearly the same. The time difference between the later impulses approaches the round-trip time it takes for a ray to travel vertically up and down the waveguide, or $2h/c$. The waveform of such a signal is shown in Figure 2.1b.

Alternatively, one could solve the same problem of impulsive propagation in a perfectly reflecting waveguide in the frequency domain and synthesize a time-domain solution using the inverse Fourier transform. This method relies on the theory of waveguide mode propagation [Budden, 1961]. At a fixed frequency f , the field in the waveguide can be decomposed into a sequence of independent field structures (i.e. modes) which propagate with different velocities. Each of these modes but one is defined almost completely by its cutoff frequency $f_{cn} = nc/2h$ [Cheng, 1989, p. 535]. If $f > f_{cn}$ for a particular mode, then the mode propagates with a group velocity $v_{gn} = c/\sqrt{1 - f_{cn}^2/f^2}$ which approaches zero as f approaches f_{cn} . If $f < f_{cn}$, then

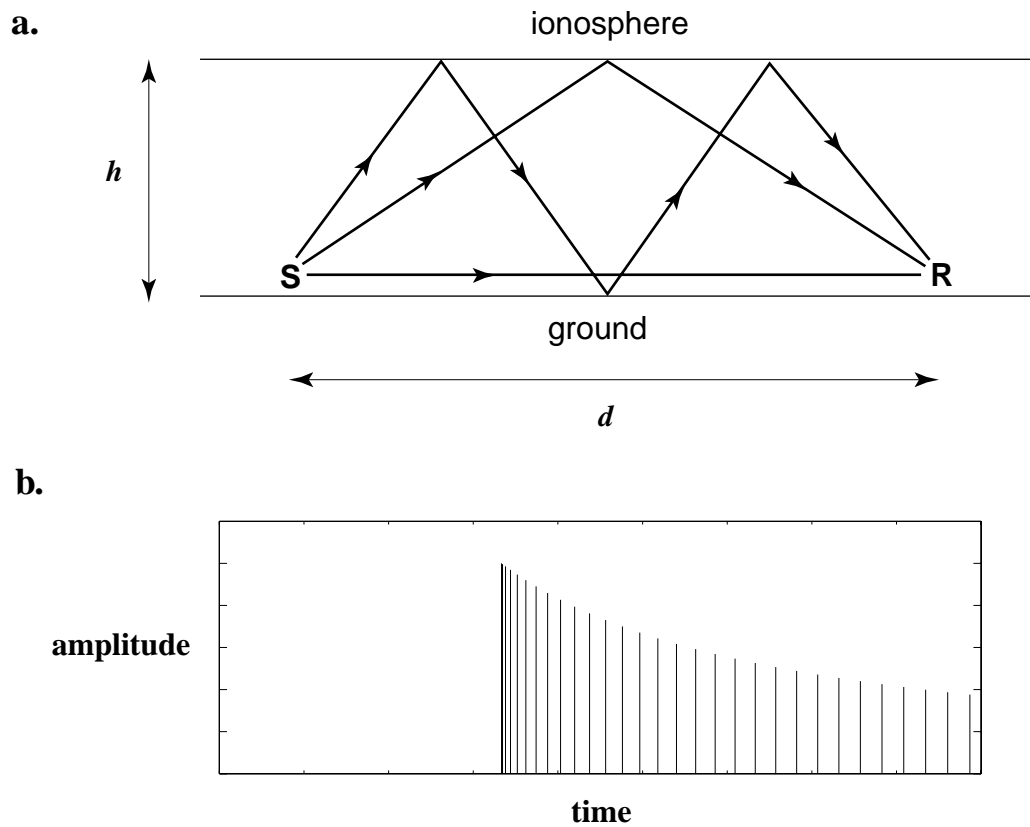


Figure 2.1: Time domain analysis of propagation in a simple waveguide. a: The ray-hop interpretation of propagation from source (S) to receiver (R). b: Sample signal at receiver from impulsive source.

the mode is called evanescent and strongly attenuates with distance from the source in the guide and does not contribute to the signal at the receiver (except when the source and the receiver are very close). In such an electromagnetic waveguide, there are two types of modes associated with each cutoff frequency—the transverse magnetic (TM) and transverse electric (TE) modes, and the single mode with no cutoff frequency is called the transverse electromagnetic (TEM) mode [Cheng, 1989, p. 534]. However, only the TM and TEM modes have a non-zero transverse magnetic field at the boundary surfaces, which is the quantity that is experimentally measured in this

work. For simplicity, we assume in the following example that the signal measurements are made of this transverse magnetic field at the boundary wall so that only the TM and TEM modes need be considered.

Figure 2.2 shows the received signal in a time-frequency representation. The TEM mode, with no cutoff, travels with a velocity c independent of frequency, and all frequencies arrive at the receiver simultaneously. The TM_1 mode does not contribute to the signal at the receiver at frequencies below its cutoff because it is evanescent, but it does contribute above its cutoff frequency. However, the near-cutoff frequency components arrive much later because of their slow group velocity. As the frequency increases further above the TM_1 mode cutoff, the propagation speed approaches the speed of light. Similar behavior can be seen in the other modes, but with a different cutoff frequency for each.

The early-time received signal is composed of a broad range of frequencies, but the late-time signal contains a series of discrete frequency components near the cutoff frequencies f_{cn} because of the low values of v_{gn} for modes near cutoff. In the frequency domain, the spectrum of the late-time signal consists of a set of frequency impulses with a spacing of $c/2h$, which in the time domain correspond to a sequence of impulses with a temporal spacing of $2h/c$. This is qualitatively the late-time signal that was deduced from the ray-hop analysis.

These analyses give us a qualitative idea of what a waveguide impulse response should look like, and they provide insight that is useful in interpreting the more physically complicated cases considered later. Some of the many factors not considered in the preceding discussion are the non-isotropic nature of a real electromagnetic source, the non-perfectly reflecting nature of the boundaries in the Earth-ionosphere waveguide, and the fact that the real Earth-ionosphere waveguide is not bounded by planar surfaces but rather by concentric spherical surfaces. All of these factors are included in the rigorous formulation presented below.

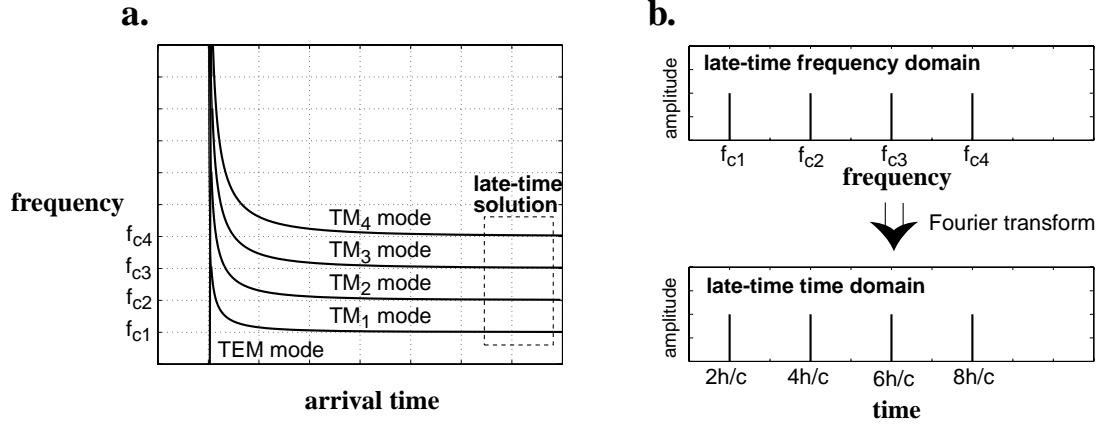


Figure 2.2: Frequency domain analysis of propagation in a simple waveguide. a: Simulated spectrogram of received signal. b: The received late-time waveform constructed from the frequency-domain solution with the Fourier transform.

2.2 Wave Propagation in a Cold Plasma

Before we discuss the mathematical details of guided propagation, it is useful to examine the electromagnetic properties of the ionosphere which makes up the upper boundary of the Earth-ionosphere waveguide. The fields in this medium are described by Maxwell's equations,

$$\nabla \times \mathbf{E} = -\partial \mathbf{B} / \partial t \quad (2.1)$$

$$\nabla \times \mathbf{B} = \mu_0 \epsilon_0 \partial \mathbf{E} / \partial t + \mu_0 \mathbf{J}_{\text{tot}} \quad (2.2)$$

coupled to an equation for current derived from the Lorentz equation of motion of the free electrons and ions in the medium in response to the wave electric field and an ambient static magnetic field [Budden, 1985, p. 45],

$$\partial \mathbf{J}_n / \partial t + \nu_n \mathbf{J}_n = \frac{q_n}{|q_n|} \omega_{Bn} (\mathbf{J}_n \times \mathbf{b}_E) + \epsilon_0 \omega_{pn}^2 \mathbf{E}, \quad (2.3)$$

where ω_{pn} is the plasma frequency for each type of particle (denoted by the subscript n) and is defined by $\omega_{pn} = \sqrt{N_n q_n^2 / m_n \epsilon_0}$, N_n is the number density per unit volume of the particle, q_n is the charge of the particle, and m_n is the mass of an individual

ion or electron. The gyrofrequency ω_{Bn} for each type of particle is defined as $\omega_{Bn} = |q_n \mathbf{B}_E|/m_n$, where \mathbf{B}_E is a static magnetic field, such as that of the Earth. The vector \mathbf{b}_E is defined as the unit vector in the direction of the static magnetic field, or $\mathbf{B}_E/|\mathbf{B}_E|$. The collision frequency ν_n is the rate of inelastic collisions between a single charged particle and neutrally-charged atmospheric molecules, representing the momentum losses due to these collisions. Each of the charged species makes its own contribution to the total current in this way, and the \mathbf{J}_{tot} term in (2.2) is defined as $\mathbf{J}_{tot} = \sum_n \mathbf{J}_n$, where the summation is over all of the positive and negative ion species (including electrons).

By assuming that the fields vary as $e^{i(\omega t - kz)}$ in (2.1)–(2.3), the index of refraction n for plane waves propagating in this medium can be straightforwardly derived [Budden, 1985, p. 75]. The resulting Appleton-Hartree refractive index equation is quite complicated, and because of the cross term from the non-zero \mathbf{B}_E , n in general depends on the direction of wave propagation relative to this static magnetic field, i.e. the medium is anisotropic. However, a number of reasonable approximations can be made to simplify (2.3) under certain circumstances. If $\nu_n \gg \omega$, then the $\nu_n \mathbf{J}_n$ term dominates on the left hand side and the $\partial \mathbf{J}_n / \partial t$ term can be neglected, which has the effect of making the medium simply (but anisotropically) conducting, with $\mathbf{J}_n = \bar{\sigma}_n \mathbf{E}$, where $\bar{\sigma}_n$ is a conductivity tensor given by a 3×3 matrix. If, in addition, $\nu_n \gg \omega_{Bn}$, then the $\omega_{Bn}(\mathbf{J}_n \times \mathbf{b}_E)$ term can also be neglected, and the medium becomes simply (and isotropically) conducting with $\sigma = \epsilon_0 \omega_{pn}^2 / \nu_n$. Also, because the ions are at least 1800 times more massive than electrons (and m_n is in the denominator of the ω_{pn} and ω_{Bn} terms), the ion current terms usually contribute only slightly to the total current and can often be neglected [Budden, 1985, p. 55]. However, at lower frequencies close to the ion plasma- and gyro-frequencies, the effect of ions cannot be neglected.

Implicit approximations were made in the derivation of (2.3). The effect of the wave magnetic field on electron and ion motion is ignored, and the electrons and ions are treated as completely motionless until acted on by the wave electric field, thus any thermal motion of the charged species is ignored (which is why this medium is called a “cold” plasma). These approximations are valid for the low-power wave propagation in the ionosphere considered here. Descriptions of wave propagation in the plasma

medium when these approximations are not applicable can be found in *Rawer* [1993].

2.3 VLF/ELF Propagation Theory

There are three primary mathematical formulations for VLF propagation in the Earth-ionosphere waveguide that are found in the literature, all of which treat the time-harmonic problem of propagation at a single frequency. The primary difference between them is in the treatment of the ionospheric and ground boundaries. J. Galejs developed a clear and concise formulation for the fields of both vertical and horizontal dipole sources in the free space region between two spherical shells [Galejs, 1972, p. 74]. In his formulation, the ionospheric and ground boundaries are described only by impedance boundary conditions which specify the ratios of orthogonal \mathbf{E} and \mathbf{H} fields (thus the fields outside of the free space region are not calculated). This derivation is based on a straightforward solution of the time-harmonic form of Maxwell's equations using the technique of separation of variables [Zauderer, 1989, p. 168]. Various asymptotic expansions of the Legendre polynomials involved lead to a solution for large distances from the source composed of a sum of traveling wave modes [Galejs, 1972, p. 82]. His work assumes a sharply stratified ionosphere (with free space below the interface and a homogeneous ionosphere above), and it is well-known that the real ionosphere is smoothly varying. This deficiency makes the Galejs formulation of little use for problems of the sort to be attacked in this work which require accurate modeling of the ionospheric reflection process.

The work of J. R. Wait on subionospheric VLF and ELF propagation was published in many papers in the 1950's and 1960's, and was conveniently summarized in his book [Wait, 1970]. In his solution for the fields in a free space region between two spherical shells, Wait specifies the conductivity, permittivity, and permeability of the upper and lower boundary regions explicitly (rather than by an impedance boundary condition). He derives a similar Legendre polynomial series solution for the fields in all three media, and by matching the tangential \mathbf{H} and normal \mathbf{E} fields at the two boundaries and through a series of asymptotic expansions and approximations similar to those of Galejs, he obtains the final result for the fields in the free space region as

a sum of traveling wave modes [Wait, 1970, p. 161].

Wait also briefly describes extending this method to the situation where the upper boundary is not a single interface but rather a series of interfaces, thus approximating a smoothly stratified upper boundary [Wait, 1970, p. 183]. However, he assumes that the upper boundary regions are isotropic, which is not the case for the magnetized plasma comprising the ionosphere (as discussed in in Section 2.2).

The theory developed by K. G. Budden [Budden, 1962] is the most general of these three, as it specifies the upper and lower waveguide boundaries in terms of completely general reflection coefficients, so that they can be comprised of any medium, sharply bounded or stratified, or even anisotropic. This work employs the waveguide propagation theory of Budden, which is described in detail below.

2.4 Budden's Waveguide Theory

2.4.1 Derivation of Budden's Theory

Rather than consider a spherical waveguide at the outset, the Budden derivation begins with a flat geometry and subsequently introduces corrections to account for the spherical nature of the Earth-ionosphere waveguide. Consider a vertical electric dipole source of strength Il in free space, radiating at a single frequency ω , located at the origin, and oriented in the z direction. Budden shows that this source is equivalent to an infinite number of line quadrupole sources parallel to the y axis, each of which radiates fields for which the Hertz vector \mathbf{U} (the Hertz vector is, much like the vector potential \mathbf{A} , a vector convenient to use in radiation problems from which \mathbf{E} and \mathbf{H} can easily be recovered [Stratton, 1941, p. 28]) is given by

$$U_z = -\frac{kIl}{8\pi^2\omega} \int_C \exp[-ik(x \cos \theta + z \sin \theta)] \cos \theta d\theta, \quad (2.4)$$

where θ is the angle in the x - z plane relative to the x axis. In this way, the waveguide problem for a single line quadrupole source can be solved, and the total solution for a point dipole can then be reconstructed by the appropriate integration of the line quadrupole fields.

Consider a general free-space-filled two-dimensional waveguide—a slab of free space sandwiched between two reflecting layers. As mentioned above, these reflecting layers can be composed of any material that is not free space in order to produce some reflection back into the free space region from outward propagating waves. The reflecting layers can be stratified, as they are only defined by their net reflection coefficients.

In the free space region, because $\partial/\partial y = 0$, the fields can be separated into independent transverse electric (TE) and transverse magnetic (TM) groups [Cheng, 1989, p. 523]. However, since the ionosphere is a magnetized plasma, these fields are coupled at the upper boundary and an incident TE wave produces both TE and TM reflections, so that purely TE or TM propagation is not possible in the Earth-ionosphere waveguide. The coupling between the modes means that the reflection coefficient from the upper boundary is not a scalar but is rather a 2×2 matrix [Budden, 1962], where each element is one of the four different reflection coefficients for a specific incident and reflected polarization. The lower boundary of the Earth-ionosphere waveguide is the ground, which can be specified by a permittivity and conductivity but is not treated as anisotropic, so that the off-diagonal, cross-polarized reflection coefficients in the ground reflection matrix are zero. Each element in the reflection matrices is a function of the angle of incidence to the boundary.

Figure 2.3 shows the coordinate system and the configuration of the problem to be solved. The line quadrupole source is parallel to the y -axis at a height $z = 0$. The region of free space is between $z = 0$ and $z = z_f$. The reflection matrix of the upper medium referenced to $z = 0$ is given by \mathbf{R}_U , and the reflection matrix of the lower medium referenced to $z = 0$ is given by \mathbf{R}_L . The matrices \mathbf{R}_U and \mathbf{R}_L are given by

$$\mathbf{R}_U(\theta) = \begin{bmatrix} \parallel R_{\parallel}(\theta) & \parallel R_{\perp}(\theta) \\ \perp R_{\parallel}(\theta) & \perp R_{\perp}(\theta) \end{bmatrix} \quad \mathbf{R}_L(\theta) = \begin{bmatrix} \parallel \bar{R}_{\parallel}(\theta) & 0 \\ 0 & \perp \bar{R}_{\perp}(\theta) \end{bmatrix}. \quad (2.5)$$

The left subscript on the matrix elements denotes the incident wave polarization (parallel or perpendicular to the plane of incidence containing the wave vector k and the boundary normal), and the right subscript denotes the reflected polarization.

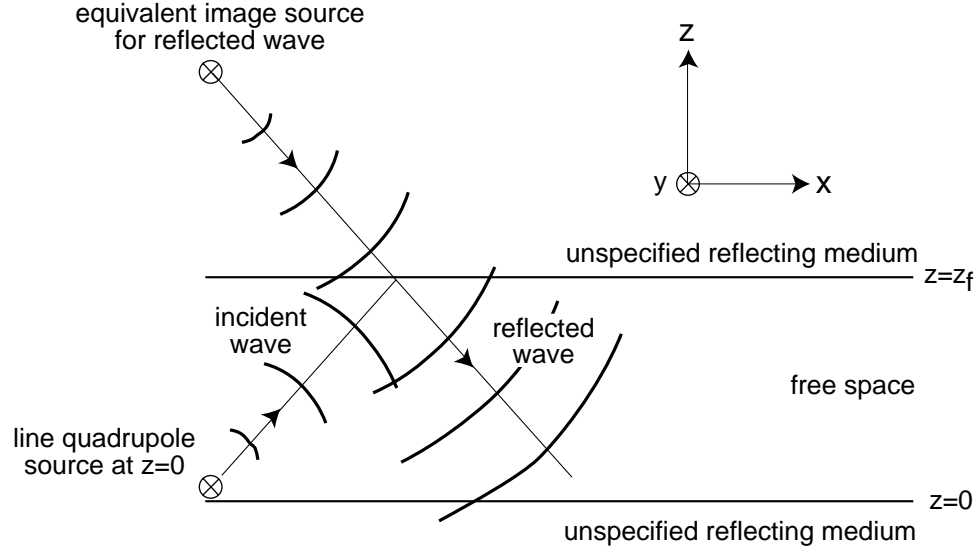


Figure 2.3: Coordinate system for the waveguide and demonstration of equivalent image source.

R denotes a downward reflection coefficient, and \bar{R} denotes an upward reflection coefficient, consistent with commonly-used notation [e.g. *Pappert and Bickel, 1970*].

The successive reflections from the upper and lower boundary create fields in the free space region that are exactly equivalent to those from an infinite series of image sources whose source amplitude and phase are set to ensure that the fields they produce in the free space region are the same as would be produced by the reflections. This equivalence is also illustrated graphically in Figure 2.3.

The use of these image sources allows the free space field to be written as an infinite sum combining (2.4) and \mathbf{R}_U and \mathbf{R}_L [*Budden, 1962*]. This infinite summation can be condensed into a single integral for the Hertz vector in the free space region

$$\begin{aligned}
 U_z = -\frac{kIl}{8\pi^2\omega} \int_C \exp(-ikx \cos \theta) \exp(-ikz \sin \theta) \\
 \cdot \begin{bmatrix} 1 & 0 \end{bmatrix} (\mathbf{I} + \mathbf{R}_U) \mathbf{W} (\mathbf{I} + \mathbf{R}_L) \begin{bmatrix} 1 \\ 0 \end{bmatrix} \cos \theta d\theta
 \end{aligned}
 \tag{2.6}$$

where $\mathbf{W} = (\mathbf{I} - \mathbf{R}_L \mathbf{R}_U)^{-1}$.

This integral can be evaluated by extending the integration into the complex plane, and the value of the integral is given by the sum of the residues from the poles of the integrand, which are all located where $\mathbf{W}^{-1} = 0$ or

$$\det [\mathbf{I} - \mathbf{R}_L(\theta)\mathbf{R}_U(\theta)] = 0. \quad (2.7)$$

Equation (2.7) is the mode condition. Its solution requires that one eigenvalue of the net reflection coefficient $\mathbf{R}_L\mathbf{R}_U$ be unity, a requirement which is equivalent to stating that the plane wave reflected once each from the upper and lower boundaries must be in phase with the incident plane wave [Budden, 1962] (for a good discussion of this mode condition in simpler waveguides, see Kraus [1992, p. 691]). Each angle of incidence θ_n that satisfies (2.7) is referred to as an *eigen angle* and defines an individual waveguide mode at the single frequency ω under consideration.

The contribution to the integral in (2.6) from these poles (each of which defines a mode) can be found analytically. After replacing the line quadrupole source by a point dipole source and solving for \mathbf{B} from the Hertz vector U_z , using the asymptotic expansion $H_\nu^{(2)}(kx \sin \theta_n) \approx \sqrt{\frac{2}{\pi kx \sin \theta_n}} \exp[-i(kx \sin \theta_n - \pi/4 - \nu\pi/2)]$ for $|kx \sin \theta_n| \gg 1$ [Abramowitz and Stegun, 1972, p. 364], and redefining θ to be the angle of incidence relative to the upper waveguide boundary normal ($\cos \theta \rightarrow \sin \theta$), the transverse horizontal magnetic field B_y at $z = 0$ (which is the field measured in this work) in this flat waveguide is given by

$$B_y(x) = \frac{ik^{3/2}\mu_0 I l}{\sqrt{8\pi x}} \exp(i\pi/4) \sum_n \Lambda_n \sqrt{\sin \theta_n} \exp(-ikx \sin \theta_n), \quad (2.8)$$

where Λ_n is given by

$$\Lambda_n = \begin{bmatrix} 1 & 0 \end{bmatrix} \frac{[\mathbf{I} + \mathbf{R}_u(\theta_n)] \mathbf{X} [\mathbf{I} + \mathbf{R}_l(\theta_n)]}{\left. \frac{\partial \Delta}{\partial(\sin \theta)} \right|_{\theta=\theta_n}} \begin{bmatrix} 1 \\ 0 \end{bmatrix}, \quad (2.9)$$

with $\Delta(\theta) = \det(\mathbf{W}^{-1})$ and $\mathbf{X} = \lim_{\theta \rightarrow \theta_n} \mathbf{W} \Delta$. After some matrix manipulations using (2.5) and using the fact that $\Delta = 0$ at $\theta = \theta_n$, Λ_n is expressed in terms of the individual reflection coefficients as

$$\Lambda_n = \frac{(1 + \|\bar{R}_\parallel\|)^2 (1 - \perp \bar{R}_\perp \perp R_\perp)}{\|\bar{R}_\parallel\| \left. \frac{\partial \Delta}{\partial(\sin \theta)} \right|_{\theta=\theta_n}}, \quad (2.10)$$

The physical basis of each term in (2.8) can be identified. The leading constant is a source term which depends on frequency and the source current-moment $I l$ of the vertical dipole source. Λ_n is commonly referred to as the excitation function for a particular mode at a given frequency, and it quantifies the efficiency with which that mode is excited by a vertical dipole on the ground. The $x^{-1/2} \exp(-i k x \sin \theta_n)$ term describes the propagation of a cylindrically expanding wave, which exists because the expansion in the vertical direction is limited by the waveguide boundaries so that the mode fields spread in only the radial dimension. The summation is over an infinite number of modes, but in practice it can be limited only to the modes which contribute significantly to the fields at a distance x from the source.

2.4.2 Correction for Spherical Earth

Equation (2.8) was derived for a flat earth. For distances from the source where the curvature of the Earth becomes significant, this equation must be modified. The $x^{-1/2}$ term which describes the field attenuation due to energy spreading in the waveguide is much like the x^{-1} spreading factor for fields in free space (which corresponds to a x^{-2} factor for the wave power). In a spherical waveguide with radius R_E , the corresponding attenuation factor is $[R_E \sin(x/R_E)]^{-1/2}$ [Budden, 1962], which approaches $x^{-1/2}$ in the limit as $R_E \rightarrow \infty$. To account for this, (2.8) must be multiplied by the correction factor $\sqrt{\frac{x/R_E}{\sin(x/R_E)}}$, which is very close to unity for $x \ll R_E$ but becomes significantly larger than unity for larger distances from the source, where the waveguide curvature plays a more important role.

The mode condition (2.7) must also be modified in the presence of the curved Earth. *Richter* [1966] introduced a coordinate transformation that converts the coordinate system from cylindrical to planar. The physical effect of the transformation is to create a planar waveguide with a modified refractive index n_{mod} that varies with altitude in the free space region as $n_{mod}^2 = \exp(z/R_E)$. If this n_{mod}^2 is expanded in a Taylor series and only the first term is kept, then the modified refractive index becomes $n^2 = 1 + 2z/R_E$, which is exactly the form used in *Budden* [1962] and *Pappert* [1968] except for the inclusion of a reference height $h \neq 0$ where $n_{mod}^2 = 1$. In this way,

the effects of a cylindrically curved earth can be included in the mode calculations without drastic modification of the general method.

2.4.3 Excitation and Height-Gain Functions

The above derivation included the excitation factor for a vertical dipole source on the ground and for an horizontal magnetic field observed on the ground. However, one may be interested in different source orientations and altitudes, or different observed field components. *Pappert and Ferguson* [1986] addressed these questions and summarized the necessary modifications to (2.8) to include these factors.

These modifications come in the excitation factor of (2.10) and in the inclusion of two new factors called *height-gain functions*, which describe the variation of the field components with altitude in the waveguide. The height-gain functions $f_{by}(z)$, $f_{ex}(z)$, and $f_{ey}(z)$ (for B_y , E_x , and E_y , respectively) are explicitly defined in *Pappert and Ferguson* [1986]; however, the height-gain functions referred to in this work are unnormalized, so the normalizing factors included in *Pappert and Ferguson* [1986] must be removed. The modified Hankel functions h_1 and h_2 mentioned in *Pappert and Ferguson* [1986] can be defined in terms of Airy functions [*Budden*, 1985, p. 205]. As in a perfectly conducting, flat waveguide (where the height-gain functions are sines and cosines), these functions are oscillatory in nature with the lower order modes (farther from the cutoff frequency) containing fewer oscillations.

Figure 2.4 plots the normalized magnitude of the height-gain functions for two different modes at 10.0 kHz. They are only plotted up to 75 km altitude because the particular analytic forms from *Pappert and Ferguson* [1986] are only valid in the free space region below the ionosphere. The height-gain functions in the ionosphere can be calculated numerically [*Pappert and Moler*, 1978], but they cannot be used to simulate sources or receivers in the ionosphere, as all of the above analysis is only valid for fields in the free space region between the ground and ionosphere.

When all of these factors are included in (2.8), we obtain the equation for a general output field F

$$F = C(F) \frac{ik^{3/2}Il}{\sqrt{8\pi x}} \exp(i\pi/4) \sum_n \Lambda_{tn} \Lambda_{rn} \exp(-ikx \sin \theta_n), \quad (2.11)$$

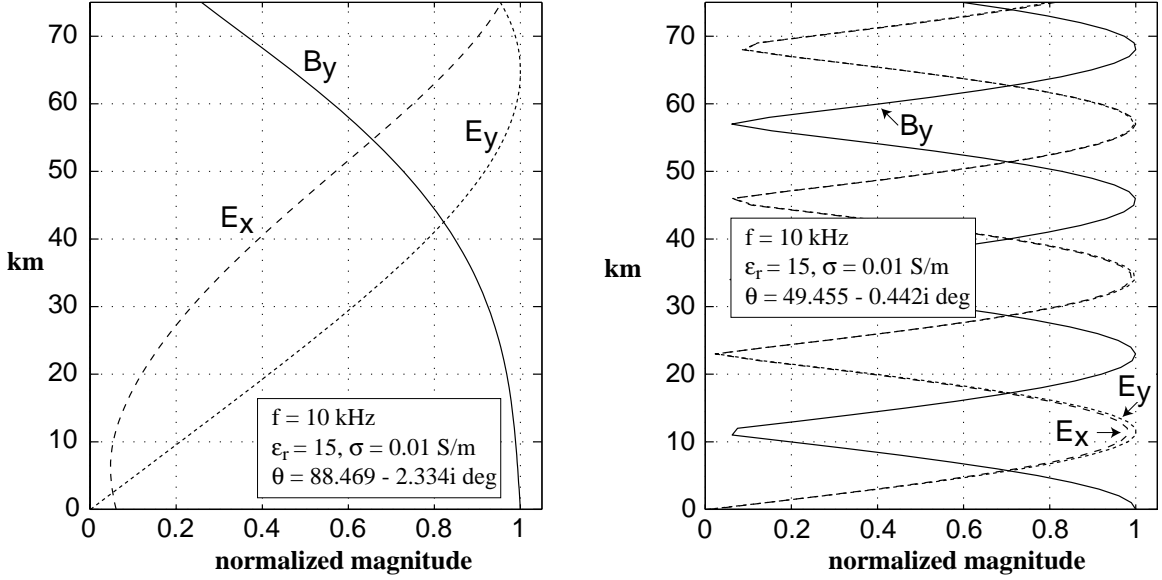


Figure 2.4: Normalized height-gain functions for two different modes at 10 kHz.

where $C(F) = \mu_0$ if F is a component of \mathbf{B} , and $C(F) = \sqrt{\mu_0/\epsilon_0}$ if F is a component of \mathbf{E} . The assumed source in (2.11) is an electric dipole oriented at an angle γ to the z (vertical) axis and at an angle ϕ to the x axis (in the propagation direction) and at an altitude of $z = z_t$. Λ_{tn} and Λ_{rn} are respectively the transmitter and receiver excitation factors which contain the height-gain functions.

A previously developed software package called MODEFNDR [Morfitt and Shellman, 1976] is used to solve the mode condition and calculate the reflection coefficients. Since MODEFNDR calculates the reflection coefficients referenced to an altitude other than $z = 0$ (which has been assumed so far), it is useful to change the definition of the reflection coefficients to match the MODEFNDR output and reference the coefficients to $z = d$, where d is an altitude chosen by the program for easier solution of the mode condition.

With this change, Λ_{tn} is given by

$$\Lambda_{tn} = -A \sin(\theta_n) \cos(\gamma) f_{by}(z_t) + B \sin(\gamma) \cos(\phi) f_{ey}(z_t) + A \sin(\gamma) \sin(\phi) f_{ex}(z_t) \quad (2.12)$$

Output Field	Λ_r
B_y	$f_{by}(z_r)$
E_z	$-f_{by}(z_r) \sin(\theta_n)$
E_y	$f_{ey}(z_r) \frac{(1 + \perp \bar{R}_\perp) \parallel \bar{R}_\parallel \perp R_\parallel f_{by}(d)}{(1 + \parallel \bar{R}_\parallel)(1 - \perp R_\perp \perp R_\perp) f_{ey}(d)}$
E_x	$-f_{ex}(z_r)$

Table 2.1: Receiver excitation functions for 4 output field components.

with

$$A = \frac{\sin^{1/2}(\theta_n)(1 + \parallel \bar{R}_\parallel)^2(1 - \perp \bar{R}_\perp \perp R_\perp)}{\parallel \bar{R}_\parallel \left. \frac{\partial \Delta}{\partial(\sin \theta)} \right|_{\theta=\theta_n} f_{by}^2(d)} \tag{2.13}$$

$$B = \frac{\sin^{1/2}(\theta_n)(1 + \parallel \bar{R}_\parallel)(1 + \perp \bar{R}_\perp) \parallel R_\perp}{\left. \frac{\partial \Delta}{\partial(\sin \theta)} \right|_{\theta=\theta_n} f_{by}(d) f_{ey}(d)} \tag{2.14}$$

remembering that all of the reflection coefficients in these equations are now referenced to $z = d$. In the notation of MODEFNDR and *Pappert and Ferguson* [1986], $A = t_1$ and $B = t_3 t_4$.

The receiver excitation factor Λ_{rn} depends on the receiver altitude z_r and the output component of interest. Table 2.1 contains Λ_{rn} for 4 of the 6 observable output fields, as adapted from *Pappert and Ferguson* [1986]. The excitation factor for the other two observable fields B_x and B_z can be relatively simply derived from the relations $B_x = \frac{1}{i\omega} \frac{\partial E_y}{\partial z}$ and $B_z = -\frac{1}{i\omega} \frac{\partial E_y}{\partial x}$, which are from Maxwell's equations with $\partial/\partial y = 0$.

2.5 Implementation in LWPC

A complete two-dimensional waveguide propagation formulation is implemented in a series of programs called LWPC (Long Wave Propagation Capability) that was developed over many years at the Naval Ocean Systems Center (now NCCOSC/NRaD) [*Ferguson et al.*, 1989]. The overall code is made up of three parts: PRESEG, MODEFNDR, and FASTMC, each of which are described below.

2.5.1 PRESEG

PRESEG determines the necessary waveguide parameters and formats them properly for input to the next stage of the program. Ground conductivity and permittivity are taken from a table based on an experimental study of these parameters over the entire surface of the Earth [Hauser *et al.*, 1969], and the magnitude and direction of the Earth's magnetic field are determined from a built-in magnetic field model. For the case of homogeneous ionosphere, ground, and magnetic field that is the primary focus of this thesis, the original PRESEG program was modified so that the ground and magnetic field parameters for the waveguide were those found at the center of the great-circle propagation path from source to receiver. When inhomogeneities are included, then the waveguide is segmented into a number of slabs, and slab boundaries are placed where the ground parameters change or when the ambient magnetic field has changed by some prescribed quantity from that in the previous slab. The waveguide parameters in each slab are then those at the start of the slab (the end closest to the transmitter).

2.5.2 MODEFNDR

MODEFNDR is the workhorse of the LWPC model and requires the most computational effort of the three parts. It takes the waveguide parameters from PRESEG and searches for angles inside some defined region of the complex plane which satisfy the mode condition (2.7). In order to solve the mode equation, the ionospheric reflection coefficients must be calculated for general electron density, ion density, and collision frequency profiles and for an oblique and complex angle of incidence. Only then can the necessary mode constants be determined and (2.11) be used to compute the fields in the waveguide. In MODEFNDR, this is done by assuming that, for a fixed angle of incidence θ , all field components vary in x as $\exp(-ikx \sin \theta)$ throughout the free space and the ionosphere. Since $\partial/\partial y = 0$, Maxwell's equations are then reduced to a system of ordinary differential equations varying in altitude z [Budden, 1985, p. 182]. This system is numerically integrated using a method developed by Pitteway [1965], and from this solution the reflection coefficients for the given θ are calculated.

MODEFNDR also calculates the excitation factors of each mode, which are needed to calculate the final field strengths. The standard MODEFNDR output is designed for immediate input into FASTMC (see below) and contains factors close to, but not exactly the same as, the excitation factors in (2.12) and Table 2.1. In order to model propagation under a homogeneous ionosphere, the default MODEFNDR output was slightly modified to contain precisely these excitation factors. By including a subroutine for the height-gain functions, the output field can then be calculated directly from (2.11). A series of Matlab routines were written to perform such a calculation for arbitrary source orientation, source and receiver height, and output field component.

2.5.3 FASTMC

For propagation in an inhomogeneous waveguide, the fields must be carefully propagated through the waveguide discontinuities. The program for performing this mode conversion calculation is FASTMC [Pappert and Ferguson, 1986]. As it was not used for the majority of the calculations in this thesis, we will omit a discussion of the details and instead refer the reader to Ferguson and Snyder [1980] and Pappert and Morfitt [1975].

The output of FASTMC is the magnitude (in dB over 1 $\mu\text{V}/\text{m}$ field strength for a radiated power of 1 kW, independent of frequency) and phase (in degrees) of the vertical electric field. Such a source is not equivalent to a vertical dipole, and a correction factor of $4.1887 \times 10^{-6} Il f \exp(i\pi/4)$ must be applied to the FASTMC output amplitudes so that the output field (in $\mu\text{V}/\text{m}$) is that which would have been radiated by a vertical electric dipole of strength Il (in units of A·m) at a frequency f (in Hz).

2.6 Parameters of the Spheric Propagation Model

The frequency-domain model described above is employed to model the propagation of sferics from the source lightning discharge to a remote receiver. The ground and

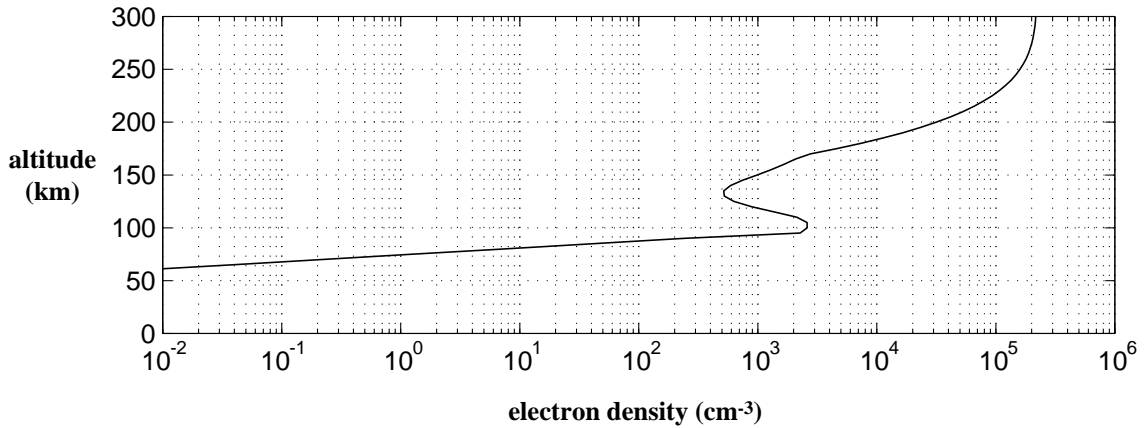


Figure 2.5: A representative midlatitude nighttime electron density profile.

ambient magnetic field parameters are automatically included as described in Section 2.5.1. Other factors to be included are discussed in the following sections.

2.6.1 Ionospheric Electron Density

As shown in Section 2.2, one of the parameters which controls electromagnetic propagation through a cold plasma is the electron density. Figure 2.5 shows a representative nighttime, midlatitude ionospheric electron density profile. Below 95 km (the *D* region), the electron density exponentially increases with altitude. Above 95 km, the profile is more complicated and was calculated using the International Reference Ionosphere (IRI) [Rawer *et al.*, 1978]. This profile is used in the sample calculations presented in Section 2.7.

2.6.2 Ionospheric Collision Frequency

Other important parameters for electromagnetic wave propagation in a cold plasma are the electron- and ion-neutral collision frequencies. *Wait and Spies* [1964] assembled experimental electron-neutral collision frequency profiles from laboratory measurements [Phelps and Pack, 1959], partial reflection data [Belrose and Burke, 1964], and propagation-based rocket measurements [Kane, 1962], and found that all of these

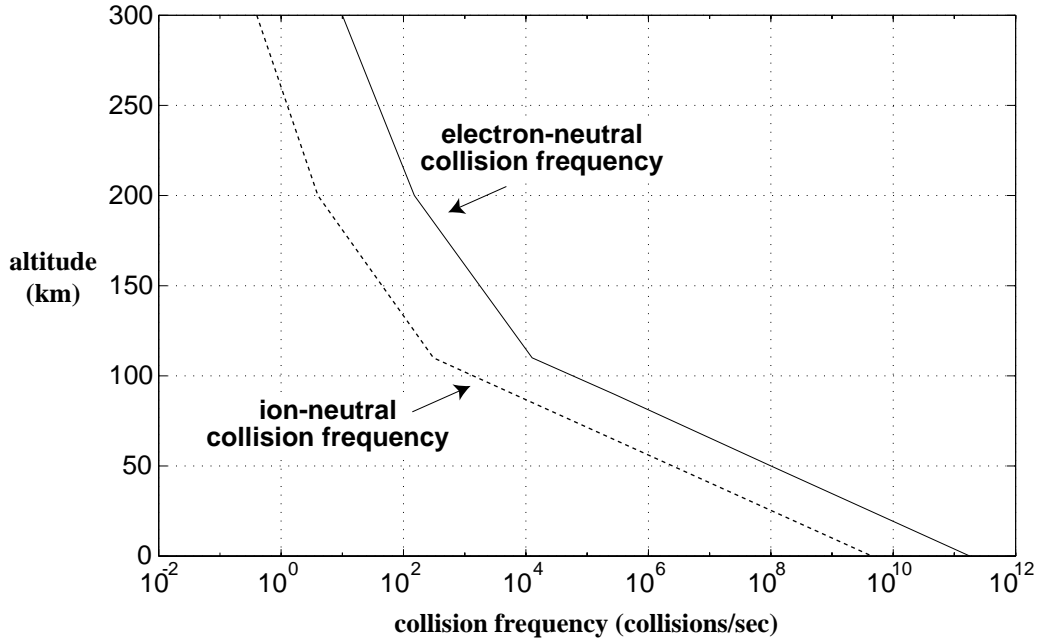


Figure 2.6: Electron-neutral and ion-neutral (both positive and negative) collision frequency profiles.

measurements were very closely approximated by

$$\nu_e = 1.816 \times 10^{11} \exp(-0.15z), \tag{2.15}$$

where z is the altitude measured in km, and ν is in units of sec^{-1} . The ion-neutral collision frequencies are taken to be $\nu_i = 4.54 \times 10^9 \exp(-0.15z)$ for both positive and negative ions [Morfitt and Shellman, 1976]. This strong exponential decay of collision frequency with altitude does not continue above ~ 100 km, and from 100-300 km altitude collision frequencies from Rishbeth and Garriott [1969, p. 131] are used. The composite electron and ion collision frequencies used in this work are plotted in Figure 2.6.

The collision frequencies depend primarily on the neutral atmospheric density, especially below 100 km altitude [Budden, 1985, p. 11]. For this reason, it is assumed in this work that the variability of ionospheric collision frequency is much less than that of ionospheric electron density, and the collision frequency profile is taken to be fixed. Collision frequency variations due to VLF heating of the ionosphere can be

detected from single frequency VLF propagation measurements [*Inan et al.*, 1992], and lightning can induce heating and collision frequency enhancements in the ionosphere [*Rodriguez et al.*, 1992]. However, these are localized effects, and we assume that their effect on sferic propagation is negligible. It will be shown in Section 3.2.5 that large-scale collision frequency profile changes have only a small effect on sferic propagation, especially at night, so for our purposes the assumption of a fixed collision frequency profile is reasonable.

2.6.3 Lightning Return Stroke Waveform

The waveform of the current-moment (current times distance) in the lightning return stroke is the effective sferic source, and as such it plays a significant role in the modeling of the sferic. Unfortunately, for observed sferics, this waveform is rarely a known parameter, so we need to assume a particular functional form.

The lightning discharge process is complicated, with the detailed dynamics occurring on many time scales [*Uman*, 1987, p. 12]. Although a number of these processes can radiate at VLF, the VLF emission is dominated by the lightning return stroke [*Arnold and Pierce*, 1964], which is considered in this work.

Many different lightning return stroke models exist [*Thottappillil et al.*, 1997], most of which were developed in an effort to explain μs -scale details in observations of the electric and magnetic fields close to the source (<100 km). For VLF radiation observed at a significant distance, a much simpler return stroke model suffices. The model used here was originally developed by *Bruce and Golde* [1941] and summarized (along with other similar models) by *Jones* [1970].

The current flowing at the ground during the return stroke is taken to have the form

$$i_g(t) = i_{g0} [\exp(-at) - \exp(-bt)]. \quad (2.16)$$

From a review of experimental data [*Berger*, 1961], *Dennis and Pierce* [1964] concluded that reasonable parameter values are $i_{g0} = 20$ kA, $a = 2 \times 10^4 \text{ sec}^{-1}$, and $b = 2 \times 10^5 \text{ sec}^{-1}$.

The return stroke pulse is assumed to propagate up the lightning channel with an

exponentially decreasing velocity given by $v(t) = v_0 \exp(-\gamma t)$, where $v_0 = 8 \times 10^7$ m/sec and $\gamma = 3 \times 10^4 \text{ sec}^{-1}$, based on photographic data [Schönland, 1956]. The net current-moment of the return stroke channel is then given by [Jones, 1970]

$$i(t) \cdot l(t) = i_{g0} \frac{v_0}{\gamma} [\exp(-at) - \exp(-bt)] [1 - \exp(-\gamma t)]. \quad (2.17)$$

The total charge moved to ground in such a discharge is simply given by

$$q = \int_0^\infty i_g(t) dt = i_{g0} \left(\frac{1}{a} - \frac{1}{b} \right). \quad (2.18)$$

Figure 2.7 plots the current-moment waveform and the spectrum of the current-moment for this model discharge. Unless specifically stated, this source waveform will be assumed throughout this work.

2.7 Sample Calculation

Now that all of the pieces of the sferic propagation model are in place, we present a sample calculation for a physically realistic scenario. The source lightning discharge is at $37^\circ\text{N } 100^\circ\text{W}$, and the receiver is at Stanford University ($37.43^\circ\text{N } 122.16^\circ\text{W}$), for a propagation distance of 1960 km. The electron density and collision frequency profiles from Sections 2.6.1 and 2.6.2 are used, and the effect of ions is neglected. The source current-moment from Section 2.6.3 is used.

2.7.1 Sferic Spectrum

Since the model completes its calculations in the frequency domain, the output is a complex spectrum (amplitude and phase) of the received signal as a function of frequency. Figure 2.8 shows the output spectral amplitude of B_y as would be observed on the ground for a single sferic using the return stroke model of Section 2.6.3. The form of this spectrum appears quite complicated, but its particular shape can be understood relatively easily. Below ~ 1.5 kHz, only the analog of the TEM mode in a perfectly conducting waveguide is present. Because of the anisotropy of the ionosphere, this mode is not strictly TEM but is referred to as the quasi-TEM (QTEM)

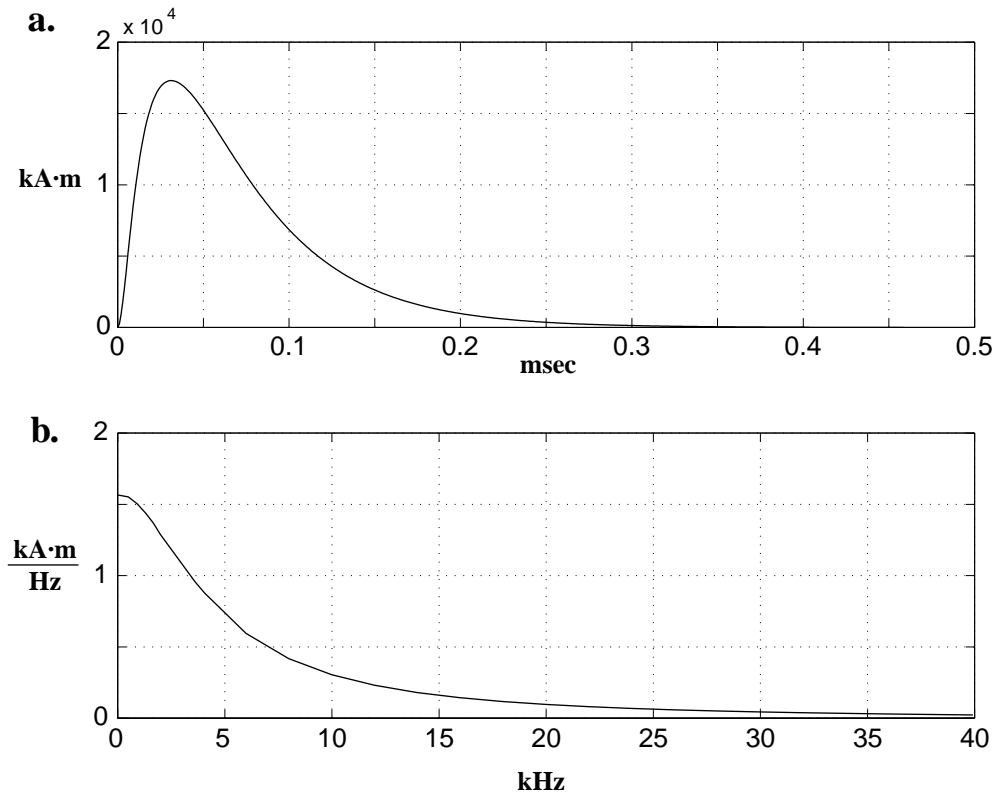


Figure 2.7: The model lightning current-moment waveform (a) and the current-moment amplitude spectrum (b).

mode and does not have a cutoff frequency. However, the nature of the boundaries causes the attenuation of the QTEM mode to increase steadily with increasing frequency, so that this mode does not contribute significantly to the signal at the receiver above ~ 1.2 kHz.

The spectral amplitude exhibits a sharp increase due to the appearance of a waveguide mode with a cutoff frequency at ~ 1.6 kHz. As in a perfectly conducting waveguide, there are actually two modes with this cutoff frequency, but they cannot be divided into strictly TE and TM modes because of the anisotropy of the ionosphere. Instead, they are classified as either quasi-TE (QTE) or quasi-TM (QTM), depending on whether the TE or TM field components are dominant in the free space region. Unlike in the perfectly conducting waveguide where the TE modes do not contribute

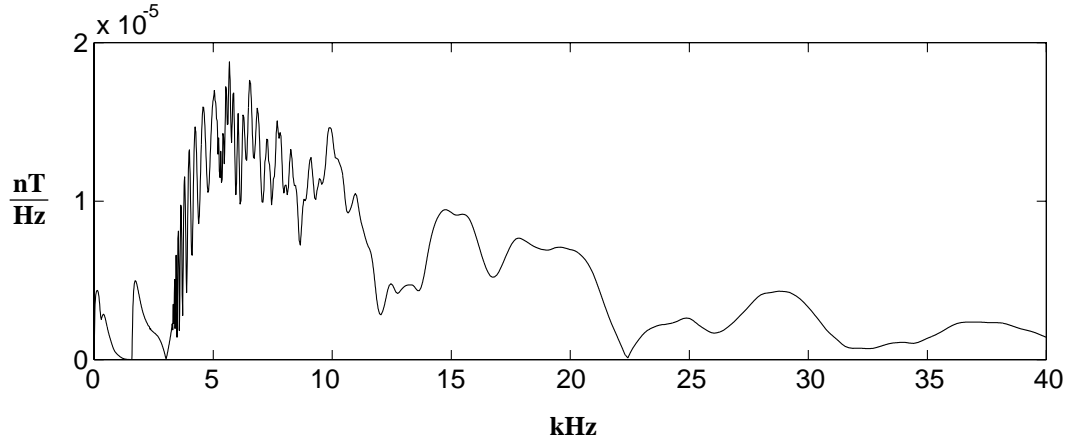


Figure 2.8: Modeled sferic amplitude spectrum from 0–40 kHz.

to the observed B_y on the lower waveguide boundary, in the real Earth-ionosphere waveguide the QTE modes do contain a non-zero B_y component at the boundary. In fact, the QTE mode fields are much larger than the QTM fields near their cutoff frequencies because of the extreme attenuation of the QTM modes. Thus this single mode above ~ 1.6 kHz is classified as a QTE mode.

Above ~ 2.5 kHz, the QTM mode attenuation is low enough for it to contribute to the observed field. Because the QTE and QTM modes do not have identical phase velocities, their relative phase at a fixed observation point changes with frequency. As the frequency increases, the interference between these two modes shifts from being constructive to destructive. This interference is the source of the nearly zero amplitude at ~ 3 kHz—the two modes are almost identical in amplitude but 180° out of phase, so that their sum is nearly zero.

At ~ 3.3 kHz, the character of the spectrum changes drastically. This is due to the presence of the next higher order QTE mode with a cutoff frequency of ~ 3.3 kHz. This mode has a significantly different phase velocity from the lower order QTE and QTM modes, so that the relative phase between modes changes much more rapidly with frequency, producing the striking rapid modal interference variations. At higher frequencies, the phase velocity of this second-order mode is closer to that of the other modes, and the signal amplitude varies more slowly with frequency.

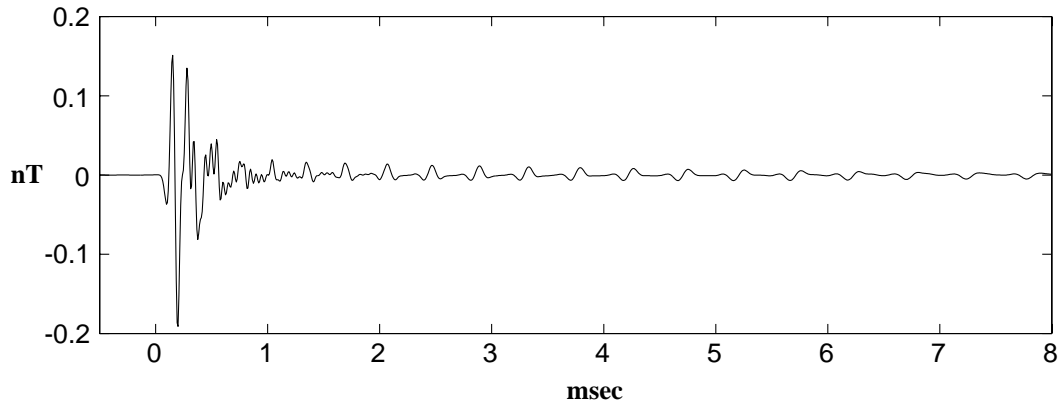


Figure 2.9: Modeled sferic waveform.

The appearance of new modes at even higher frequencies increases the complexity of the modal interference variations. However, the attenuation of modes near cutoff increases with increasing frequency, so that above 10 kHz, the near-cutoff modes have a relatively small effect. In this frequency range, there are many (5 or more) modes with similar phase velocities, so that the signal amplitude changes more slowly with frequency. However, the overall effect of the interference of so many modes is complicated, resulting in an irregular interference pattern.

It should be emphasized that since the modal interference variations are functions of the relative phase of the individual modes, the position and amplitude of these variations depends strongly on the propagation distance. The spectral amplitude from the same sferic should appear significantly different at different ranges from the source.

2.7.2 Sferic Waveform

Since the output of the sferic propagation model is the Fourier transform of the sferic waveform, an inverse Fourier transform (IFT) operation provides the time variation of B_y . The numerical method used in this work for this inversion is described in Appendix A.

Any waveform must be observed on a band-limited system, that is, frequencies

above and below a certain value are filtered out by the system and not observed. Such a filter must be applied to the output spheric spectrum before a waveform can be calculated. The filters present in the receiving system used for the data acquisition are discussed in detail in Section 3.1.2, but they can be briefly described as a single pole, 420 Hz high pass filter, and a many pole, extremely sharp ~ 20 kHz low pass filter. After applying the frequency response (amplitude and phase) of these filters to the output spectrum in Figure 2.8, the numerical IFT operation yields the B_y spheric waveform plotted in Figure 2.9. The characteristics of the waveform are similar to those expected from the qualitative analysis in Section 2.1. Most of the energy arrives at the front of the signal, but there is a distinct tail of individual pulses whose separation time increases slowly and approaches a limiting value.

Chapter 3

D Region Measurements using VLF Sferics

As shown in the previous chapter, the factors that control the guided propagation of VLF waves are the source characteristics (orientation, position, and time-varying current), the electrical properties of the ground (conductivity and permittivity), and the state of the ionosphere. Suppose that for a particular sferic the source orientation, the source position, and the electrical parameters of the ground for the particular propagation path are known. The two remaining unknown parameters that control the characteristics of the received sferic are then the source current and the ionosphere. If the effects of these two parameters are separable, it should then be possible to extract information about the ionosphere along the propagation path from the received sferics by iteratively varying the ionosphere used in the VLF propagation model described in the previous chapter until a good match between theory and observation is obtained.

The source location for an individual sferic can be accurately found from National Lightning Detection Network (NLDN) [*Bernstein et al., 1996*] data. This system is implemented with over 100 receivers across the United States which use magnetic field direction finding and time-of-arrival analysis to pinpoint cloud-to-ground (CG) discharge locations to a mean accuracy of 500 meters [*Bernstein et al., 1996*]. Timing is accurate to better than 1 ms, using GPS-based timing, and the system captures over 90% of the CG discharges within its coverage area [*Bernstein et al., 1996*]. With the

sferic source location known, the only unknown propagation factor is the ionosphere, which we intend to measure.

In the propagation model, it is assumed that the ionosphere is homogeneous along the propagation path. Thus, the proposed sferic-based measurement yields a single inferred ionosphere which is in some sense a path-integrated ionosphere, since the ionosphere along the entire path affects sferic propagation. In Section 3.2.4, it is shown that this single inferred ionosphere is in fact the average ionosphere along the entire propagation path, i.e. the path-averaged ionosphere. The ionospheric measurement realized with the technique developed here is different from previous techniques mentioned in Section 1.2, all of which measure the ionosphere at a specific point. A path-averaged measurement cannot detect fine structure as well as a point measurement; however, such a measurement can efficiently measure large-scale structure.

The sample calculation in Section 2.7 included the effects of the ionosphere from *D* region altitudes to *F* region altitudes. While it is known that the propagation of the QTEM mode ($f < 1.5$ kHz) is affected by the ionosphere over this entire altitude range [Pappert and Moler, 1974; Barr, 1977], the QTM and QTE modes ($f > 1.5$ kHz) are essentially confined below the *D* region, at altitudes where $N_e < 10^3$ cm⁻³. This fact will be demonstrated later (in Section 3.2.2), but it merits mention now because it provides a convenient separation of the QTEM mode and the QTE/QTM modes. The subject of this chapter is the measurement of the *D* region electron density profile, thus only the QTE/QTM modes are included in the sferic propagation model. Modeling the propagation of the QTEM mode is discussed in Chapter 4.

3.1 VLF Sferic Observations

3.1.1 Sample VLF Sferics

Before we present the analysis of sferic waveforms, it is useful to show some examples of typical and atypical sferic waveforms. Figure 3.1a shows a typical sferic waveform received at Stanford from a relatively large (-56 kA peak current) CG lightning discharge that occurred in the midwestern United States. The sferic waveform has

the expected time-domain form based on the theoretical analysis in Section 2.7, with large peaks in the early portion of the waveform followed by a long tail composed of distinct pulses which represent the arrival of the signal along individual ray paths. Figure 3.1b shows a spectrogram of this waveform, which agrees qualitatively with the heuristic spectrogram in Figure 2.2. The sferic tail is composed of discrete frequency components, each of which represents an individual mode in the Earth-ionosphere waveguide. The QTE_1 mode dominates the tail, but a close examination reveals a total of four modes above the noise. This spectrogram was produced using a method described in *Kim and Ling* [1993] and is comprised of narrow Δt /wide Δf cells in the early portion of the signal and wide Δt /narrow Δf cells in the later portion. Such a variable $\Delta t/\Delta f$ cell aspect ratio is ideal for displaying the frequency-time structure of a waveform like this, where the early part of the signal is impulsive but the later part contains discrete frequencies.

Figures 3.2a–d show samples of unusual sferic waveforms. While not representative of those used in the ionospheric measurement technique presented here, these sferics are interesting examples of what can be found when analyzing broadband VLF data. The sferic in Figure 3.2a has a tail that is composed of unusually discrete pulses (rather than the almost single frequency in Figure 3.1a), which implies that many near-cutoff modes contribute to the late-time signal. Waveforms such as this indicate a sharp ionospheric boundary so that losses are very low for the higher-order modes.

Figure 3.2b shows a sferic with an unusually long tail of more than 45 ms. Sferics such as this one are often referred to as “tweeks” [*Yamashita*, 1978] because of the distinct chirping sound they make when played on a loudspeaker. Such sferics also indicate relatively low propagation losses for modes near cutoff, but, as is typical of the very long tweeks that the author has seen, the tail is composed of essentially a single frequency rather than a discrete set of frequencies. This result implies that either the source discharge does not significantly radiate at the frequencies of the higher-order modes, or that losses are much lower for the first-order mode than for the higher-order modes. This tweek, and others the author has seen, was not associated with an NLDN-recorded discharge, suggesting that it may have propagated from the east over the Pacific Ocean. An all-ocean path is consistent with the low losses observed, as salt

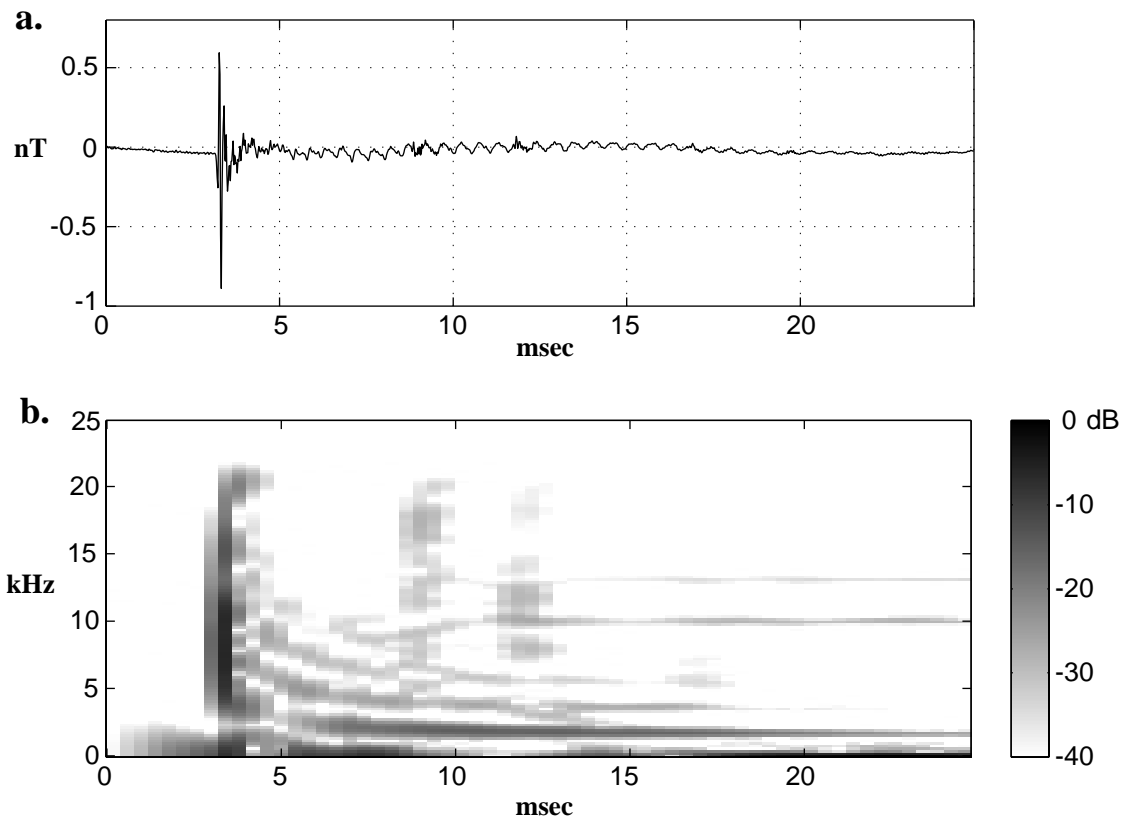


Figure 3.1: Spectrogram (a) and waveform (b) of a representative large sferic.

water is a significantly better conductor (~ 4 S/m) than typical earth ($\sim 10^{-2}$ S/m).

Figure 3.2c shows another tweek waveform, but for this one the peak sferic amplitude is hardly larger than the peak amplitude in the tail, indicating either a discharge radiating a large amount of energy near 2 kHz but relatively little above, or extremely low propagation losses near the cutoff frequency of the first-order mode. Figure 3.2d shows perhaps the most unusual sferic of these four, one containing a tail with no apparent initial peak. It is possible that the tweeks in Figures 3.2b–d are all a manifestation of nearly lossless propagation near the cutoff frequency of the first-order mode. The tweek in Figure 3.2d could have propagated over such a long distance that the initial portion has attenuated below the noise level but with the tail still remaining, or it could have been produced by a discharge that radiated strongly near

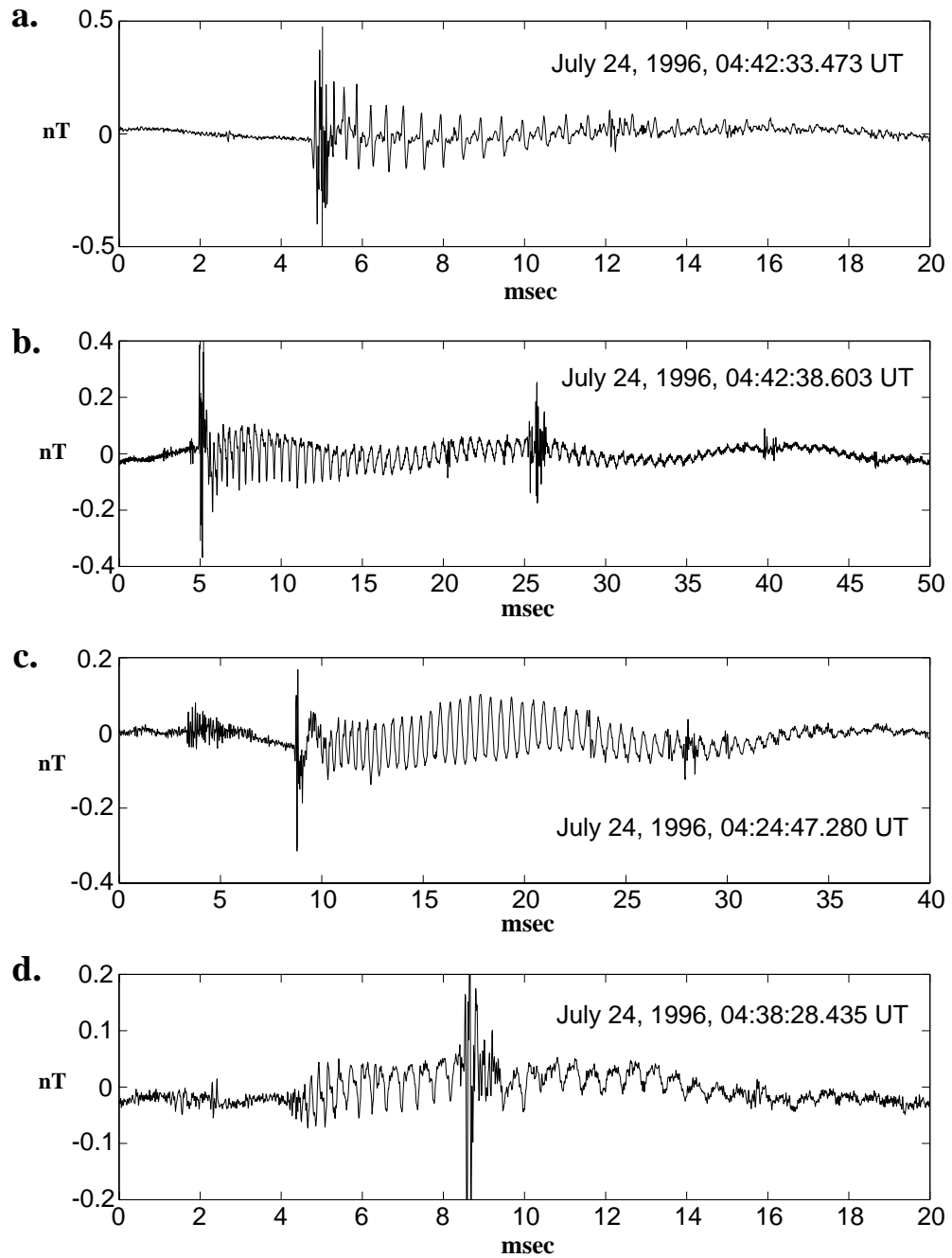


Figure 3.2: Unusual sferics received at Stanford on July 24, 1996.

2 kHz but weakly (or not at all) above ~ 3 kHz.

3.1.2 Data Acquisition

The measurements presented in this chapter were made with the Stanford University VLF Radiometer [*Fraser-Smith and Helliwell, 1985*]. The receiving antennas of this system are two orthogonal triangular loops, but only the one oriented 78° east of magnetic north was used in this study (the magnetic declination at Stanford is $\sim 17^\circ$, so that this alignment corresponds to $\sim 95^\circ$ east of geographic north). After low-pass filtering of the antenna signal at ~ 90 kHz, the output signal is 16-bit sampled at 44.1 kHz and digitally recorded (PCM) on a Betamax video tape. The recorded signal can then be extracted and sampled via playback on a Betamax player through a PCM-decoder. The frequency response of the recorded signal is dominated on the low end by a single-pole high-pass filter with a measured cutoff of 420 Hz, while on the upper end the response is dominated by a very sharp anti-aliasing low-pass filter in the PCM encoder with a ~ 20 kHz cutoff frequency. The overall impulse response of this VLF system was measured by injecting a 1 microsecond pulse into the calibration input of the receiver, recording the output signal on a Betamax tape, and then extracting the signal from the tape.

The measured time-domain impulse response and frequency-domain spectral amplitude of the overall system response are plotted in Figure 3.3. Of particular note is the fact that from ~ 8 – 20 kHz, the response is not flat but falls by a factor of 2. The effect of this filter is included in all of the theoretical waveforms and spectra in this chapter by convolving this measured impulse response with the theoretical waveforms, so that the forthcoming comparisons of measurements and theory are as accurate as possible.

The absolute calibration of the magnetic field measurements into calibrated units (nT) is straightforward. At 5 minutes after every hour, the system automatically injects a calibration signal comprised of single frequency components spaced every 250 Hz at an amplitude level equivalent to 0.1 pT for one second. The difficulty in this scheme is that the 0.1 pT level is rather low compared to the ambient noise level

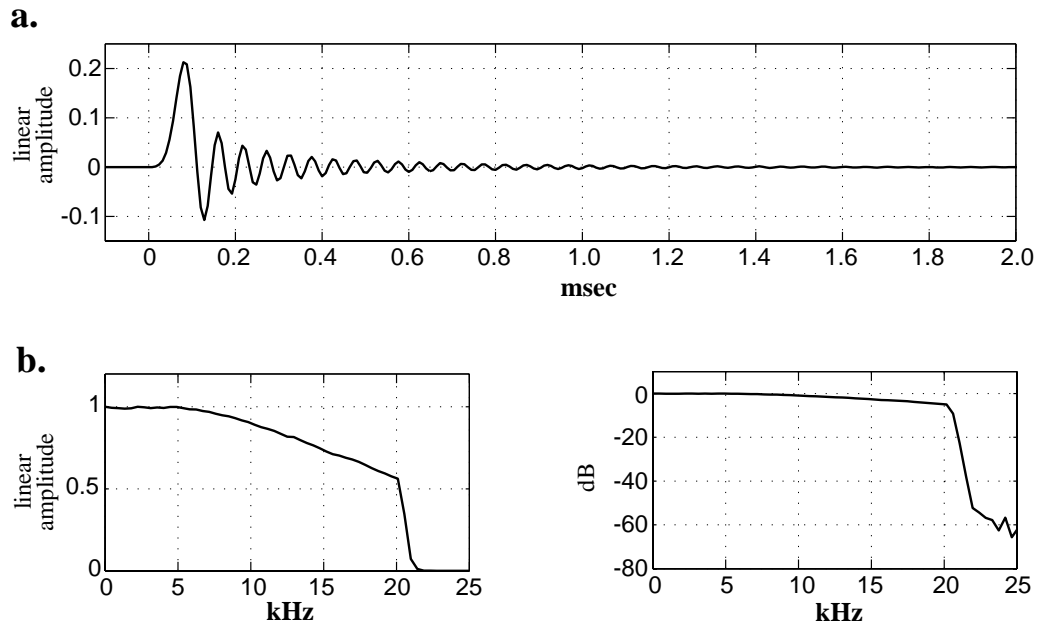


Figure 3.3: Measured impulse response (a) and frequency response (b) of anti-aliasing filter in the data acquisition system.

created by the steady stream of sferics arriving from all corners of the Earth. Even by trying to extract the calibration factor from as quiet a period as possible, there is an uncertainty of $\sim 5\%$ in the absolute calibration for the data presented in this chapter. However, this uncertainty does not affect the ionospheric measurements made in this chapter, which do not depend on the absolute system calibration.

3.2 Theoretical Effects of Ionospheric Parameters on VLF Propagation

Before we can extract information from the observed sferics using the sferic propagation model of Chapter 2, we must investigate the dependence of sferic characteristics on the various ionospheric parameters (electron density, collision frequency, positive and negative ions, etc.) that are included in the model.

Throughout this chapter, we assume that the *D* region electron density can be

described by a two-parameter exponential profile,

$$N_e(h) = 1.43 \times 10^{13} \exp(-0.15h') \exp[(\beta - 0.15)(h - h')], \quad (3.1)$$

with N_e in electrons/cm³, h' in km and β in km⁻¹. This specific functional form has been used with success in previous comparisons between VLF propagation theory and measurement [e.g. *Bickel et al.*, 1970; *Thomson*, 1993], and agrees well with directly observed *D* region profiles [e.g. *Sechrist*, 1974].

The two parameters h' and β control respectively the altitude and the sharpness of the profile. However, for a constant β , a change in the height parameter h' of $\Delta h'$ shifts the ionosphere by more than $\Delta h'$ because of the $\exp(-0.15h')$ term. This functional form for the electron density originates in *Wait and Spies* [1964], who used it as a basis for exponential profiles of a conductivity parameter $\omega_r = \omega_p^2/\nu$. When (3.1) is combined with the collision frequency profile in (2.15), ω_r has a simpler exponential dependence on h' and β . *Wait and Walters* [1963] found from numerical calculations that the ionospheric altitude where $\omega_r = 2.5 \times 10^5$ rad/sec is a good representation of the reflection height for VLF waves, and h' in (3.1) is the altitude where this occurs, assuming that (2.15) is used for the collision frequency profile. *Bickel et al.* [1970] found that $h' = 85.5$ km and $\beta = 0.5$ km⁻¹ provided good agreement with midlatitude, nighttime observations of the variation of field strength with distance from the source at single frequencies, as measured on an airplane. In a theoretical investigation using the same LWPC VLF propagation model employed here, *Thomson* [1993] found that a profile of $h' = 70$ km and $\beta = 0.45$ km⁻¹ was consistent with midlatitude, daytime propagation measurements.

3.2.1 Electron Density Profile

The effect of the electron density profile parameters h' and β on the characteristics of sferics must be understood before any electron density assessment can be made. These effects are investigated on a propagation path 1960 km long (from 37°N 100°W to Stanford, at 37.43°N 122.16°W). For this section and others below, daytime and

nighttime ionospheres will be considered separately because reflection occurs at altitudes (~ 85 km at night and ~ 70 km during the day) with different collision frequencies, leading to significant differences in the dependence on electron density of the characteristics of the received signal.

Nighttime h and β

Figure 3.4a shows two nighttime electron density profiles with different heights ($\beta = 0.5$ km $^{-1}$, $h' = 85$ and 82 km), and Figure 3.4b and 3.4c show the theoretical sferic spectra and waveforms calculated for each of these cases. The differences between the two cases are quite clear: the spectrum corresponding to the higher reflection height is compressed (but it maintains the same shape), and the individual pulses in the late-time waveform are farther apart. This effect is expected based on the qualitative analysis of waveguide propagation presented in Section 2.1. For a higher waveguide boundary, the cutoff frequencies are proportionally lower, causing the compression of the spectrum. Alternately, in the time domain, the higher waveguide boundary means a longer total distance for each ray to travel from the source to the receiver, which increases the time between the arrival of the late-time pulses.

The effect of β on sferic characteristics is more subtle. Figure 3.5a shows two nighttime electron density profiles with different sharpnesses ($h' = 85$ km, $\beta = 0.5$ and 0.4 km $^{-1}$), and Figure 3.5b and 3.5c show the sferic spectra and waveforms for each. The spectrum for the $\beta = 0.4$ profile is significantly smoother than that for $\beta = 0.5$, especially above 10 kHz, and the amplitude of the modal interference variations at lower frequencies is slightly smaller for the smaller β . A close examination of the two waveforms shows that the $\beta = 0.5$ ionosphere yields late-time pulses that are slightly sharper than those for the $\beta = 0.4$ ionosphere. Qualitatively, these effects are expected, since the sharper ionosphere is a better reflector, which in the time domain decreases the losses (and increase the amplitude) of the nearly-vertical, late-arriving rays which are reflected most. In the frequency domain, this improved reflection from a sharper ionosphere correspondingly decreases the attenuation of the most vertically-propagating modes, namely those near cutoff. This decreased attenuation accounts for the increased amplitude of these modes, in turn enhancing the modal interference

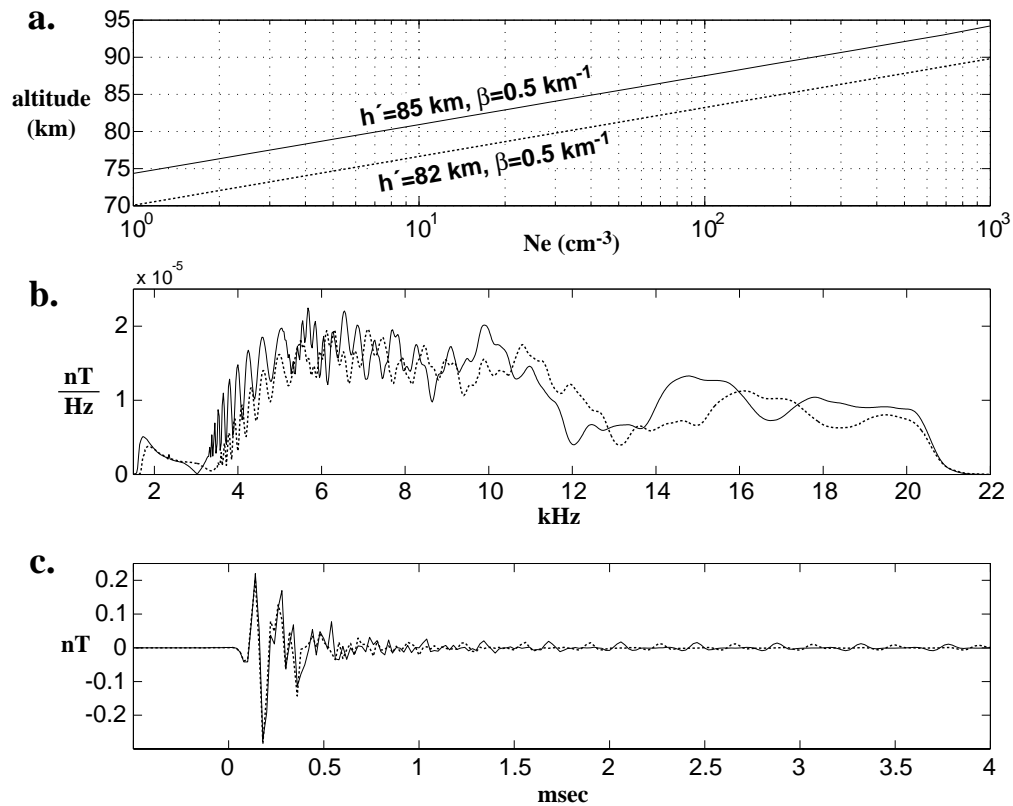


Figure 3.4: A comparison of sferic spectra for two nighttime ionospheres with different values for h' . a: Two nighttime D region density profiles. b: Sferic spectra for the profiles in (a). c: Sferic waveforms for the profiles in (a).

variations.

The above analysis shows that the effects of β and in particular h' are significant in both the sferic waveforms and sferic spectra for a nighttime ionosphere, and thus should be distinguishable in observed sferics. The waveforms and spectra provide the essentially same information about the ionosphere; however, since the observable features are more easily quantified in the spectra than in the waveforms, the theoretical and observed sferic spectra will be the focus of the analysis through the rest of this chapter.

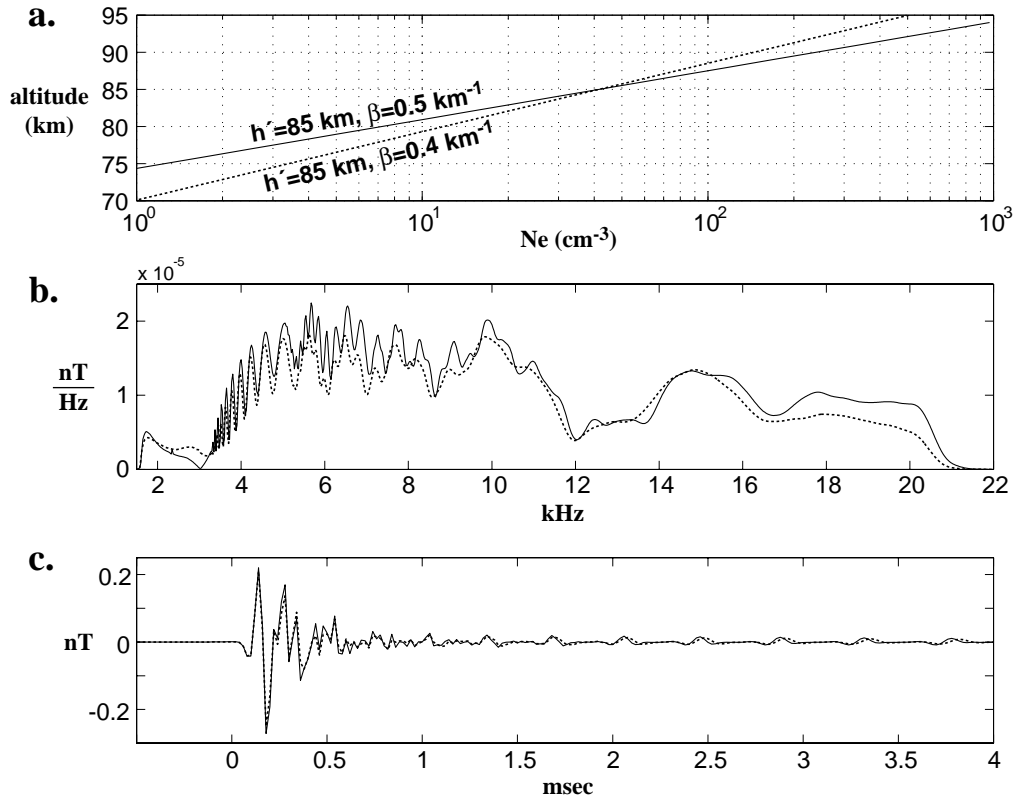


Figure 3.5: A comparison of sferic spectra for two nighttime ionospheres with different values for β . a: Two nighttime D region density profiles. b: Sferic spectra for the profiles in (a).

Daytime h and β

The D region during the day is much denser than at night because of the presence of solar ionizing radiation (primarily X-rays and Lyman- α radiation [Hargreaves, 1992, p. 230]). This enhanced density means that VLF waves are reflected at a lower altitude where the electron-neutral collision frequency is much higher, and thus the effects of ionospheric variability on daytime sferic spectra are different than at night.

Figure 3.6 shows three theoretical sferic spectra for three different representative daytime ionospheres ($h' = 70$ km, $\beta = 0.45$ km $^{-1}$; $h' = 70$ km, $\beta = 0.30$ km $^{-1}$; and $h' = 73$ km, $\beta = 0.45$ km $^{-1}$). The lack of fine spectral features for sferics which propagated under a daytime ionosphere makes a determination of the effects of h' and

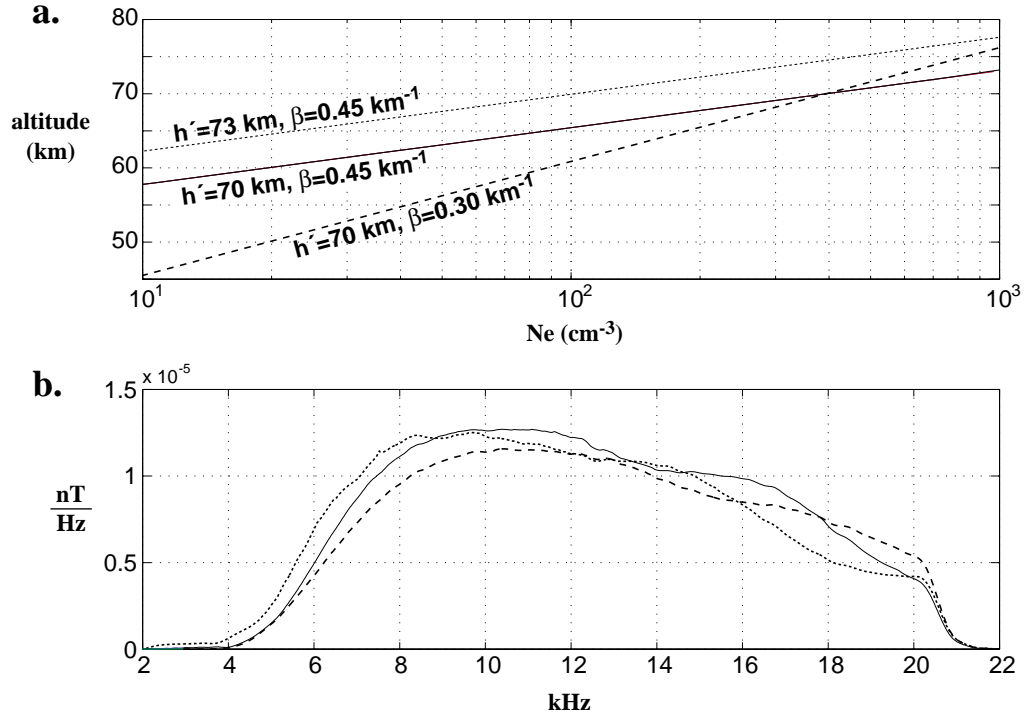


Figure 3.6: A comparison of sferic spectra for three different daytime ionospheres. a: Three daytime *D* region density profiles. b: Sferic spectra for the profiles in (a). c: Sferic waveforms for the profiles in (a).

β difficult. For nighttime ionospheres, there were many fine features that were clearly due to propagation and which changed significantly in response to h' and β . For the same value of β , the height change from $h' = 70$ to 73 km appears to compress the spectrum as it did for the nighttime ionosphere, but this is much less obvious than at night because of the lack of fine features in the spectra to serve as a reference point.

The effects of the change in β from 0.45 to 0.30 km^{-1} are even less noticeable. The amplitude across nearly the entire $2\text{-}22$ kHz band for a fixed h' is lower for $\beta = 0.30$, consistent with extra losses incurred as the wave propagates through the denser region of N_e below the reflection height in the $\beta = 0.30$ case.

In the context of an experimental observation, the broad spectral changes caused by variation of these parameters for daytime ionospheres could easily be due to changes in the source lightning radiation spectrum. This possibility limits the amount of

information about the daytime ionosphere that can be extracted from sferics without knowledge of the source spectrum.

3.2.2 Minimum and Maximum Electron Density

The reflection and guiding of VLF waves in the Earth-ionosphere waveguide is affected only by ionospheric parameters in a limited altitude range. Regions containing electron densities below a certain value do not significantly affect the propagation of the VLF waves and can be accurately treated as free space. Similarly, because there is some frequency-dependent maximum electron density above which a VLF wave cannot penetrate without being almost completely reflected, densities above this value cannot play a significant role in the propagation. These upper and lower limits represent the range of electron densities to which subionospheric VLF propagation is sensitive and thus define the range of electron densities that can be usefully extracted by any VLF-based technique.

The MODEFNDR program includes a provision for the direct specification of these upper and lower electron density limits. Electron densities below the specified lower limit N_e^{min} are ignored and the medium is treated as free space. If this value were set too high, then significant and measurable effects of the lower part of the profile would be ignored.

Above the altitude where N_e is equal to the specified upper limit N_e^{max} , the medium is treated as a homogeneous half-space with $N_e = N_e^{max}$. Any energy still propagating upward at this altitude boundary is effectively lost, as there are no reflections from the homogeneous medium. If N_e^{max} is set too low, then some wave energy that would have been reflected by higher electron densities is not accounted for, resulting in a significant and measurable effect on the propagation.

The higher densities at lower altitudes of a daytime *D* region mean that reflection occurs at an altitude with higher collision frequency than for a nighttime ionosphere. Because of this, the range of N_e that plays a significant role in the reflection of VLF waves is different during day and night, and these ranges are investigated separately in the next two sections.

Nighttime Minimum and Maximum N

As before, $h' = 85$ km and $\beta = 0.5$ km⁻¹ are chosen as a representative nighttime ionosphere, and N_e^{min} and N_e^{max} are separately varied to determine the range of values which have a significant effect on the theoretical sferic spectrum. The changes in the characteristics of the individual modes (phase velocity and attenuation) with N_e^{min} and N_e^{max} can also be examined, but the output spectrum gives a clearer overall measure of the effect.

Figure 3.7a shows four theoretical sferic spectra which propagated from 37°N 100°W to Stanford under an ionosphere with $h' = 85$ km and $\beta = 0.5$ km⁻¹. We have used $N_e^{max} = 10^4$ cm⁻³ for these calculations, which is safely above the level where all significant reflection for VLF frequencies takes place. N_e^{min} is varied from 10^{-1} – 10^2 cm⁻³. The propagation is clearly sensitive to $N_e < 10^2$ cm⁻³, as the spectrum for $N_e^{min} = 10^2$ cm⁻³ is significantly different from the others. Values for $N_e < 10^0$ cm⁻³ have no significant effect, while values of $N_e < 10^1$ cm⁻³ have some effect. Thus we take the minimum significant (and therefore the minimum measurable) N_e to be 10^0 cm⁻³ for nighttime propagation.

Figure 3.7b shows four theoretical sferic spectra for the same propagation path and ionosphere, but with a fixed $N_e^{min} = 10^{-2}$ cm⁻³ and a varying $N_e^{max} = 5 \times 10^2$ – 10^4 cm⁻³. Ignoring $N_e > 10^3$ cm⁻³ has essentially no effect on the propagation, but lowering N_e^{max} to 5×10^2 cm⁻³ does have an effect, especially between 3 and 7 kHz, where the modal interference peaks are shifted. Thus the maximum significant N_e for nighttime propagation is taken to be 10^3 cm⁻³.

Similar calculations with $h' = 80$ km show the same dependence on N_e , indicating that N_e^{max} and N_e^{min} do not vary significantly over the expected range of nighttime ionospheres.

Daytime Minimum and Maximum N

Parameter values of $h' = 70$ km and $\beta = 0.45$ km⁻¹ are taken as a representative daytime ionosphere [Thomson, 1993]. We follow the same procedure as for the nighttime case above to determine the range of N_e that is significant for daytime subionospheric

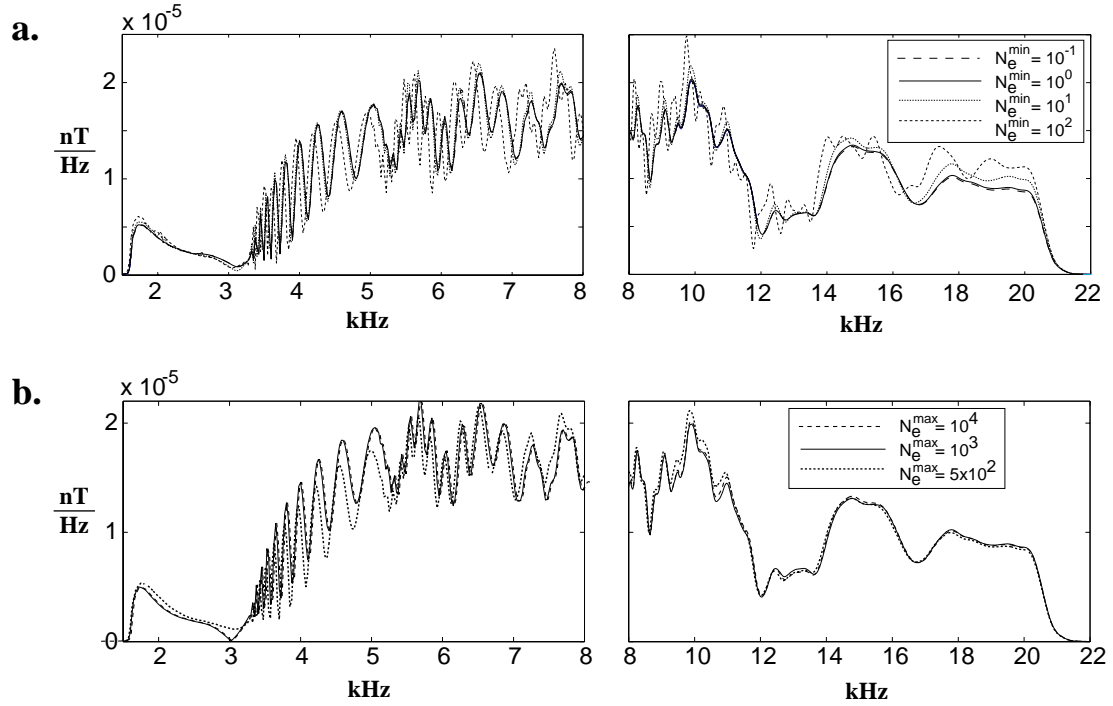


Figure 3.7: Theoretical sferic spectra demonstrating the effect of nighttime N_e^{min} (a) and nighttime N_e^{max} (b) on VLF sferic propagation.

VLF propagation.

Figure 3.8a shows three theoretical sferic spectra with $N_e^{max} = 10^4 \text{ cm}^{-3}$ and $N_e^{min} = 10^0\text{--}10^2 \text{ cm}^{-3}$. Electron densities below $\sim 10^1 \text{ cm}^{-3}$ do not significantly affect the spectrum, while densities below $\sim 10^2 \text{ cm}^{-3}$ do play a minor role. Figure 3.8b shows three theoretical sferic spectra with $N_e^{min} = 10^{-2} \text{ cm}^{-3}$ and $N_e^{max} = 10^2\text{--}10^4 \text{ cm}^{-3}$. As in the nighttime case, $N_e > 10^3 \text{ cm}^{-3}$ does not play a major role in the propagation, but electron densities below this value are important. The range of N_e that has a significant effect on VLF propagation for a daytime ionosphere is thus approximately $N_e = 10^1\text{--}10^3 \text{ cm}^{-3}$, which is narrower than the comparable range for the representative nighttime ionosphere.

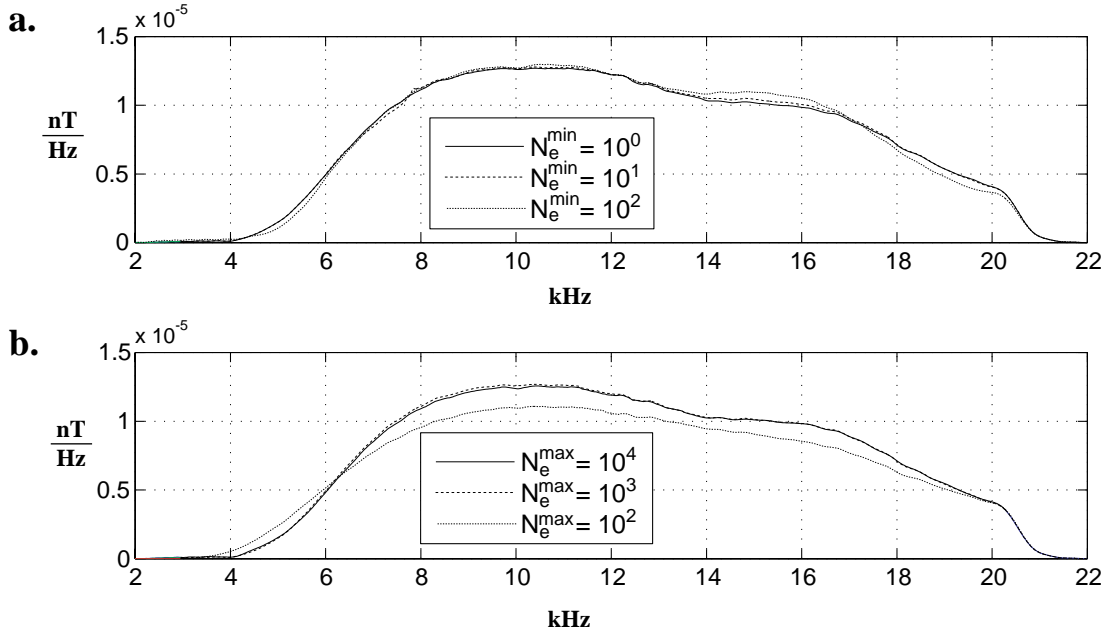


Figure 3.8: Theoretical sferic spectra demonstrating the effect of daytime N_e^{\min} (a) and daytime N_e^{\max} (b) on VLF sferic propagation.

3.2.3 Positive and Negative Ions

As mentioned in Section 2.2, the effect of free ions in the ionospheric cold plasma can be neglected under many circumstances. However, at the lower end of the VLF spectrum, the wave frequency is close enough to the ion plasma- and gyro-frequencies to have a potentially significant effect on wave propagation. In this section we investigate the effect of ions on sferic propagation.

There are few published works on the effect of ions on subionospheric VLF propagation, and it is quite likely that this dearth is due to the fact that relatively little is known about ion species and concentrations in the D region. Midlatitude rocket observations at noon have found that O_2^+ and NO^+ ions dominate above ~ 82 km, and the water cluster ion $\text{H}_2\text{O}\cdot\text{H}_3\text{O}^+$ is the primary ion below ~ 82 km, with a total positive ion density of $\sim 10^3$ – 10^4 cm^{-3} between 65 and 85 km [Narcisi and Bailey, 1965]. Narcisi [1969] reported rocket-based midlatitude nighttime ion measurements in the presence of a sporadic E layer [Hargreaves, 1992, p. 251] at ~ 90 km, which

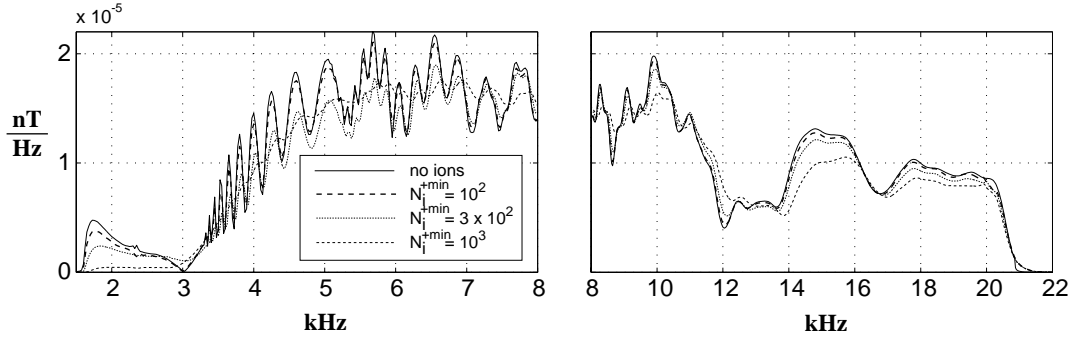


Figure 3.9: Theoretical sferic spectra demonstrating the effect of ions on nighttime VLF sferic propagation.

showed a total positive ion density $< 3 \times 10^2 \text{ cm}^{-3}$ below 80 km.

Although many different ion species are present at D region altitudes, the LWPC propagation model lumps their effect into a single species with atomic mass 32 (equivalent to O_2^+), which is a reasonable approximation to the known dominant species discussed above. As a rough approximation to the daytime observations of *Narcisi* [1971], we assume that below the altitude where N_e equals some predetermined value N_i^{+min} , the positive ion density is constant, so that $N_i^+ = N_i^{+min}$. Above this altitude, $N_i^+ = N_e$. To maintain charge neutrality, N_i^- is determined by $N_i^- = N_i^+ - N_e$.

Figure 3.9 shows four theoretical sferic spectra for nighttime propagation under an $h' = 85 \text{ km}$ and $\beta = 0.5 \text{ km}^{-1}$ ionosphere, three of which include ions with different values for N_i^{+min} . At $N_i^{+min} = 10^2 \text{ cm}^{-3}$, the effect of the ions is small but noticeable, especially below 10 kHz. At $N_i^{+min} = 10^3 \text{ cm}^{-3}$, the effect is drastic—the amplitude of the modal interference variations has dropped significantly.

The above calculations show that increasing the ion densities has essentially the same effect as decreasing β . As a result, when ions are accounted for, the amplitude of the modal interference variations does not yield information about β alone but rather some combination of β and N_i^{+min} . We are then forced to make an assumption about one of these parameters in order to measure the other. Throughout the remainder of this thesis, we assume that $N_i^{+min} = 3 \times 10^2 \text{ cm}^{-3}$, a level at which the effect of ions is significant but not overwhelming. This ion density is lower by as much as a factor

of 10 than that used in theoretical ELF propagation studies [e.g. *Pappert and Moler, 1974*], but is more consistent with the nighttime ion observations of *Narcisi [1969]*. This value for N_i^{+min} is also more consistent with the observed sferics in this work, as a higher positive ion density leads to theoretical spectra with consistently smaller modal interference variations than are observed.

Including ions in our calculations does not significantly affect the *position* of the modal interference oscillations, which was shown previously to be the primary determinant of the electron density profile altitude parameter h' . Thus the uncertainty in N_i^{+min} does not significantly effect the measurement of h' .

Similar calculations for daytime ionospheres show that the effect of an N_i^{+min} from $10^1 - 10^4 \text{ cm}^{-3}$ on a daytime profile ($h' = 70 \text{ km}$, $\beta = 0.45 \text{ km}^{-1}$) is negligible. This is not surprising when considered in the context of losses near the reflection height. For the nighttime case, reflection occurs at an altitude where losses are lower, and the addition of ions introduces a significant amount of loss. But for a daytime ionosphere, the reflection occurs at a substantially lower altitude where the collision frequency is much higher, and electron losses dominate regardless of ion density.

3.2.4 Ionospheric Inhomogeneities

For all of the measurements presented in this chapter, the ionosphere is assumed to be homogeneous along the propagation path, and a single ionosphere is extracted from measurements to describe the entire propagation path. In reality, the ionosphere is almost certainly inhomogeneous to some degree. To have confidence in the inferred ionospheric profile, it is important to verify that even in the presence of ionospheric inhomogeneities, sferic characteristics are determined by the path-averaged mean ionosphere. To do this, we theoretically compare the sferic spectra for propagation under homogeneous and sharply inhomogeneous ionospheres. To simulate the inhomogeneous propagation, we use the FASTMC program described in Section 2.5.3.

The variation of h' with distance along the propagation path for different three ionospheres is shown in Figure 3.10a. One is homogeneous with $h' = 82.5 \text{ km}$ and

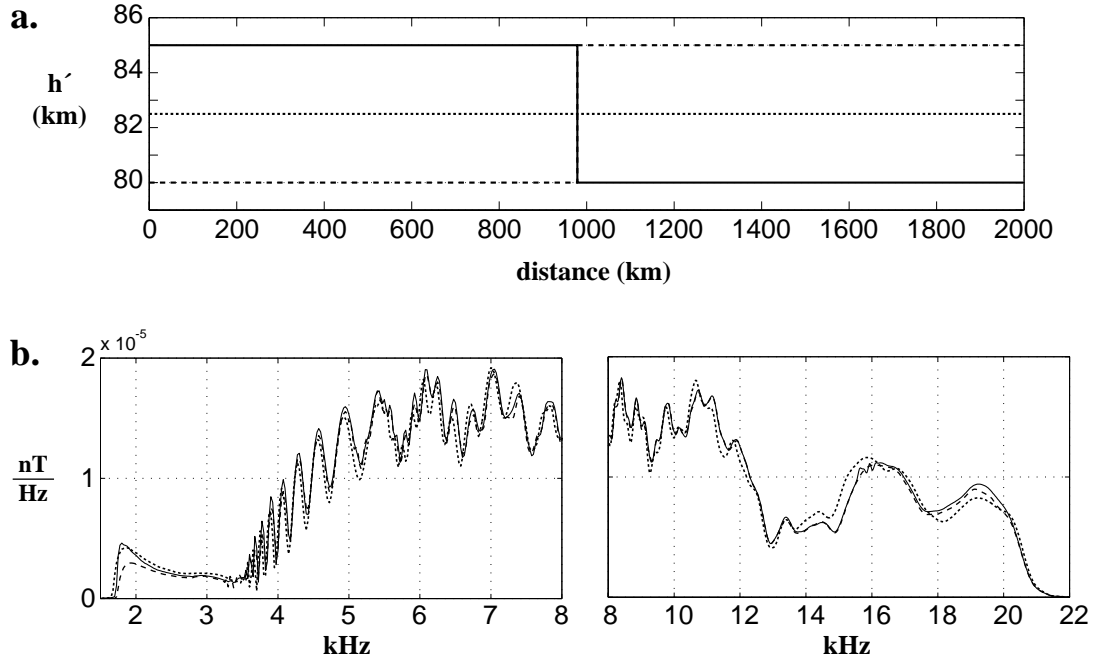


Figure 3.10: A comparison of homogeneous and inhomogeneous spheric propagation. a: The variation of h' with propagation distance for the three cases. b: Theoretical VLF spheric spectra for the homogeneous and inhomogeneous ionospheres.

$\beta = 0.5 \text{ km}^{-1}$ ionosphere. The two inhomogeneous ionospheres have a step-like change in h' at the center of the path. One has $h' = 85.0 \text{ km}$ and $\beta = 0.5 \text{ km}^{-1}$ for the path portion closer to the lightning and $h' = 80.0 \text{ km}$ and $\beta = 0.5 \text{ km}^{-1}$ for the portion closer to the receiver. The other has the same ionospheres only spatially reversed, with $h' = 80.0 \text{ km}$ near the lightning and $h' = 85.0 \text{ km}$ near the receiver. Figure 3.10b shows the theoretical spheric spectra for propagation from $37^\circ\text{N } 100^\circ\text{W}$ to Stanford for three different nighttime ionospheric conditions.

Since the path-averaged ionosphere is the same for the three cases, the spheric spectra must be similar for our method to be able to infer robustly the path-averaged ionosphere in the presence of an inhomogeneity of this magnitude. Figure 3.10b shows that the spectra are quite similar, especially in the critically important positions of the modal interference peaks below 14 kHz. The change in position of these peaks created by the ionospheric inhomogeneities are much smaller than those produced by

a change in h' of 3 km (Figure 3.4), indicating that even significant inhomogeneities will not affect our ability to measure h' from observed sferic spectra. However, the change in the amplitude of the spectral variations below 10 kHz between sferics propagating under the homogeneous and inhomogeneous ionospheres is comparable to that created by a change in β of 0.1 km^{-1} (Figure 3.5). This creates a potentially significant uncertainty in an extraction of β from observed sferics, since it is not known whether an ionospheric inhomogeneity is present over a given propagation path.

A simulation of a more complicated inhomogeneity shows similar results, which are presented in Figure 3.11. The inhomogeneous ionosphere in Figure 3.11a is divided into four equal segments; from the source lightning to the receiver, the third segment has $h' = 80.0 \text{ km}$ and $\beta = 0.5 \text{ km}^{-1}$ while the other three segments have $h' = 85.0 \text{ km}$ and $\beta = 0.5 \text{ km}^{-1}$. The path-averaged ionosphere would then be $h' = 83.75 \text{ km}$ and $\beta = 0.5 \text{ km}^{-1}$, and this homogeneous ionosphere is also shown. The sferic spectra for propagation under these two ionospheres are shown in Figure 3.11b. As in the cases in Figure 3.10, the positions of the interference peaks in the homogeneous and inhomogeneous spectra agree quite closely, but the difference in the amplitude of these peaks implies uncertainty in any extraction of β from measurements.

We thus conclude that the frequencies of the modal interference peaks and valleys are primarily determined by the path-averaged ionosphere, even for ionospheres with substantial inhomogeneities as considered here. This result implies that the values of h' inferred on the basis of these interference peaks constitutes an accurate and robust measure of the average ionosphere even in the presence of ionospheric inhomogeneities. However, the peak-to-peak magnitudes of these interference variations are somewhat smaller for the inhomogeneous case; thus, the possible presence of large and substantial inhomogeneities introduces uncertainty in the measurement of β .

3.2.5 Collision Frequency Profile

In Section 2.6.2, it was stated that we assume the electron collision frequency profile to be fixed, so that any observed effects on VLF sferic propagation is interpreted in terms of changes in the electron density profile. Such an assumption merits some

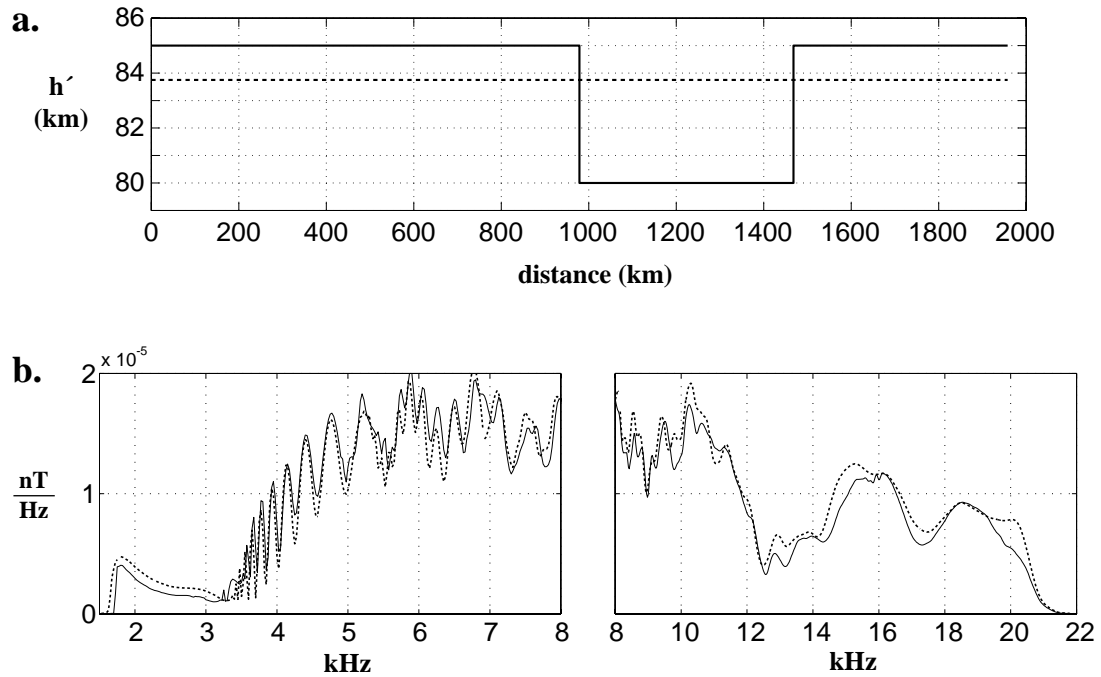


Figure 3.11: Another comparison of homogeneous and inhomogeneous sferic propagation. a: The variation of h' with propagation distance for the two cases. b: Theoretical VLF sferic spectra for the homogeneous and inhomogeneous ionospheres.

investigation.

Figure 3.12 shows two theoretical sferic spectra for propagation under the same nighttime ionosphere ($h' = 85$ km, $\beta = 0.5$ km $^{-1}$, no ions), one using the collision frequency profile in (2.15) and the other using collision frequencies two times larger. The strongest effect is a reduced overall signal amplitude for the higher collision frequency due to the additional loss incurred in propagating through the more collisional plasma. However, the positions of the modal interference variations are not changed significantly below ~ 14 kHz by this collision frequency change, when compared to the changes produced by an electron density change in h' of 3 km (Figure 3.4). That the spectral changes are so small for such a 100% increase in the ionospheric collision frequency indicates that nighttime sferic propagation is relatively insensitive to the collision frequency changes of this magnitude. Collision frequency variations

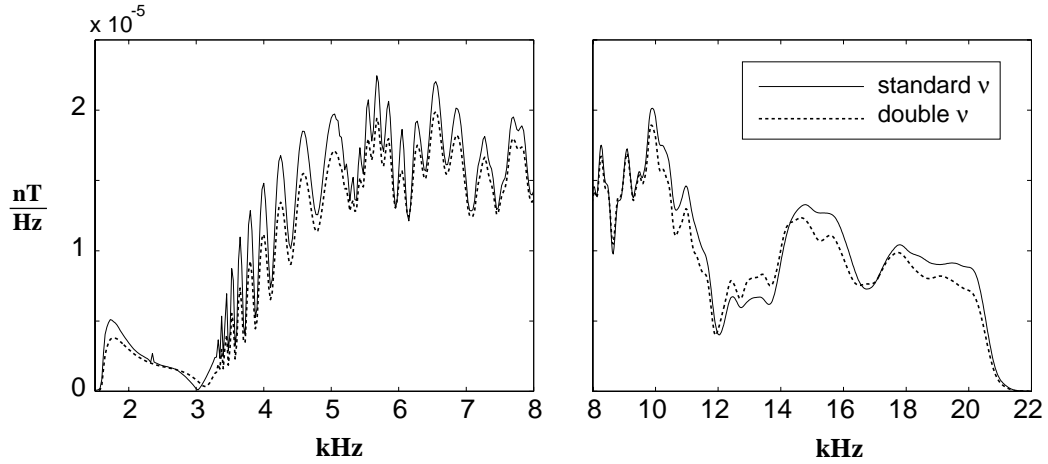


Figure 3.12: Two sferic spectra demonstrating the effect of a factor of two collision frequency increase on nighttime VLF sferic propagation.

due to VLF heating of the ionosphere can be detected from single frequency VLF propagation measurements [*Inan et al.*, 1992], and lightning can induce heating and collision frequency enhancements in the ionosphere [*Rodriguez et al.*, 1992]. However, these are localized effects, and we assume that their effect on sferic propagation is negligible.

The amplitude of the modal interference variations decreases slightly due to this collision frequency enhancement, in a manner similar to that caused by a decrease in the sharpness β of the electron density profile. Thus the uncertainty in the collision frequency profile present over a sferic propagation path introduces further uncertainty in the assessment of β , in addition to the uncertainty associated with ion density and ionospheric inhomogeneities. However, the variation in the measured and theoretical collision frequency profiles on which the assumed profile (2.15) is based is much less than a factor of two [*Wait and Spies*, 1964], so we expect that the actual uncertainty in β due to the unknown collision frequency profile is smaller than that shown in this example.

The effect of the collision frequency profile on daytime sferic propagation is significantly different than for nighttime. As shown in Figure 3.13, a factor of two increase in the collision frequency profile actually decreases losses below ~ 17 kHz. And unlike

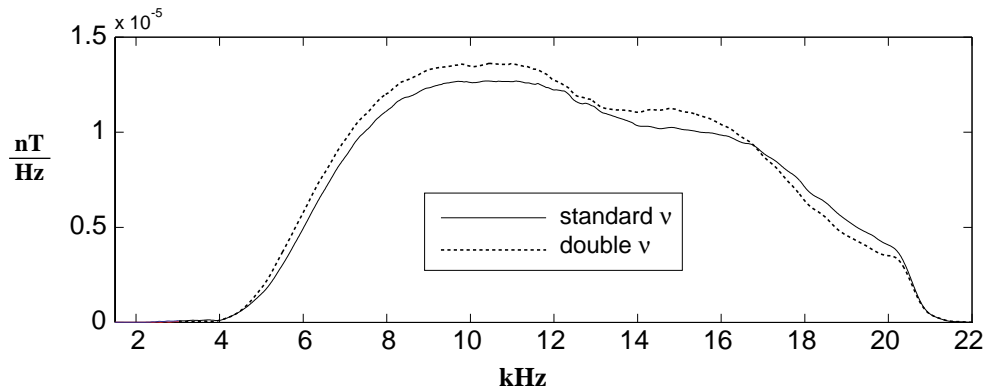


Figure 3.13: Two sferic spectra demonstrating the effect of a factor of two collision frequency increase on daytime VLF sferic propagation.

the nighttime case, this collision frequency increase also shifts the spectral features. This difference in the effect on night and day VLF propagation is again due to the fact that collisions are much less important at the nighttime VLF reflection altitudes than at daytime reflection altitudes.

3.2.6 Ground Altitude

An implicit assumption in the LWPC propagation model is that the ground altitude along a propagation path is constant. In reality, this is not a valid assumption for the typical land paths considered here, especially in the vicinity of the Rocky Mountains. The electromagnetic boundary conditions at the lower waveguide interface are enforced at the ground altitude, so the propagation is sensitive not to the ionospheric height but rather to the difference of the ionospheric height and the ground height. This means that the inferred path-averaged ionosphere is defined relative to the *average ground altitude* of the sferic propagation path. When comparing inferred ionospheres along propagation paths with different mean ground altitudes, this factor must be taken into account (as is discussed in Section 3.4.1).

3.3 Description and Example of *D* Region Measurement Technique

If the location and current-moment waveform for the source lightning discharge for a given sferic are known, then the *D* region electron density along the propagation path can be inferred by iteratively varying the ionosphere in the VLF propagation model until some level of agreement is reached between the modeled and observed sferic spectra. A quantitative measure of this agreement is developed in Section 3.3.3. However, two factors make such a comparison of theory and individual sferics difficult. First, the source lightning current waveform might have spectral features that could be confused with the fine features produced by the propagation, thereby affecting the interpretation. This is unlikely, since it is known that most return stroke waveforms are relatively smoothly varying [Uman, 1987, p. 122] and thus have smooth spectral amplitudes, but since the source current waveform for a sferic is generally not known, this potential ambiguity cannot be avoided. Second, the noise in the measurement created by other sferics limits the amount of information that can be extracted from a single sferic.

Both of these problems can be minimized by averaging many sferic waveforms that are known to have originated from a small geographic location. This averaging has a two-pronged effect: it increases the signal to noise ratio, and it smooths the effective source current-moment waveform. The net result is a single sferic waveform with a higher signal-to-noise ratio that was launched by the equivalent of a smoother source current-moment waveform (the temporal average of all of the individual source waveforms, since the problem is linear).

For each measurement, the sferics to be averaged are limited to those determined by the NLDN to have originated in a 0.5° latitude by 0.5° longitude region (approximately 56 km by 48 km at latitudes of the continental U.S.). Obviously, during any given time period, at most only a few storms in the United States produce enough lightning and sferics for the averaging of sferics originating in such a small region to be useful. More sferics could be included in the average by using a larger location, but the finest expected spectral features of the sferic vary enough with propagation

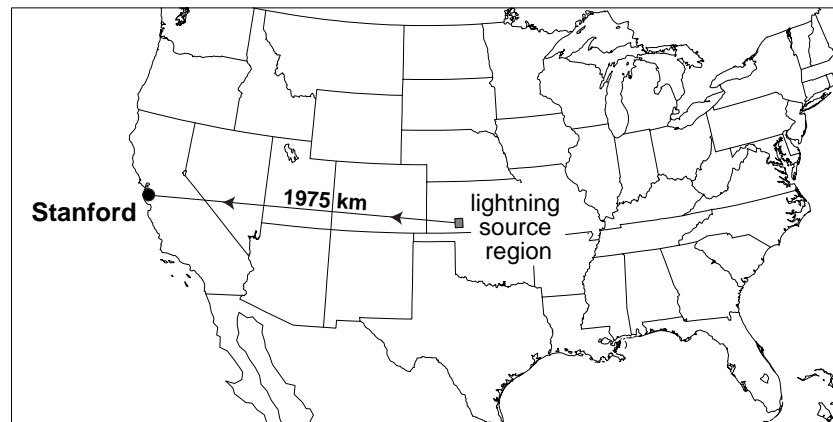


Figure 3.14: Map showing the sferic receiver location (Stanford) and the lightning source region on July 22, 1996, 0415-0445 UT.

distance that they would be partially smoothed out by using a larger area. This difficulty could be taken into account in the modeling by averaging modeled spectra from slightly different locations to produce an equivalent effect. For the purposes of this thesis, the 0.5° by 0.5° area provides enough sferics for averaging and is small enough that the sferic averaging does not significantly smooth out any of the features which are of interest.

The overall procedure for measuring a path-averaged *D* region electron density from an average sferic spectrum is best illustrated by an example. The sferics used in the following sections are from a storm on July 22, 1996, between 0415 and 0445 UT. As shown in Figure 3.14, the source strokes from latitudes 37.3° – 37.8° N and longitudes 99.4° – 99.9° W launched sferics that were received at Stanford, 1975 km away from the center of this source region.

Figure 3.15 shows representative large and small amplitude sferic waveforms and spectral amplitudes from this group. The spectral spikes at 10 kHz are from an intentionally injected tone used for timing and are not part of the signal, and will be present at some level on all of the observed spectra presented in this work. There is also power line hum (at 60 Hz and its harmonics) which does not contribute significantly to the noise in the VLF band. The spectral details that we expect to see, particularly the modal interference variations between 3 and 10 kHz, are present in

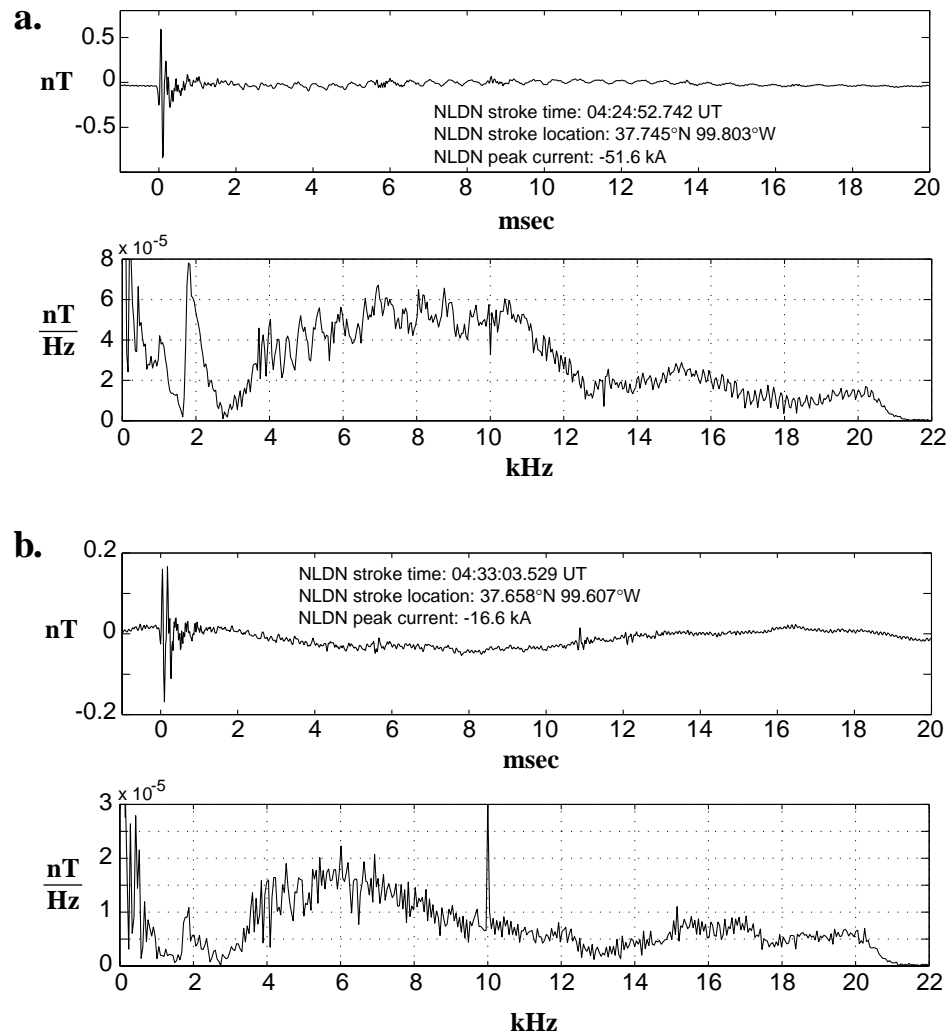


Figure 3.15: Typical large (a) and small (b) sferic waveforms and spectra from lightning discharges on July 22, 1996, from 37.3°–37.8°N and 99.4°–99.9°W.

these individual sferics, even with the broadband noise created by other sferics.

All of the spectral amplitudes presented in this chapter are computed as the magnitude of the Fast Fourier Transform (FFT) [Oppenheim and Schaffer, 1989, p. 514] of the time domain waveform. The observed spectral amplitude is defined as the FFT of the average of the observed waveforms. To compute the theoretical spectral amplitude, the model output spectrum is converted to a time domain waveform via

the inverse Fourier transform method described in Appendix A, and then converted back to a spectral amplitude via the FFT. This ensures that both the theoretical and observed spectra contain the small but perhaps significant artifacts of the FFT, such as leakage due to a finite window width [Oppenheim and Schaffer, 1989, p. 699].

3.3.1 Noise Reduction with Late-Time Filtering

An examination of the frequency-time structure of a typical sferic suggests a possible method to reduce the noise in the measured waveforms at the upper frequencies of the signal. Referring back to the spectrogram in Figure 3.1b, notice that ~ 4 ms after the start of the sferic, the only frequency components present are below ~ 10 kHz. This is primarily because for modes near cutoff (of which the later part of the signal is composed), attenuation varies exponentially with frequency, and any long delayed (i.e. near cutoff) components above 10 kHz are strongly attenuated by the time they propagate to the receiver. This suggests that low-pass filtering a portion of the sferic waveform, from ~ 4 ms after the start of the sferic to the end, for example with a -6 dB cutoff frequency of 10 kHz, with a zero-phase-shift filter [Oppenheim and Schaffer, 1989, p. 285] can eliminate noise without affecting the signal of interest.

The left panels of Figure 3.16 show the latter portion of the sferic waveform from Figure 3.15a, before and after the application of this late-time filtering. The right panels show the spectral amplitudes of the unfiltered and filtered waveforms, which demonstrate that the effect of this late-time filtering is to reduce the noise level above the cutoff of the late-time filter (10 kHz) without affecting the important details of the signal. This filtering technique is applied to all of the VLF sferic waveforms in this chapter prior to their inclusion in the averaging.

3.3.2 Sferic Averaging Procedure

After assembling the group of sferics for time averaging, the waveforms must be accurately time-aligned so that the averaging is coherent and does not significantly smooth out the higher frequencies of the sferic. Most sferics from a single location

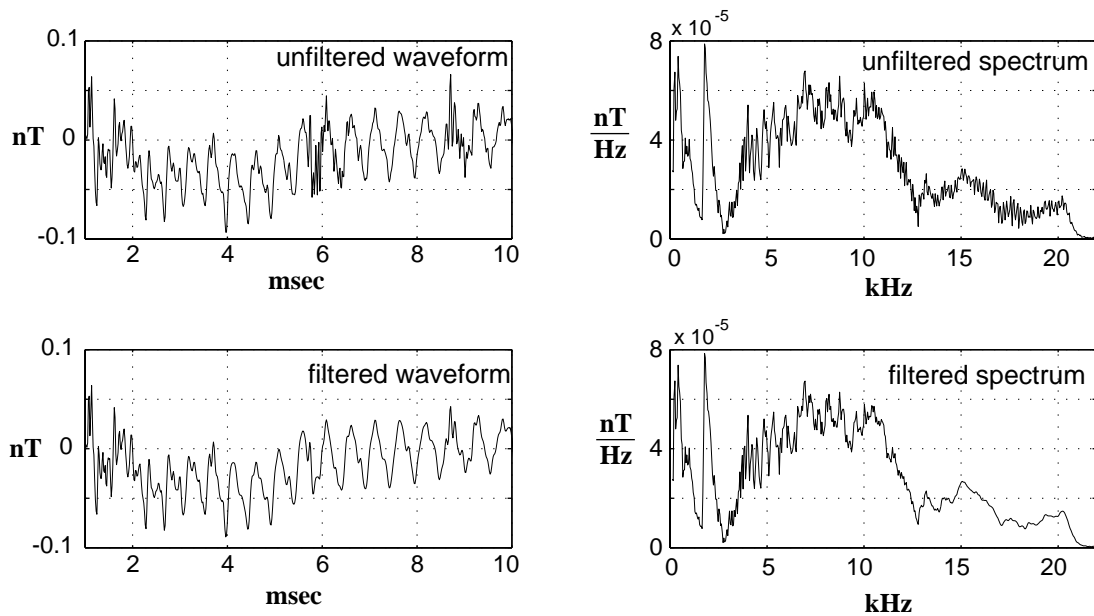


Figure 3.16: Demonstration of >10 kHz noise reduction using late-time filtering.

have a very clear and repeatable onset, and the first recognizable peak is chosen to be the time alignment point, as shown in Figure 3.17a. The position and polarity of this initial peak depend on the distance from source to receiver, but for sferics originating in the same location, the first peak is consistently in the same place. Not surprisingly, the polarity of the return stroke changes the polarity of the sferic (Figure 3.17b), so that sferics launched from the less common positive lightning discharges must be inverted before including them in the averaging. For the cases considered in this work, the distribution of sferic amplitudes of those included in the averaging spans approximately a factor of 4, with the majority of sferics having a peak amplitude near the center of this distribution. This shows that the average spectra computed are not dominated by a single (or a few) sferics.

Some sferics are excluded from the averaging for a number of reasons. A second sferic sometimes arrives soon after the first, as shown in Figure 3.17c, which if included would add too much noise to the average. Sometimes, as shown in Figure 3.17d, the onset of the sferic is corrupted by earlier activity, possibly due to a separate sferic or

a pre-return-stroke lightning process that radiates at VLF [Arnold and Pierce, 1964]. Figure 3.17e shows a sferic with an unusually smooth onset (which probably implies a slower rise time in the current) and a general sferic shape that is unlike the “normal” ones in Figures 3.17a and 3.17b. These latter two cases are excluded because their sferic time alignment points are not well defined.

For this July 22, 1996, 0415–0445 UT time period, there were 59 sferics launched from the region 37.3°–37.8°N and 99.4°–99.9°W that met the criteria to be included in the averaging. The first 18 ms of each sferic were included in the averaging. Figure 3.18 shows the average sferic waveform and its spectral amplitude, each on two different scales to highlight the details of each signal. A comparison of these with the waveforms and spectra of individual sferics in Figure 3.15 clearly shows that the averaging improves the signal-to-noise ratio and reinforces the fine spectral features that form the basis of the *D* region measurement.

3.3.3 Spectrum Matching Procedure

It was shown in Section 3.2.1 that by increasing or decreasing h' , the sferic spectrum is shifted right or left, respectively, while retaining its general shape. This feature suggests that a model exponential ionosphere can be matched to the observed spectrum by iteratively varying h' until the modeled spectral peaks are aligned in frequency with the observed peaks. The parameter β can be inferred (as accurately as possible given the uncertainties discussed in Sections 3.2.3–3.2.5) in a similar manner by varying it in the model calculations until the modal interference peaks are of the proper amplitude. In order to make this measurement in an objective manner, it is necessary to use an automatic procedure for determining the quality of agreement between the observed and model spectra.

Since the return stroke waveform and therefore the coarse spectral details are not known, a direct comparison of the spectral amplitudes is not the best way to proceed. The information about the ionosphere is contained in the *fine* spectral details, which therefore must form the basis for our comparison. To do this, the sampled theoretical and observed spectral amplitudes are reduced to the *spectral detail vector*

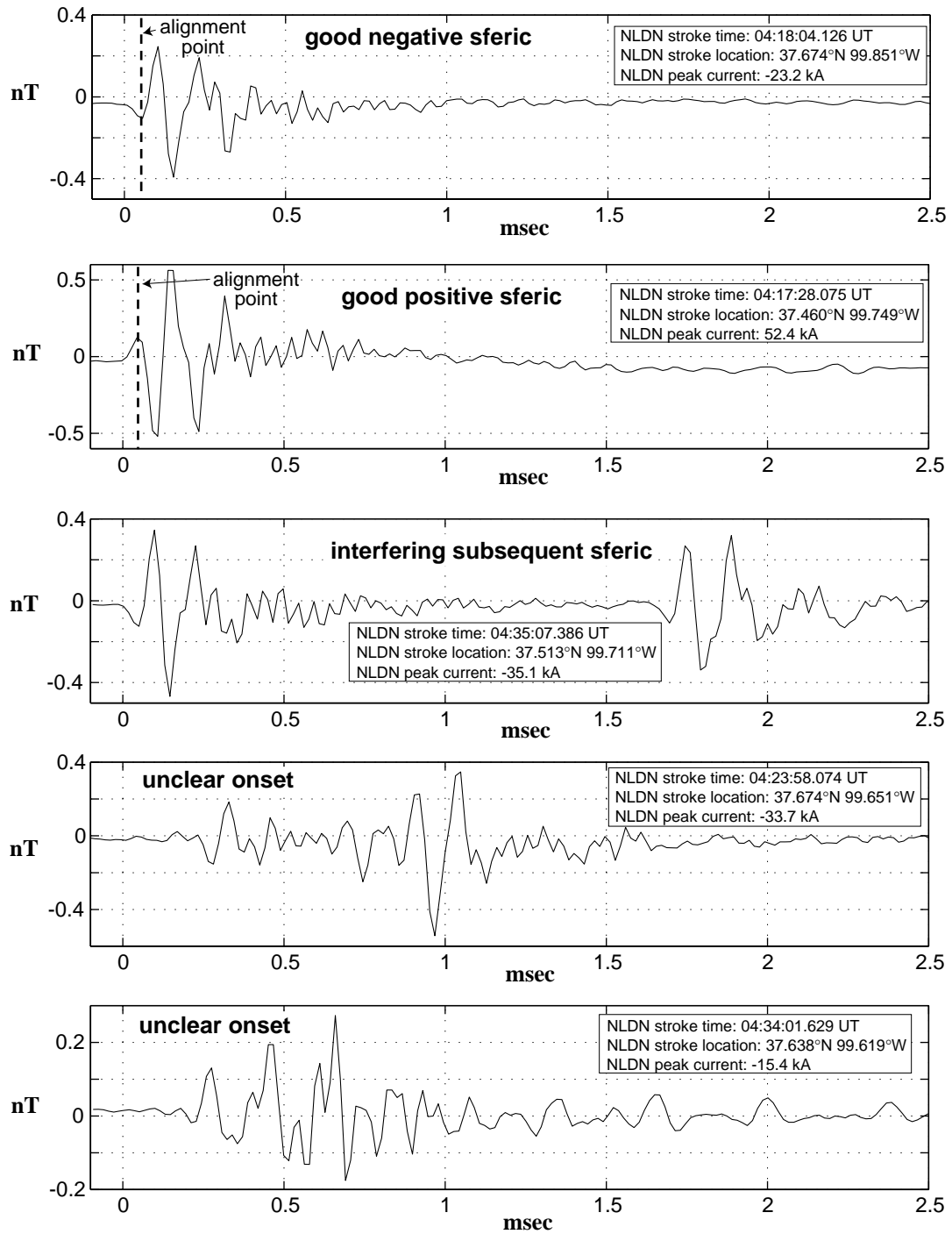


Figure 3.17: Examples of acceptable and unacceptable sferic onsets.

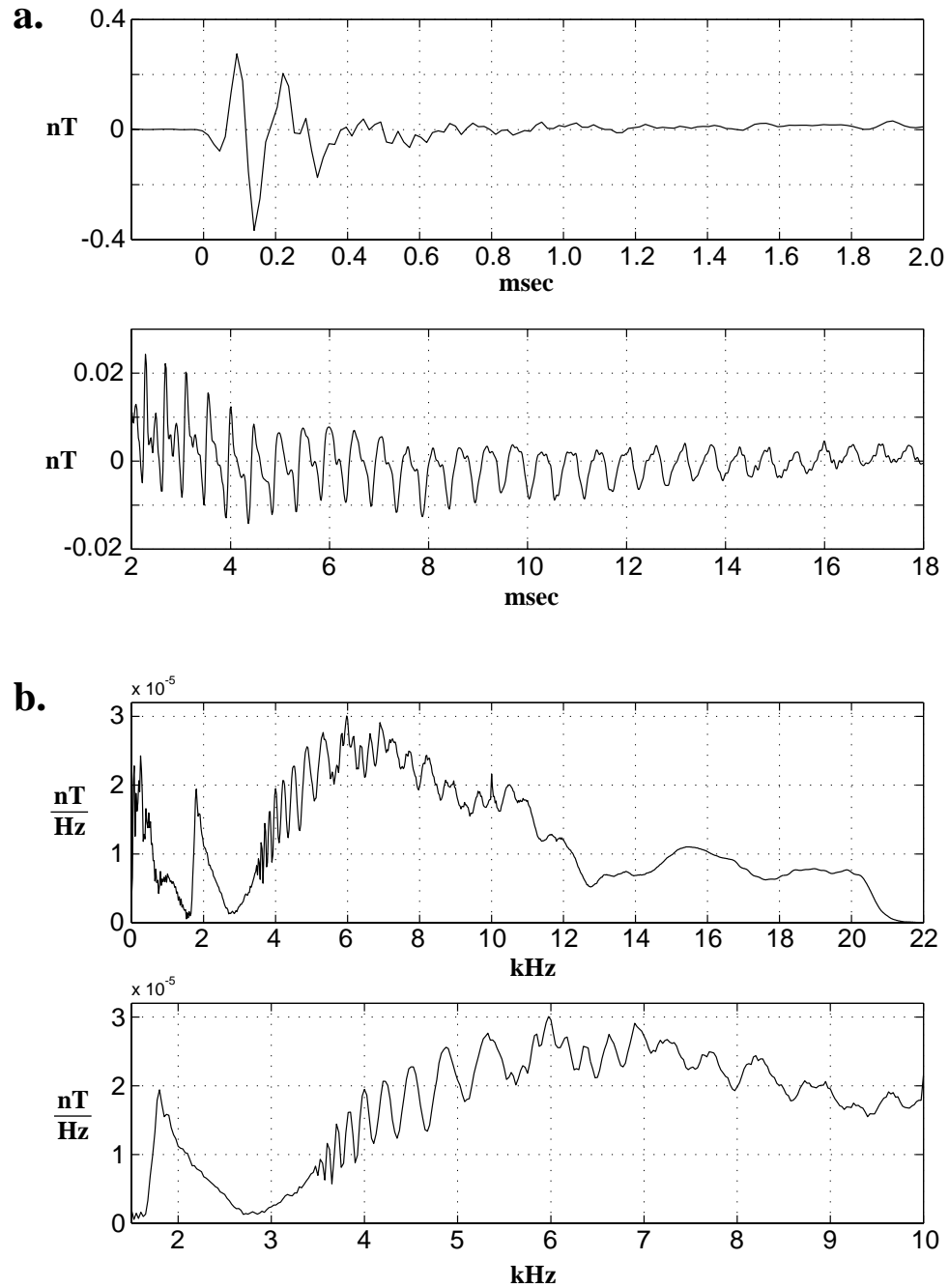


Figure 3.18: Average sferic waveform (a) and spectrum (b) calculated from 59 individual sferics.

D by the following procedure, which is demonstrated in Figure 3.19. The original sampled spectral amplitude (either theoretical or observed) is digitally FIR filtered (using Matlab’s *filtfilt* routine so there is no net phase shift) to obtain a smoothed spectrum. The original spectrum is then divided by the smoothed spectrum to yield the detail vector *D*. Dividing, rather than subtracting, ensures that the details are normalized to the amplitude of the smoothed spectrum. The vector *D* should be as independent as possible of the broad spectral variations contributed by the return stroke waveform. Figure 3.19c shows that *D* is essentially the same for a theoretical spheric spectrum launched by a “normal” discharge (described by 2.17 with the return stroke parameters from Section 2.6.3) and for an impulsive discharge ($Ih = \delta(t)$).

The quality of fit parameter *F*, which determines the quantifies the agreement of the details between two spectra, is defined as $F = \sum |D_{observed} - D_{theoretical}|$, summed over frequencies from 3 to 14 kHz, where most of the detail in which we are interested resides. A smaller *F* indicates better agreement between theory and observation, and the location of the minimum as a function of *h'* and β gives the extracted ionospheric parameters. The choice of the L_1 norm [Golub and Van Loan, 1989, p. 53] in the definition of *F* is somewhat arbitrary, but tests show that using another comparable norm (such as L_2) does not change the location of this minimum. Frequencies below 3 kHz are excluded because they consistently show variations that are not predicted by the propagation model which are probably due to interference with the QTEM mode, the propagation of which is influenced by the *E* and *F* regions of the ionosphere and is therefore not as useful in making this *D* region measurement.

Figure 3.20a shows a contour plot of the quality of fit parameter *F* vs. β and *h'* for the observed average spectral amplitude shown in Figure 3.18. The location of the minimum of *F* in β -*h'* space gives the best fit ionospheric parameters inferred by this technique. There is a distinct minimum at $h' = 83.2$ km and $\beta = 0.49$ km⁻¹ that is broader in β than in *h'*, indicating that the extraction is much more sensitive to *h'* than to β . The plot also shows that a change in *h'* of only 0.2 km produces distinguishably worse agreement (as determined by *F*), giving some indication of the precision of this measurement. The inferred electron density profile from these two parameters for $N_e = 10^0$ – 10^3 cm⁻³ (which is the range of N_e to which the VLF

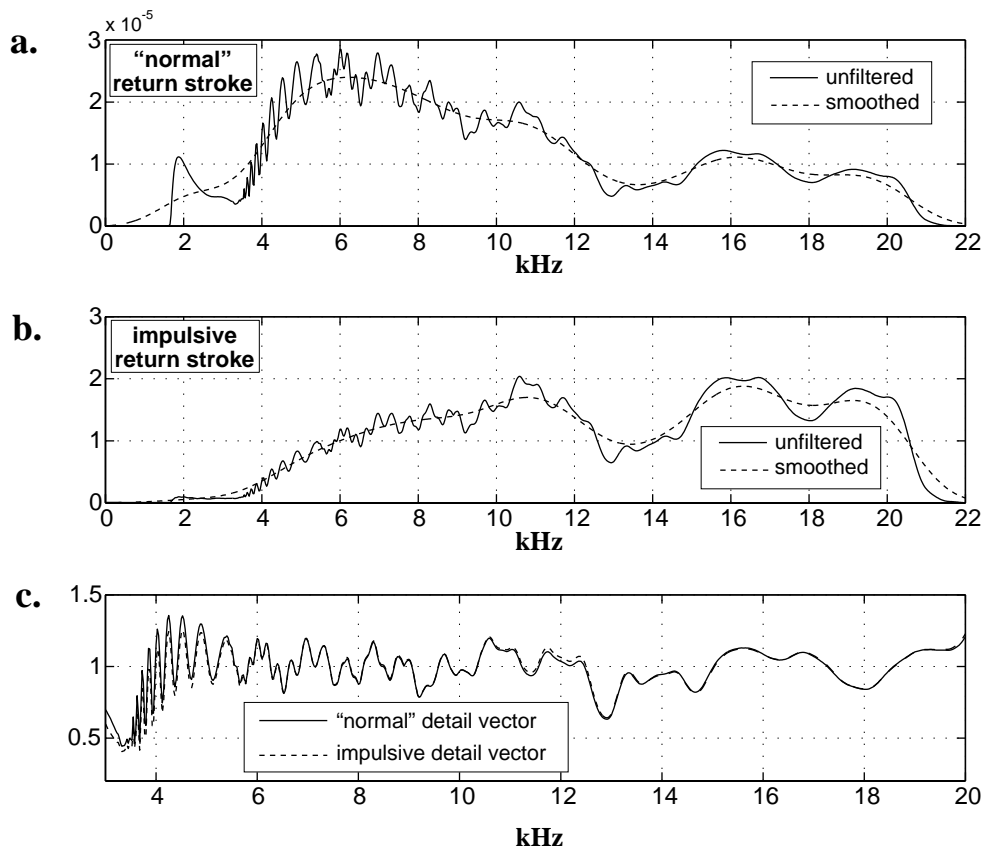


Figure 3.19: Demonstration of spectral detail extraction. a: The unsmoothed and smoothed spectra for a normal discharge. b: The unsmoothed and smoothed spectra for an impulsive discharge. c: The spectral details for each case, which are nearly identical.

propagation is sensitive, as was discussed in Section 3.2.2) is shown in Figure 3.20b.

Figure 3.21 displays the final comparison between theory (using the best fit ionosphere as determined above) and observation. Figure 3.21a shows the spectral amplitudes on two different frequency scales to highlight the fine detail, and Figure 3.21b shows the magnetic field waveforms on two different time scales. The best fit h' and β found by the above procedure does yield good visual agreement between the observed and modeled spheric spectra. A change in h' of 0.2 km produces a noticeable misalignment in the interference peaks, reinforcing the precision of this measurement

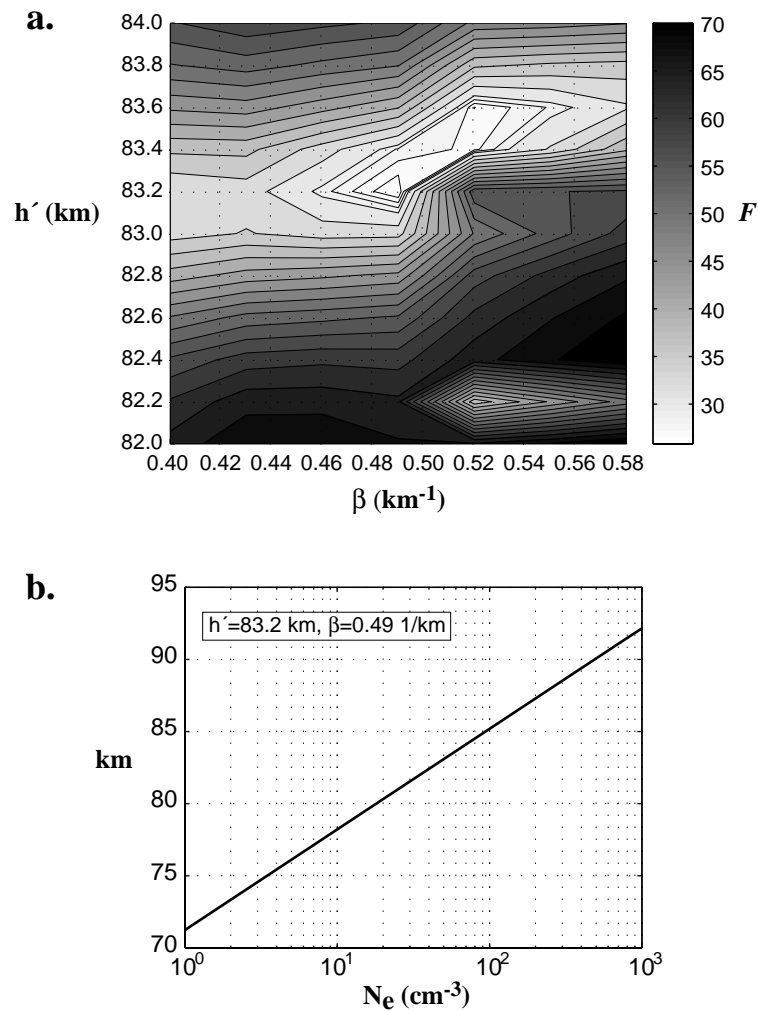


Figure 3.20: Extraction of ionospheric parameters from measured spectral details. a: Contour plot of F vs. β and h' . The minimum gives the best fit ionosphere for this particular observation. b: The best-fit inferred D region electron density profile.

as determined by the contour plot of F . Little can be said about the absolute accuracy of this measurement without comparison with a different technique capable of the same path-averaged D region measurement. As discussed in Section 3.2.6, this inferred electron density profile is defined relative to the mean ground altitude of the propagation path.

The modeled spectrum and waveform in Figure 3.21 were calculated using a model

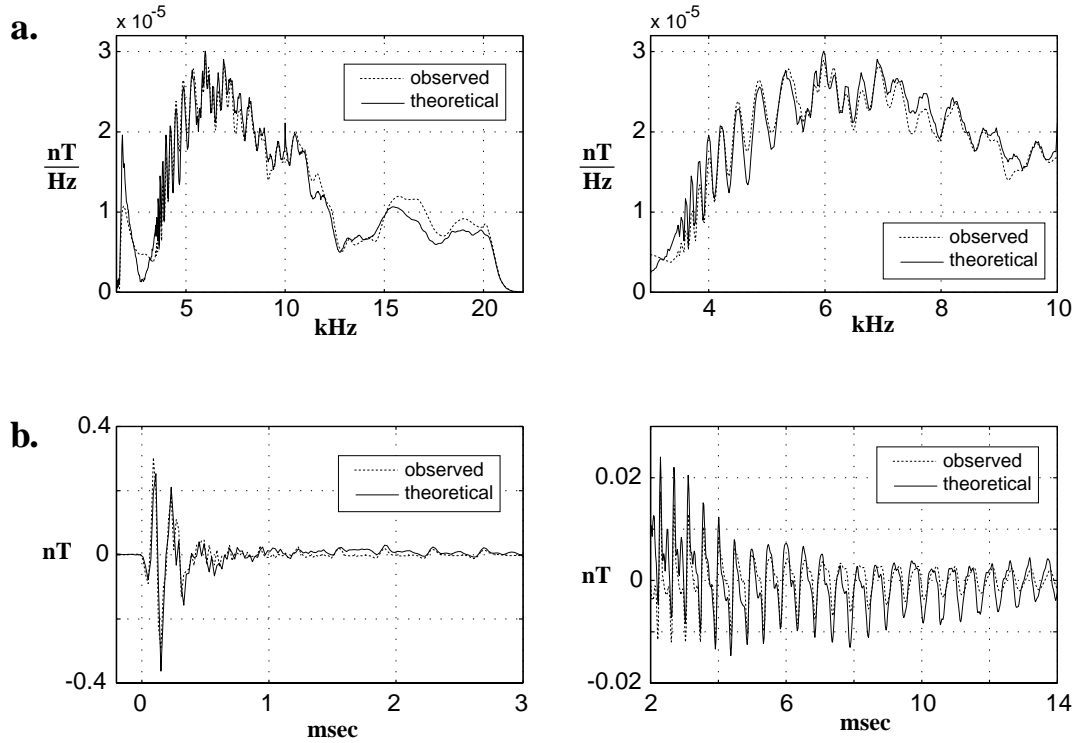


Figure 3.21: Final agreement between theory and observation. a: Sferic spectrum. b: Sferic waveform

return stroke with parameters $a = 10^4 \text{ sec}^{-1}$, $b = 3 \times 10^5 \text{ sec}^{-1}$, and $i_{g0} = 34 \text{ kA}$, in the notation of Section 2.6.3. These parameters were chosen to give good visual agreement between the broad spectral amplitude of the theoretical and observed spectra to highlight the overall agreement between the modeled and observed spectra. By varying the return stroke parameters to achieve good agreement with an observed spectrum, the return stroke waveform can be inferred from average or individual sferics. The difficulty in attempting to do this using the Bruce-Golde return stroke model given in (2.17) is that the parameters are not independent. The maximum current-moment can be increased by increasing i_{g0} , increasing v_0 , or decreasing γ , and the risetime can be increased by increasing either b or γ . Return stroke parameters can be chosen to agree with observations, but the choice is not unique, so there is uncertainty in any measurement of this type.

Latitude	Longitude	Return Stroke Parameters
28.1°–28.5°N	108.9°–109.2°W	$a = 2 \times 10^3 \text{ sec}^{-1}$, $b = 5 \times 10^4 \text{ sec}^{-1}$, $i_{g0} = 40 \text{ kA}$
35.2°–35.4°N	104.5°–104.8°W	$a = 2 \times 10^3 \text{ sec}^{-1}$, $b = 2 \times 10^5 \text{ sec}^{-1}$, $i_{g0} = 32 \text{ kA}$
35.8°–36.2°N	87.5°–88°W	$a = 2 \times 10^4 \text{ sec}^{-1}$, $b = 2 \times 10^5 \text{ sec}^{-1}$, $i_{g0} = 46 \text{ kA}$
45.8°–46.4°N	91.1°–92.3°W	$a = 5 \times 10^3 \text{ sec}^{-1}$, $b = 2 \times 10^5 \text{ sec}^{-1}$, $i_{g0} = 34 \text{ kA}$

Table 3.1: Four sferic source regions and the return stroke parameters used to calculate the modeled spectra shown in Figure 3.22.

3.4 Two Case Studies

We now apply the above procedure for extracting β and h' from sferic measurements to two broader case studies. The first study uses simultaneous ionospheric measurements from a number of sferic locations to provide a large-scale picture of the *D* region over the U.S. during a single 30 minute period. The second uses multiple ionospheric measurements from a single sferic location over a 40 minute period centered at sunset at the receiver, during which period the ionosphere changes significantly.

3.4.1 Simultaneous, Multiple Location Ionospheric Measurements

Using the same time period as in the previous example (July 22, 1996, 0415–0445 UT), we infer *D* region electron densities along a number of different sferic propagation paths, both to verify the consistency of the ionospheric parameter extraction along paths that overlap and to produce simultaneous *D* region measurements over a large portion of the continental United States. The four locations (in addition to that of the previous example) that had enough lightning to produce a satisfactory measurement are listed in Table 3.1. The 46°N 92°W region was expanded beyond 0.5° by 0.5° to include more discharges to improve the sferic averaging. The return stroke parameters used to produce the modeled spectra for these four locations are also listed in 3.1.

Figure 3.22 shows, for each location, the measured average spectrum and the best-fit modeled spectrum on which the ionospheric measurement is based. For the three

southern locations, the agreement in the alignment of the fine features between theory and measurement is comparable to the agreement displayed for the previous example in Figure 3.20. For the 28°N 109°W and 35°N 104°W locations, the broad differences between the spectra near 8 kHz is indicative of the disagreement between the assumed and actual lightning return stroke spectrum. The fact that the fine-features between 3 and 14 kHz agree well with the model indicates that the inferred electron density profile is accurate.

For the 46°N 92°W location, the agreement is not as good. Even with the expanded geographic area for sferics, only 16 clean sferics were recorded during the 30 minute period and included in the averaging, which is too few for averaging to be effective (the other three locations had 43, 42, and 86 sferics, from south to north, included in the average spectra). However, even with only 16 sferics, the fine spectral features are distinguishable, which still allows us to assess the state of the ionosphere. The agreement in the position of the fine spectral features is good, but the amplitude and sharpness of these variations in the theoretical spectrum appears to be too low across the entire frequency range. This aspect suggests that a spectrum with a higher value of β might have produced a better fit than the spectrum shown. However, even with the relatively noisy observed spectrum, h' appears to have been extracted accurately.

Results and Discussion

Figure 3.23a shows a map of the propagation paths to Stanford from these four locations and the one analyzed in Section 3.3. Each path is labeled with the inferred ionospheric parameters (h' and β) for this period based on the spectral fits shown in Figure 3.22. For a geomagnetic perspective, the footprints of the geomagnetic L -shells of 2–4 are also shown.

It is difficult to place this measurement in the context of other measurements, because no simultaneous D region measurement over such a large geographic area has been made before. However, there is an obvious general trend of the ionospheric height decreasing with increasing latitude, with a total change of ~ 3 km over the entire probed region, with ~ 2 km of this change occurring in the southern portion of the region. As discussed in Section 3.2.6, the height of the inferred electron density

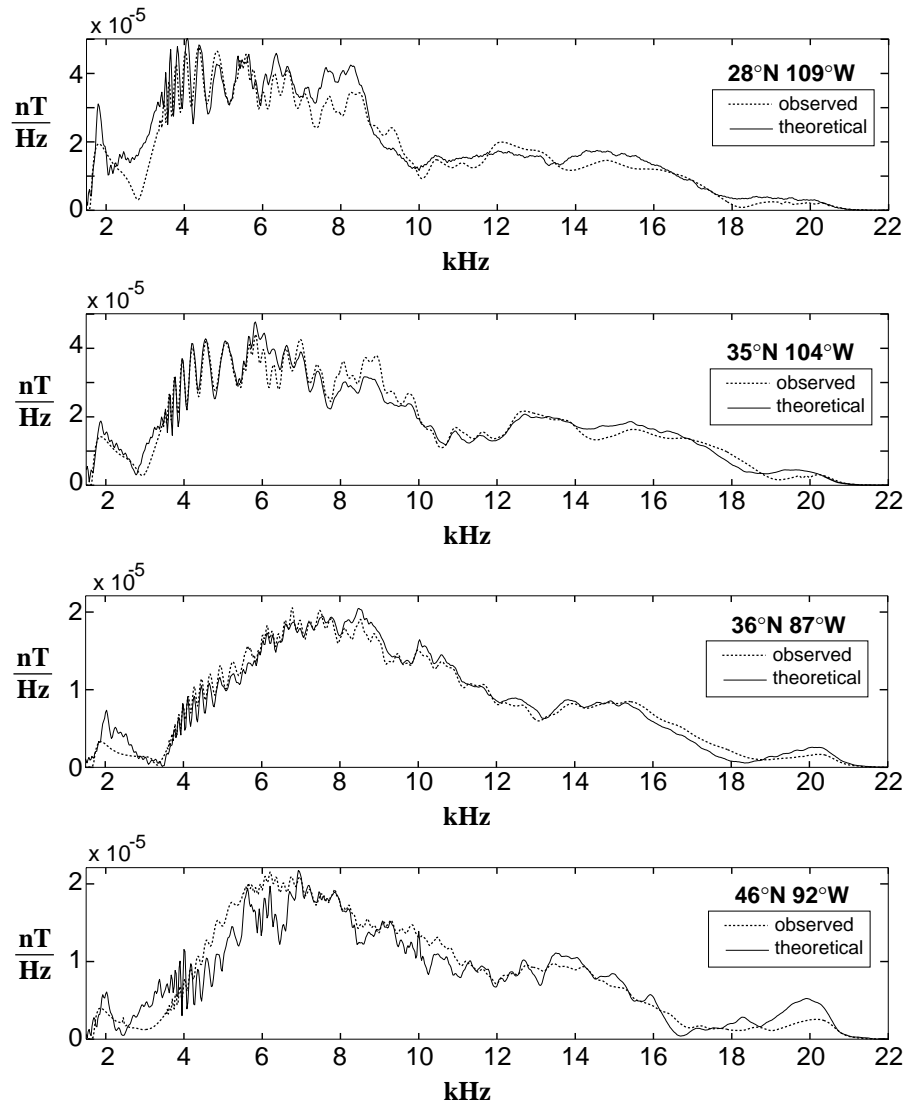


Figure 3.22: Observed and best fit theoretical sferic spectra on July 22, 1996 from 0415-0445 UT for sferics originating in the areas listed in Table 3.1.

profile is measured relative to the average ground altitude of the propagation path in question. Some of the observed height variation is likely due to ground height variations, which could be quantified if the mean ground altitude of the propagation paths were known.

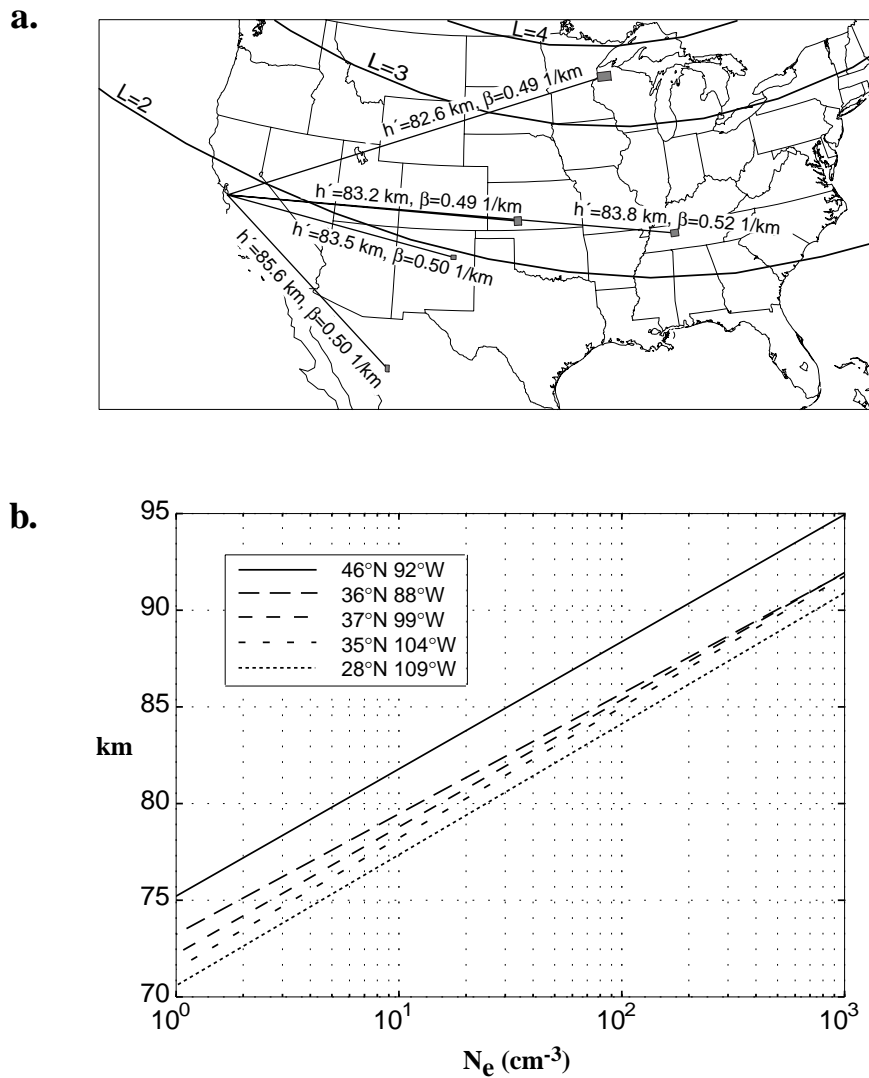


Figure 3.23: Multi-location ionospheric measurement. a: Map of propagation paths to Stanford labeled with extracted ionospheric parameters h' and β . b: The inferred electron density profiles for each of these paths.

The two overlapping propagation paths from $36^\circ\text{N } 88^\circ\text{W}$ and $37^\circ\text{N } 99^\circ\text{W}$ to Stanford show different path-averaged h' measurements. The fact that the section of propagation path contained only in the longer path has a higher ionosphere could be due to the fact that this section has a lower mean ground altitude, because of the

Rocky Mountains. Since the length of the shorter path is $\sim 60\%$ of that of the longer path, the ground-ionosphere height over the non-overlapping section must be 84.7 km ($0.6 \cdot 83.2 + 0.4 \cdot 84.7 = 83.8$) to be consistent with the observations. Much of this 1.5 km height difference may be due to the higher mean ground altitude on the shorter path. Part of this measured height difference may also be due to the fact that the eastern portion of the path is later in local time and farther removed from sunset, so that the ionosphere has had more time to relax after the disappearance of the solar ionizing radiation, leading to a higher ionospheric reflection height in the east.

This example highlights the potential of this technique for the measurement of the *D* region. With just a few more strategically placed receiving stations, these five source regions could produce path-averaged measurements along 20 or more propagation paths. An image of the ionosphere over the entire United States can in principle be produced by a tomographic reconstruction of the spatial variation of *D* region height and sharpness based on many path-integrated measurements.

3.4.2 Ionospheric Measurements During Sunset

We now apply the VLF measurement technique developed in this work to a single propagation path over a time period when the ionosphere is known to be changing, such as during sunset. The disappearance of the solar ionizing radiation causes a rapid recombination of many of the free electrons throughout the ionosphere, including the *D* region, leading to a typical increase of the VLF reflection height from ~ 70 km in the day to ~ 82 km at night [Rasmussen *et al.*, 1980]. This application tests the theoretical predictions of Section 3.2.1 which suggested that the lack of spectral details would make daytime *D* region measurements difficult.

Sferics received on May 25, 1997 which originated in the region of 37° - 37.5° N 99.5° - 100° W are used for this case. The location of this region and the propagation path is shown in Figure 3.24. Sunset at the ground at 37° N 100° W was at 0149 UT on this day, and sunset at Stanford was at 0318 UT [*U. S. Naval Observatory Web Site*]. The location of the day-night terminator (the boundary between daylight and night) at the ground at 0230, 0300, and 0330 UT is shown on the map. Lightning stroke

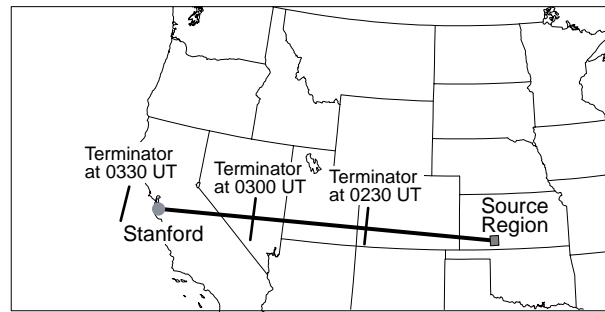


Figure 3.24: Map of propagation path and day-night terminator location on May 25, 1997.

rates in this small region were very high, leading to effective spheric averages in time periods as short as 5-10 minutes. The high time resolution is essential because the *D* region changes rapidly during sunset [Rasmussen *et al.*, 1980].

Figure 3.25 shows an overview of the evolution of the average spheric spectral amplitude from this location during 0240–0345 UT. A number of clear changes occur as the terminator moves across the path—the gradual appearance of the first order mode in the range of ~ 1.5 -3.0 kHz; the gradual appearance of modal interference oscillations between 3 and 10 kHz; and the evolution from a flat, featureless spectrum above 10 kHz to one with broad maxima and minima like the nighttime spheric spectra shown in the previous sections. These changes can be attributed to the expected upward movement of the ionospheric reflection height over this period. The collision frequency at the reflection altitude decreases, reducing attenuation rates for the modes near cutoff which are launched nearly vertically.

The ionospheric parameters are extracted from five of these spectra which cover the period during which sunlight disappears completely from the propagation path: 0300, 0310, 0320, 0330, and 0340 UT. At 0340 UT, the modal interference variations between 3 and 10 kHz are present, but not quite at the level of the nighttime observations shown in Section 3.4.1. At 0300 UT, these same variations are essentially absent, and the spectral details-based measurement technique does not work well. For the 0300 and 0310 cases, the quality-of-fit function F has a very broad (in h' and especially in β) and shallow minimum, implying that the extraction of h' and β is much

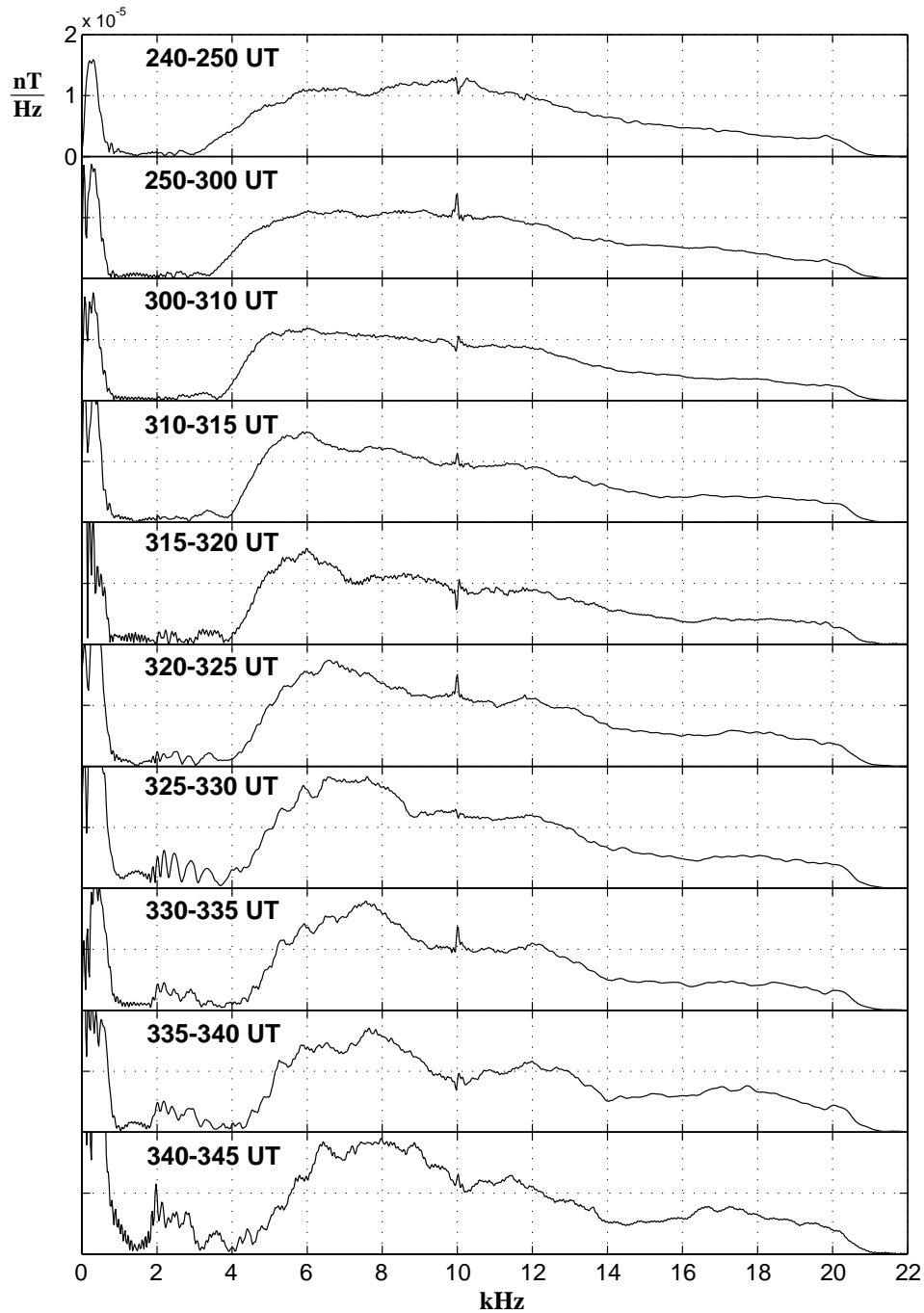


Figure 3.25: Evolution of observed average sferic spectrum on a single propagation path as the terminator moves west across the path. The vertical scale on each graph is the same.

less certain than it was in Section 3.4.1. For this reason, the best fit ionosphere was determined partially by with F and partly by visual alignment of the small variations between 5 and 6 kHz.

Figure 3.26a shows the observed and best-fit theoretical spectra for these 5 time periods. For the 0340, 0330, and 0320 UT periods, the agreement is fairly good, but not as striking as for the nighttime cases due to the relative lack of spectral features. For the 0310 and 0300 UT periods, the agreement is almost completely determined by the very weak variations between 5 and 6 kHz. Figure 3.26b shows the electron density profile variation during this period. The measured trend of an ionosphere moving up from $h' = 79$ to 81.5 km in this time period is qualitatively expected. The parameter β was only extracted to an accuracy of 0.05 km^{-1} because of the relatively large uncertainty of the quality of agreement between theory and observation for these spectra with few fine features.

This example demonstrates the shortcomings of this method for measuring daytime ionospheres, namely that the spectral details which are necessary for the measurement are absent in daytime. It is possible that some feature other than the modal interference pattern could be used as a discriminator for daytime ionospheres; however, no such feature is readily apparent in these observed spectra.

The rapid appearance of frequencies between 1.5 and 3 kHz between 0300 and 0340 UT as can be seen in Figure 3.26a merits some discussion. It is unlikely that this phenomenon is due to a rapid change in the average lightning return stroke spectrum, thus it is almost certainly an ionospheric effect. During this time period, the ionosphere changes most rapidly at the end of the path closest to the receiver. When the ionosphere at the end of the path is significantly denser than that for the remainder of the path, there is a rapid change in the cutoff frequencies of the waveguide at this inhomogeneity, and frequencies near 1.5–2.0 kHz that were propagating under the higher ionosphere are below cutoff under the lower ionosphere, and attenuate rapidly. As the ionosphere at the end of the path rises, this effect quickly disappears, so that modes near cutoff can change very quickly while the path-averaged ionosphere does not change as much because the change is only over a small portion of the path. Thus, in the presence of a significant ionospheric inhomogeneity such as that due

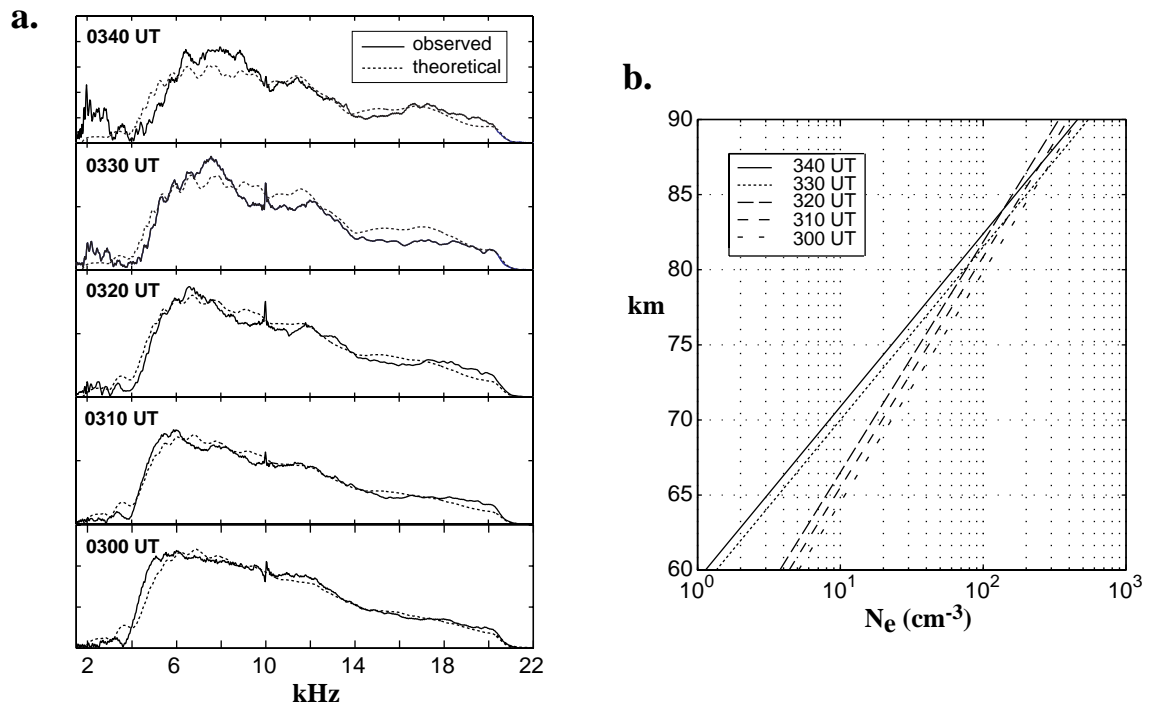


Figure 3.26: Single-location ionospheric measurement. a: Observed and best-fit theoretical sferic spectra from 0300–0340 UT. b: Inferred variation of the path-averaged ionospheric electron density.

to the day/night terminator, modes near cutoff are strongly affected by the local ionospheric conditions rather than the path-averaged ionosphere. This conclusion is hinted at by the ionospheres considered in Figure 3.11, in which the inhomogeneous ionosphere produces a sferic with lower spectral amplitude from 1.5–3 kHz than for the homogeneous ionosphere. However, the inhomogeneities responsible for the observed effect in Figure 3.26 must contain an ionospheric height change greater than the 5 km considered theoretically in Section 3.2.4.

Chapter 4

Lightning Current-Moment Waveform Measurements Using ELF Sferics

There are three components to the linear system which describes subionospheric VLF and ELF propagation: the source current-moment waveform (the input), the propagation effects (the system), and the magnetic field sferic waveform (the output). The previous chapter used a numerical model to estimate the details of the ionosphere from average sferic measurements by assuming that the source current-moment waveform and spectrum were smoothly varying. Sferic measurements can also be used to estimate the source current-moment waveform of individual sferics, provided that the propagation effects are either known or accurately modeled. Chapter 3 showed clearly that the propagation effects at VLF can be modeled accurately with the sferic propagation model described in Chapter 2.

In this chapter, a sferic-based current-moment measurement technique is applied to a specific kind of lightning discharge—those which create the mesospheric optical emissions known as sprites. Previous work has shown that sprites are associated with lightning discharges that launch sferics containing an unusually high amplitude at ELF frequencies (<1.5 kHz) [*Bocippio et al.*, 1995; *Reising et al.*, 1996]. This result implies that the source current-moment waveform must contain large, slowly varying

(>1 ms) currents, and that these large, slowly-varying currents are associated with sprite production.

The primary effect of such slowly-varying currents is to move a large quantity of charge in a single lightning stroke, and the fact that it takes such a discharge to create a sprite is in general agreement with theoretical models of sprite production. One theory proposes that these large slow currents, by moving large amounts of charge from the cloud to the ground, create intense quasi-electrostatic fields in the ionosphere which can heat the ambient electrons to levels exceeding the threshold for the generation of optical emissions via electron impact on atmospheric constituents [Pasko *et al.*, 1997]. Another set of theories proposes that optical emissions may be produced by runaway electrons driven upward by the same quasi-electrostatic fields [Bell *et al.*, 1995b; Roussel-Dupre and Gurevich, 1996; Taranenko and Roussel-Dupre, 1996; Lehtinen *et al.*, 1997].

Due to the highly nonlinear nature of each of these mechanisms, both theories predict a sharp threshold in the quantity of charge-moment change from the lightning discharge necessary for the creation of the sprite. This threshold depends on uncertain parameters such as the pre-discharge charge configuration in the cloud and the ambient ionospheric conductivity, but a predicted charge-moment threshold of ~ 1000 C·km to produce optical emissions at 75 km altitude is reasonable in the context of the quasi-electrostatic heating theory [Pasko *et al.*, 1997]. More charge-moment transfer is required to create optical emissions below 75 km (~ 4000 C·km for emissions at 60 km), and less is required above this altitude. Runaway electron simulations by Lehtinen *et al.* [1997] show that a larger charge-moment change is required to create significant optical emissions at observed sprite altitudes (~ 60 – 90 km) through the runaway mechanism, a change of approximately 2250 C·km in 1 ms. The runaway theories of Roussel-Dupre and Gurevich [1996] and Taranenko and Roussel-Dupre [1996] contain different assumptions about ambient atmospheric conditions, and respectively predict charge-moment thresholds for sprite-production of 1800 C·km in 10 ms and 1350 C·km in 5 ms.

A remote measurement of charge-moment change in sprite-producing discharges is critically important to test the validity of these models. As discussed in Section 1.3,

lightning charge and current measurements are in general difficult to make at a point distant from the discharge, but a sferic-based technique is capable of making this measurement remotely.

4.1 Measurement Technique

As mentioned above, the approach taken in solving this problem is to treat the propagation process as a linear, time invariant system. The “system” in this case is a combination of all of the propagation effects: the receiver and source locations, the ionospheric conditions, and the particular output field of interest. Time invariance of this system is achieved if the system (i.e. the path-averaged ionosphere, which is the only time-varying aspect of the system) does not change significantly over the duration of a single input waveform, which is a very reasonable assumption in this case since sferic waveforms typically last at most a few tens of milliseconds. Although the nighttime ionosphere is highly variable, these variations occur over time scales of seconds to hours.

The input to the system in this case is the vertical lightning source current-moment (current times channel length) waveform. The output of the system is the received horizontal magnetic field waveform. Since the system is linear and time-invariant, it can be completely specified by its impulse response, or the output waveform to an impulsive vertical current-moment at the input. If this impulse response is known, then the output waveform can be found for a completely arbitrary input function by the convolution of this input with the impulse response [Bracewell, 1986, p. 179].

The problem to be solved is not the forward, *convolution* problem but rather the inverse, *deconvolution* problem. The output of the system (i.e. the sferic) is observed, and we wish to find the input. To do this, we have to specify the other unknown of the equation, the system impulse response. Since this is not an easily measurable quantity, it must be modeled as accurately as possible. The results of Chapter 3 show that with the MODEFNDR program, VLF (>1.5 kHz) propagation can be modeled accurately if the right ionospheric conditions can be inferred and used in the model.

For this problem, ELF (<1.5 kHz) propagation must also be modeled accurately

since it is the ELF component (i.e. QTEM waveguide mode) of the sferic that contains the information on the slow time scale currents that are known to be important in sprite production. In fact, the VLF (i.e. non-QTEM) components of the received sferic can be ignored in measuring the quantity of charge-moment transfer to create a sprite. Published fast time resolution optical observations of sprites have shown that they usually occur at least 1 ms after the source lightning stroke [Rairden and Mende, 1995; Winckler *et al.*, 1996; Fukunishi *et al.*, 1996; Inan *et al.*, 1997; Cummer *et al.*, 1997]. Thus the information on the return-stroke dynamics on time scales shorter than ~ 1 ms, which is provided by the VLF portion of the observed sferics, appears to be unimportant to the issue of sprite production. It should be noted that this filtering only slows the perceived rate of charge transfer and does not limit our ability to measure the total magnitude of charge transfer occurring on faster time scales. This issue is discussed fully in Section 4.4.2.

The observed sferics are digitally filtered with a 10th-order FIR filter with a cutoff frequency of 1 kHz (at a 10 kHz sampling rate), using a zero-phase implementation [Oppenheim and Schaffer, 1989, p. 285] (Matlab's *filtfilt*) that doubles the effective filter order. The resultant frequency response of this filtering operation is shown in Figure 4.1. The modeled sferic spectrum in Figure 2.8 and the observed sferic spectra in Figure 3.18a show that such a filter removes the non-QTEM modes above ~ 1.5 kHz without significantly affecting the QTEM mode (for which attenuation increases with frequency).

The two steps involved in our extraction of the source current-moment waveform are to model the ELF/QTEM propagation impulse response, and to use deconvolution to extract the source current-moment waveform from individual observed ELF sferics which contain frequency content from ~ 10 –1500 Hz and which last for ~ 10 –20 ms. Each of these steps are described in detail below in Section 4.3.

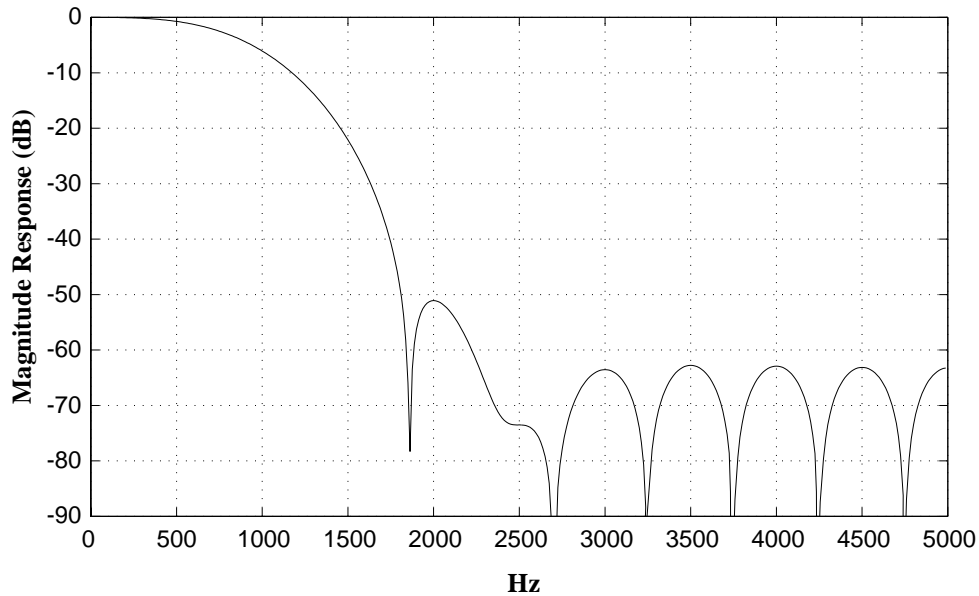


Figure 4.1: Frequency response of filter used to remove all non-QTEM sferic components.

4.2 ELF Sferic Observations

4.2.1 Data Acquisition

The time period to be examined in this chapter is July 24, 1996, from 0400–0600 UT, a period during which many sprites occurring in the vicinity of 37°N 100°W were directly observed on video recordings made at Yucca Ridge, Colorado with a system described in *Inan et al.* [1997].

The observed sferics in this chapter were recorded at Stanford on a system slightly different from that used in Chapter 3. The loop antenna used is oriented precisely in the magnetic east-west plane (thus $\sim 17^\circ$ south of geographic east based on the magnetic declination at Stanford). The receiver used is designed for ELF recording, with the frequency response of the recorded channel rolling off above ~ 3 kHz but extending to significantly below 10 Hz at the lower end. The precise lower cutoff is likely dominated by the frequency response of the PCM encoder used to record

the signal on a Betamax tape. The signal is recorded and extracted in the manner described in Section 3.1.2.

Accurate absolute calibration of the recorded ELF signal is critical for this application because the sferic amplitudes will be quantitatively interpreted. However, there is no easily-interpreted calibration signal injected onto the recorded ELF channel. In this work, the ELF channel was calibrated by a comparison to the calibrated VLF channel in the 1–2 kHz frequency range, where both channels have a flat frequency response. The fact that the ELF and VLF loop antennas do not point in the same direction must be accounted for, as the amplitude received on each loop is proportional to $\cos \theta$, where θ is the angle between the plane of the loop and the arrival direction of the sferic. Thus the location of the individual sferic (which is not necessarily a sprite-associated sferic) used for this calibration must be known from NLDN data so the $\cos \theta$ factor can be accurately computed for each antenna.

4.2.2 Removal of Power Line Interference

Because of the flat frequency response extending to below 10 Hz, power line fields at 60 Hz and its harmonics forms a large part of the recorded signal, an example of which is shown in Figure 4.2a. As much of this interference as possible must be removed in a way that does not distort the sferic waveform. An effective noise removal technique is isolate the interference waveform and to subtract this noise-only waveform from the observed waveform, leaving only the signal of interest. Because the 60 Hz interference is essentially stationary (i.e. it does not change significantly) on time scales of less than a second, the noise-only waveform could be taken from before or after the section containing the signal of interest. However, it is very difficult to find a section of data long enough to use as the noise-only waveform that does not contain any significant sferics.

It is easier to find a single 60 Hz period that can be replicated to create an artificial noise waveform. The first 60 Hz period (16.667 ms) in Figure 4.2a is zero-phase low-pass filtered at ~ 2 kHz to remove any sferics but leave the 60 Hz and the harmonics untouched. This 16.667 ms period is then replicated to form an interference waveform

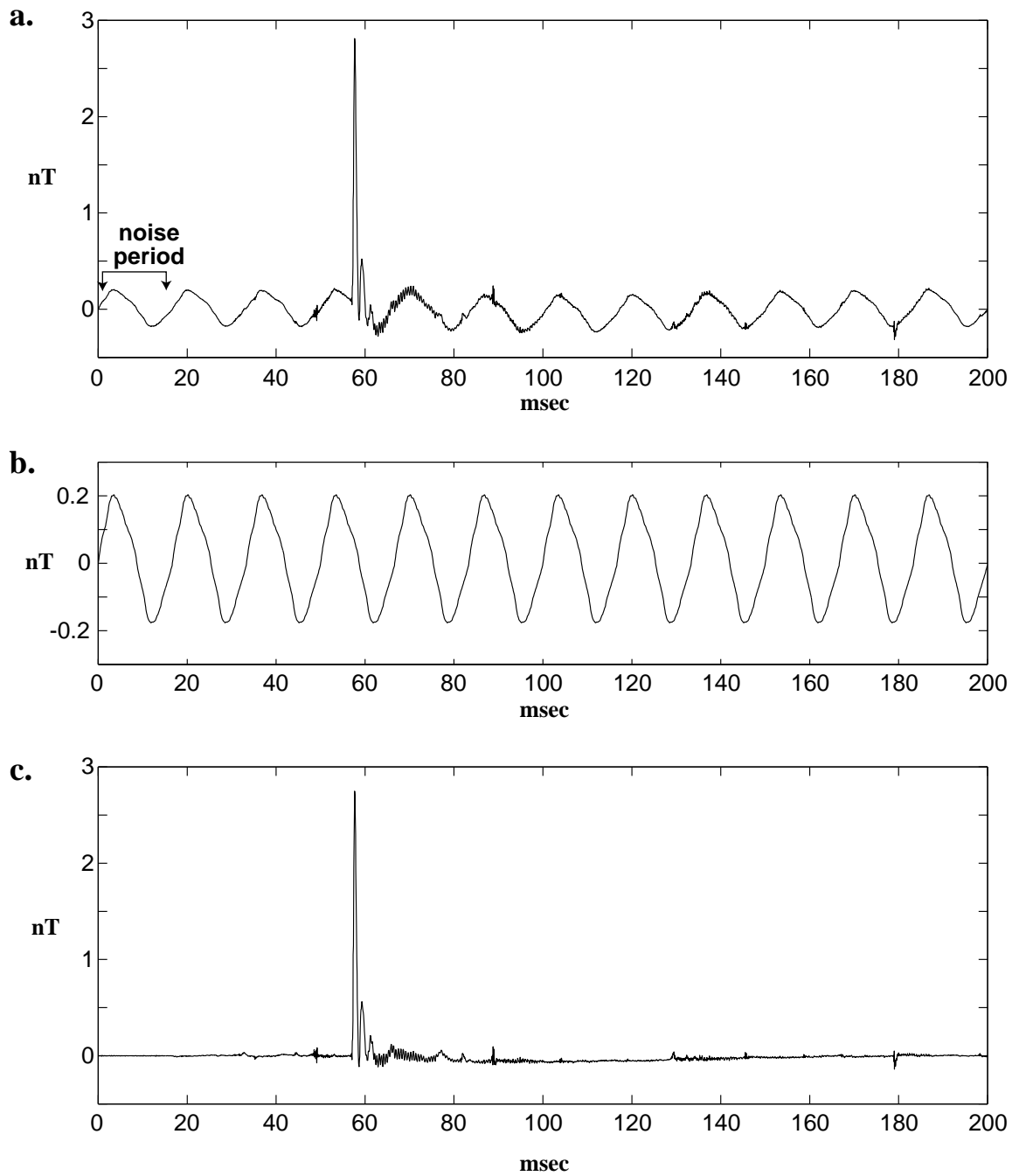


Figure 4.2: Noise removal from ELF sferics. a: Sample of ELF recording with desired sferic and 60 Hz noise. b: Artificial 60 Hz noise waveform. c: De-noised sferic constructed by subtracting artificial noise from original signal.

of the same length as the original signal, as shown in Figure 4.2b. The noise waveform can be extended to an arbitrary length, but care must be taken to ensure that the waveform is continuous from the beginning to the end of each noise period so that it is smoothly varying. This artificial noise waveform is then subtracted from the observed waveform to produce an interference-free waveform, as shown in Figure 4.2c. This technique works well in removing most of the 60 Hz noise without distorting the observed sferic waveform, and is applied to produce all of the observed sferic waveforms examined in this chapter.

4.3 Modeling the ELF Impulse Response

One of the two steps in measuring the source current-moment which radiates a measured ELF sferic is the modeling of the ELF propagation impulse response, defined as the sferic radiated by an impulsive current-moment waveform of a known amplitude as it would be observed at the receiver. The sferic propagation model described in Chapter 2 is used for this purpose, but only the QTEM mode is considered. For each individual sferic to be considered, the source location is known from the NLDN data, and the ground, magnetic field, collision frequency, and ion density are assumed to be the same as given in Chapter 3. The only unknown parameter is the ionospheric electron density profile over the propagation path.

4.3.1 The Dependence of QTEM-Mode Propagation on the *E* and *F* Region Electron Density Profiles

To investigate this dependence, the theoretical QTEM mode impulse is calculated for propagation from 37°N 100°W (the approximate location of the sprite-producing lightning discharges examined here) to the receiver at Stanford, for three different ionospheres. The *D* region electron densities are exponential up to 95 km (see equation 3.1) with $\beta=0.5 \text{ km}^{-1}$. Two of these profiles have $h'=85 \text{ km}$ and the other has $h'=83 \text{ km}$. The electron densities above 95 km are from the International Reference Ionosphere (IRI) [Rawer *et al.*, 1978], obtained with sunspot parameters of 10 (very

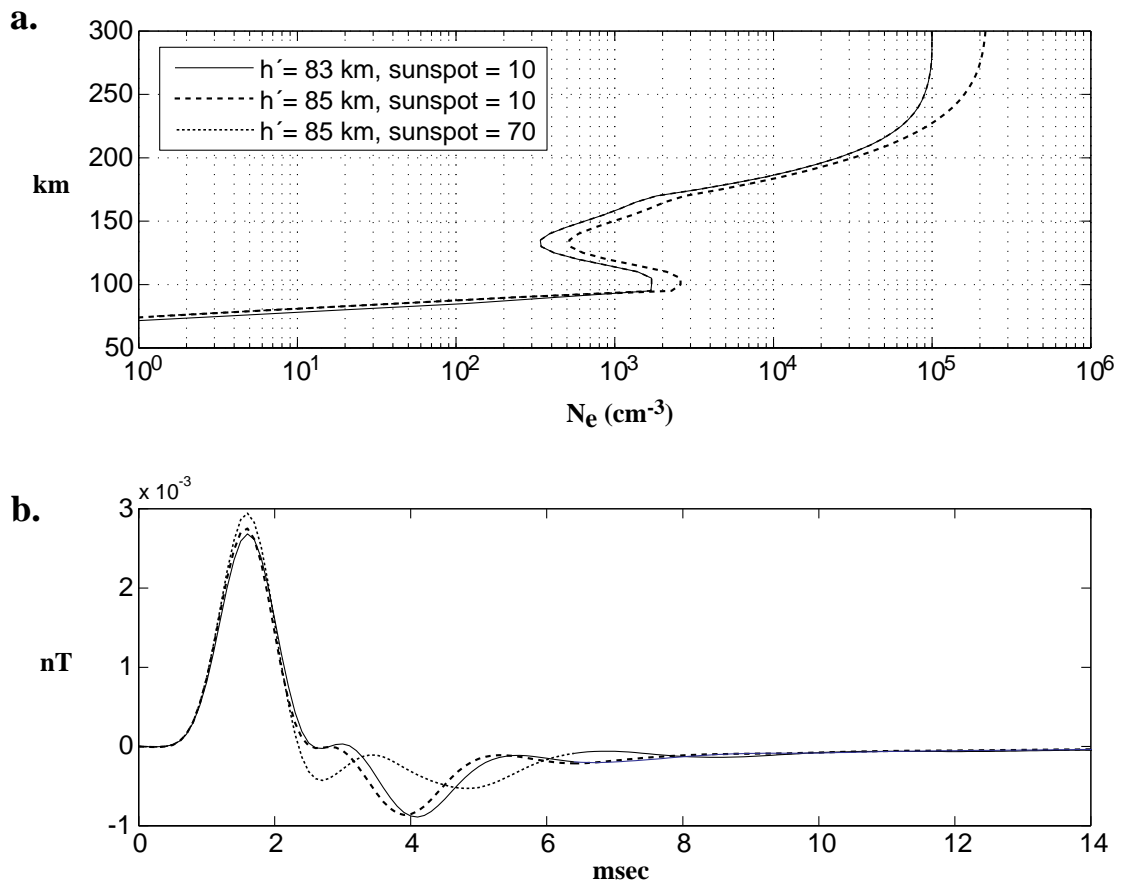


Figure 4.3: Demonstration of dependence of ELF impulse response on the ionosphere. a: Three ionospheres with different D and E regions. Two ionospheres are identical above 95 km, and two are identical below 95 km. b: Modeled ELF impulse responses for propagation under these three ionospheres.

quiet) and 70 (moderate). The IRI input location (37°N 100°W), month (July), and local time (midnight) are the same for all three ionospheres. The IRI model is used here to provide physically reasonable E and F region electron densities. These three composite electron density profiles are shown in Figure 4.3a.

For an impulsive discharge involving a charge-moment change of $1 \text{ C}\cdot\text{km}$, the modeled ELF sferics for each of these three ionospheres are shown in Figure 4.3b. For the two ionospheres that differ only in D region density, the impulse responses are quite similar in shape. However, for the two ionospheres that differ in E and F region

density, there is a significant difference in the post-peak oscillations.

It is important that these oscillations be modeled correctly in the impulse response to be used in the deconvolution, since the observed ELF sferics contain similar oscillations produced by the E and F regions. For example, if we attempt to deconvolve a source waveform out of an observed ELF sferic using a modeled impulse response that contains no post-peak oscillations, then the extracted source waveform will incorrectly contain oscillations that should have been present only in the impulse response. Similarly, the presence of the wrong oscillations in the impulse response will lead to the wrong oscillations in the current waveform. These post-peak oscillations are fairly small compared to the main peak, so any errors would probably not contribute significantly to the charge-moment measurement over larger time scales.

4.3.2 Choosing the Right ELF Impulse Response

Our objective is to use observed sferic waveforms to extract information about source current waveforms of lightning discharges which produce sprites. However, a typical storm produces many sferics, most of which are not associated with sprites. These non-sprite sferics can be used to infer the ionospheric conditions, as was done for the D region in Chapter 3. For the purposes of this chapter, both the D and the E and F regions must be inferred.

The D region can be directly inferred with relatively little ambiguity using the technique of Chapter 3. As mentioned above, the time period examined in this chapter is July 24, 1996, from 0400–0600 UT. Observations of VLF sferics between 0415 and 0430 UT (37 of them originating in the region 37.3° – 37.6° N, 99.5° – 99.9° W) and between 0545 and 0600 UT (50 of them originating in the region 37.0° – 37.5° N, 99.2° – 99.7° W) yield D region measurements for these time periods of $h'=83.5$ km, $\beta=0.51$ km $^{-1}$ and $h'=82.9$ km, $\beta=0.50$ km $^{-1}$, respectively. Figure 4.3 shows that a change of 2 km in h' does not significantly change the ELF impulse response, so that we can assume that the observed change in the D region has a negligible effect on the ELF impulse response. We use a D region profile of $h'=83.2$ km, $\beta=0.50$ km $^{-1}$ is used for the entire two hour observation period.

We now need to determine the appropriate E and F region electron density profiles to use in the propagation model. Because the return stroke in a “normal” lightning discharge starts and finishes within ~ 0.5 ms [Uman, 1987, p. 122], it can be considered an impulsive radiator at ELF (< 1.5 kHz). If we can find ELF sferics that appear as though they were radiated impulsively, they can be compared with theoretical ELF impulse responses in order to infer the ionospheric conditions. Figure 4.4a shows an impulsive sferic from a large, negative discharge in the sprite-producing region which occurred at 04:37:32.532 UT. This observed sferic contains the same post-peak oscillations as the modeled ELF impulse response in Figure 4.4a, which was calculated using the IRI E and F regions shown in Figure 4.4b. The good agreement in turn means that the theoretical impulse response is an accurate representation of the true impulse response.

Figure 4.5a shows an impulsive sferic received at Stanford later in the same time period, at 05:24:48.110 UT. The character of the impulse response has changed somewhat from that observed at 04:37:32.532 UT, implying that the E and F regions have changed. We can find a different IRI ionosphere (Figure 4.5b) that produces a modeled impulse response (Figure 4.5a) that contains the same post-peak oscillations as an observed ELF sferic. A comparison of Figure 4.4b and Figure 4.5b shows that during the ~ 1 hour period between these sferics, N_e at the E region maximum near 100 km altitude became more dense, while the minimum in the E region valley became less dense.

In the following sections, the 0437 UT theoretical ELF impulse response (Figure 4.4a) is used to extract the current-moment from sprite-producing sferics observed before 0500 UT, and the 0524 UT theoretical ELF impulse response (Figure 4.5a) is used for sferics observed after 0500 UT.

4.3.3 Filtering the ELF Impulse Response

For accurate reconstruction of the source current-moment waveform, the modeled ELF impulse response must be filtered in the same way as the observed sferics. As mentioned in Section 4.1, the observed ELF sferics are FIR low-pass filtered, and this

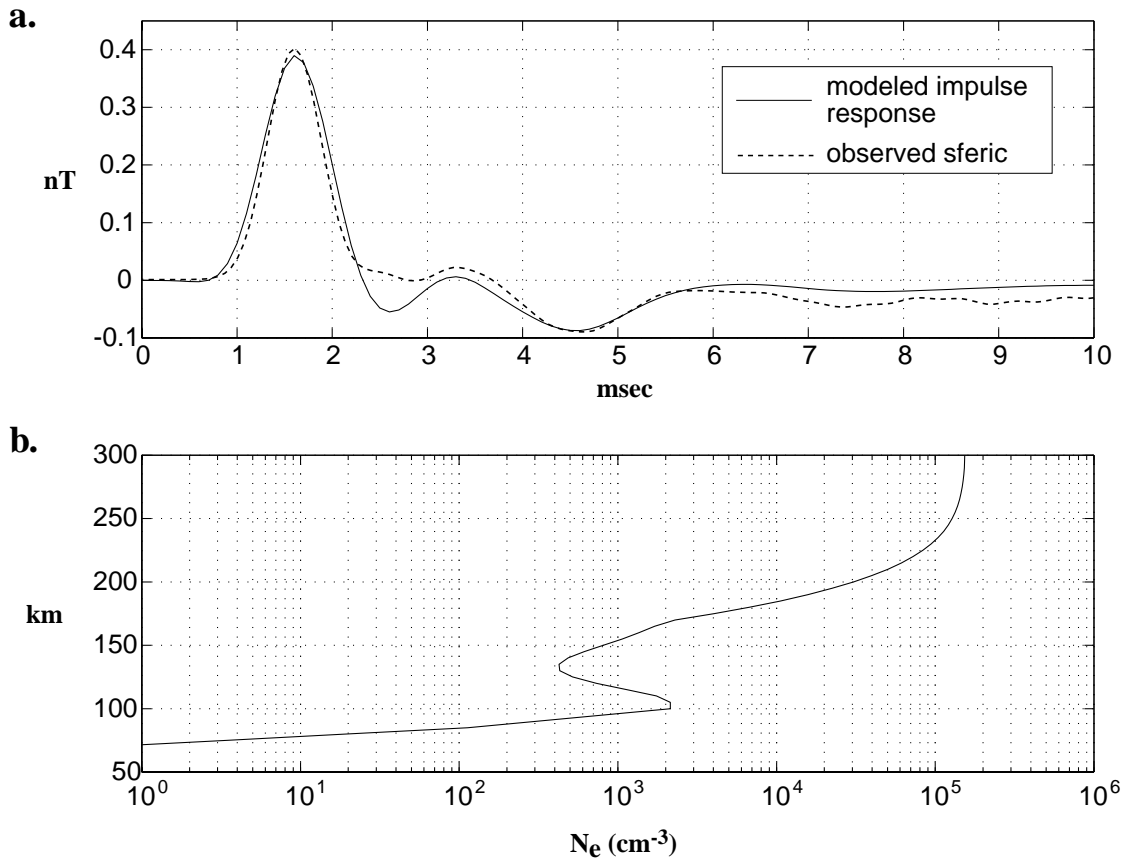


Figure 4.4: Determining the E and F region electron density profile. a: A modeled, impulsive ELF sferic that agrees well with the observed ELF sferic recorded at 04:37:32.532 UT. b: The IRI-based E and F region electron density profile used to produce the modeled ELF sferic.

same filter is applied to the modeled ELF impulse response. The characteristics of the high-pass filter in the observed data are difficult to measure because of the relatively slow system response in the frequency range of interest, and these characteristics are not known with certainty beyond the fact that the frequency response is flat to below 10 Hz. To reduce the effects of this uncertainty in the measurement system, a high-pass filter with a higher cutoff frequency than the filter in the system is applied to the observed ELF sferics and to the modeled ELF impulse response before the deconvolution process. This filtering, which ensures that the low end frequency response is

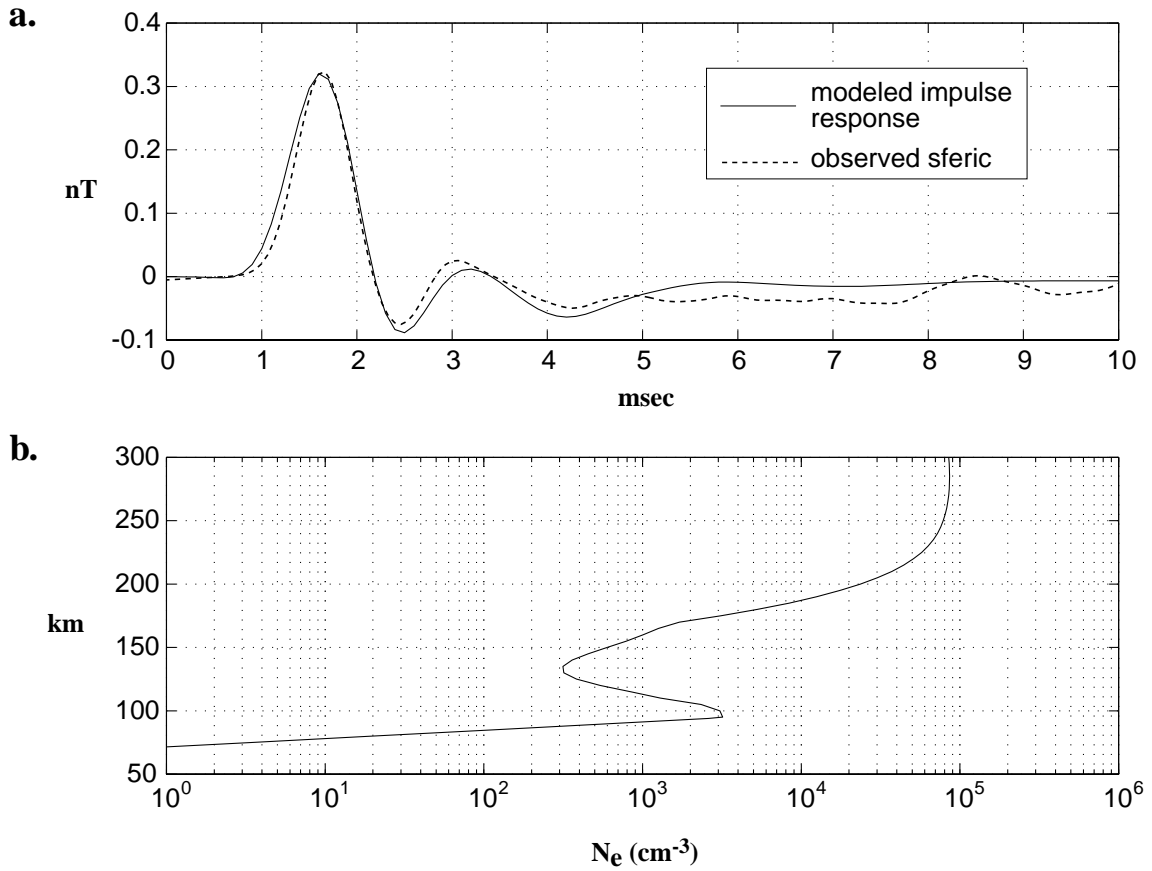


Figure 4.5: Determining the E and F region electron density profile. a: A modeled, impulsive ELF sferic that agrees well with the observed ELF sferic recorded at 05:24:48.110 UT. b: The IRI-based E and F region electron density profile used to produce the modeled ELF sferic.

accurately known, will remove some information on the slowest time scales, but it is necessary to ensure the accuracy of the deconvolution. The applied filter is a single pole, 10 Hz cutoff digital high-pass filter. The 10 Hz cutoff ensures that the information discarded will not affect the accuracy of the current-moment measurement over the time scales in which we are interested (~ 10 ms).

4.4 Deconvolution

4.4.1 Technique

With the impulse response for QTEM propagation from lightning source to receiver accurately modeled, a deconvolution procedure must be implemented to extract the source current-moment waveform from the measured ELF sferic and the modeled impulse response. Deconvolution is a mathematically tricky problem in general because it is ill-posed [*Press et al.*, 1986, p. 535]; that is, there are many solutions to this inverse problem that satisfy the forward convolution problem equally well. This quality is expected based on the nature of the forward problem, as convolution is inherently a smoothing or filtering operation, and it discards information. If an impulse is convolved with the impulse response of a low-pass filter, then there is no information at the output about the high frequencies at the input, and any attempt to reconstruct the input from the output must deal with this uncertainty.

Whatever method is used for the deconvolution, the extracted source current-moment waveform must be physically plausible, i.e. strictly positive (so the lightning current does not reverse direction, a phenomenon which is not seen in the published data) and smooth on submillisecond time scales [e.g. *Uman*, 1987, p. 199]. A deconvolution method which suits our purposes well is the CLEAN algorithm [*Teuber*, 1993, p. 216]. CLEAN was developed as a image-processing method for sharpening blurry images (since blurriness is caused by a two-dimensional convolution of the initial image with a spatial impulse response which is not sharp), but it can easily be adapted to the one-dimensional deconvolution problem we wish to solve here. CLEAN is somewhat similar to another deconvolution method called the method of successive substitutions [*Bracewell*, 1995, p. 454]. The CLEAN algorithm works best when the system impulse response has one dominant peak, as is the case in our application.

The CLEAN algorithm is an iterative procedure, and the steps of the process are outlined in Figure 4.6. The two panels in Figure 4.6a shows the ELF impulse response and the measured ELF sferic from which the current will be extracted. Notice that the oscillations in the impulse response are similar to those in the measured sferic, which is a consequence of the care taken to choose an ionosphere that produced an

impulse response similar to those observed.

The main step of the deconvolution process is to place an impulse in the reconstructed current waveform at the time and with the magnitude so that, when this current is convolved with the impulse response, the resulting waveform will have its peak at the same point in time and with the same magnitude as the observed output waveform. The current waveform in Figure 4.6b shows the proper placement of this impulse, and that the convolution of the impulse with the ELF impulse response gives a waveform with a peak in the proper location and of the right magnitude.

The difference between the reconstructed output and the measured output is calculated and referred to as the *residual*, also shown in Figure 4.6b. Since convolution is a linear operation, the problem that remains is to find the current that, when convolved with the impulse response, gives the residual. Finding this current is simply another deconvolution operation, so that in this way the solution can be found recursively by repeatedly applying the above procedure of adding an impulse to the reconstructed current as to match the peak in the residual. Figure 4.6c shows the addition of another current impulse to match the residual peak, and the convolution of this two impulse current with the impulse response leads to a reconstructed output which is closer to the measured output than that for the single impulse current.

The residual after two iterations is also shown in Figure 4.6c, which is smaller in magnitude than the residual after one step. After each successive approximation, the residual has a smaller maximum than the previous one, which implies that the impulses added to the reconstructed current waveform decrease in amplitude as the iteration continues. After a certain number of iterations, the changes being made to the current waveform do not contribute significantly to the total current, and the iteration can be stopped. Because the maximum value of the residual must be small at this point, the reconstructed output must closely agree with the measured output, and a solution to the deconvolution problem has been obtained.

In the numerical implementation of this algorithm, the continuous convolution required at each time step is executed as a discrete convolution of two sampled vectors. For maximum accuracy, these vectors should be sampled as finely as possible so that

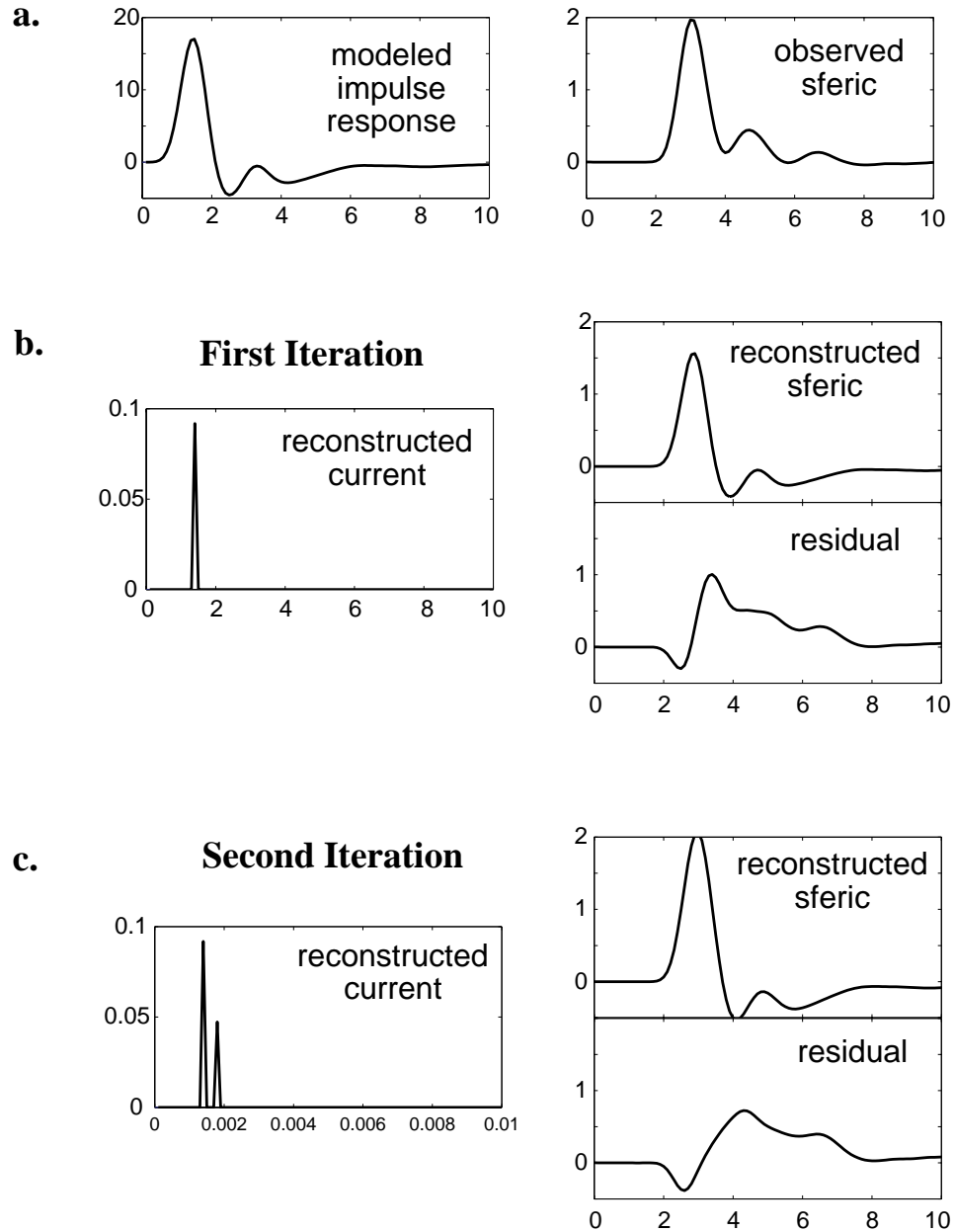


Figure 4.6: Outline of the CLEAN algorithm. a: The modeled ELF impulse response and the observed ELF sferic. b: The current waveform, reconstructed sferic, and residual after the first iteration. c: The current waveform, reconstructed sferic, and residual after the second iteration.

the discrete convolution is a good approximation of the continuous convolution. However, since the computational cost of this algorithm is dominated by the forward convolution required in each iteration, a time step that is too small drastically increases the execution time. One way to increase the computation speed while maintaining reasonable accuracy is to run the method with a coarse time step until the solution is close to convergence, interpolate all of the vectors (current, impulse response, and measured sferic) to a finer time step, and then run the method with the fine time step until the maximum value of the residual is below some threshold level.

With this deconvolution algorithm, it is easy to limit the reconstructed input to be strictly positive, which meets part of the constraint on physical plausibility of the source-current waveform. However, if the above procedure is applied without any modifications, then the reconstructed current is composed solely of impulses, which does not meet the smoothness requirement. To improve the smoothness of the solution, the CLEAN algorithm is slightly modified. First, the amplitude of the current impulse placed at each iteration is only one-tenth of the value required to reduce the residual maximum to zero. This means that more iterations are required to build the current up to its proper value, but these impulses are distributed in time rather than placed at a single point, contributing to the smoothness of the solution. The reconstructed current waveform is also low-pass filtered after a prescribed number of iterations (from 20 to 50) to periodically smooth the solution further. And lastly, rather than place the current impulses at the exact time to maximally decrease the residual, they are placed at the time with minimum current over a 0.5 ms window around the optimal placement point. This ensures that if an impulse is adjacent to a time with no current, impulses are added to the zero-current time first. This window is narrow enough that the movement of the impulse does not degrade the quality of the solution, but it contributes further to its smoothness.

There are a number of parameters involved in these various smoothing schemes, but the one that requires the most variation between the different sferics is the one which controls whether or not smoothing is applied to the initial portion of the extracted current-moment waveform. Some sferics have a relatively slow rise time and require smoothing of this initial portion to keep it smooth. However, some have rapid rise

times, and any smoothing of the initial portion widens the initial pulse of the reconstructed sferic beyond the width of the observed sferic, thereby not properly solving the deconvolution. If the rise time of the observed sferic is less than 1 ms, then no smoothing is applied to the first 2 ms of the reconstructed current-moment waveform.

4.4.2 Deconvolution Tests

In order to fully understand the nature of the information extracted using the deconvolution algorithm described above, we now test it to see if a known current-moment waveform can be successfully extracted from a modeled sferic.

Slow Currents

Figure 4.7a shows the modeled ELF impulse response (from Figure 4.5a) that is used in the following 3 examples. This impulse response was convolved with a simulated current waveform (which had no significant high frequency content beyond that in the impulse response) to produce a simulated sferic, shown in Figure 4.7b. The deconvolution algorithm is then applied using this sferic and impulse response to obtain an extracted current waveform, which should be identical to the known simulated source waveform. These two current waveforms are shown in Figure 4.7c, and they agree well, indicating that the deconvolution method works as expected.

Fast Currents

If the source current contains components faster than the impulse response, then these components cannot be fully recovered, but they do not significantly degrade the deconvolution. Using the impulse response from the previous example, Figure 4.8a shows the simulated sferic, and Figure 4.8b shows the simulated source and the extracted source. The slow current hump is restored accurately, but the two faster peaks are both lower and wider than they were in the original source waveform. This result is a consequence of the fact that the simulated source contained fast frequency components that were filtered out by the ELF impulse response. Nevertheless, the

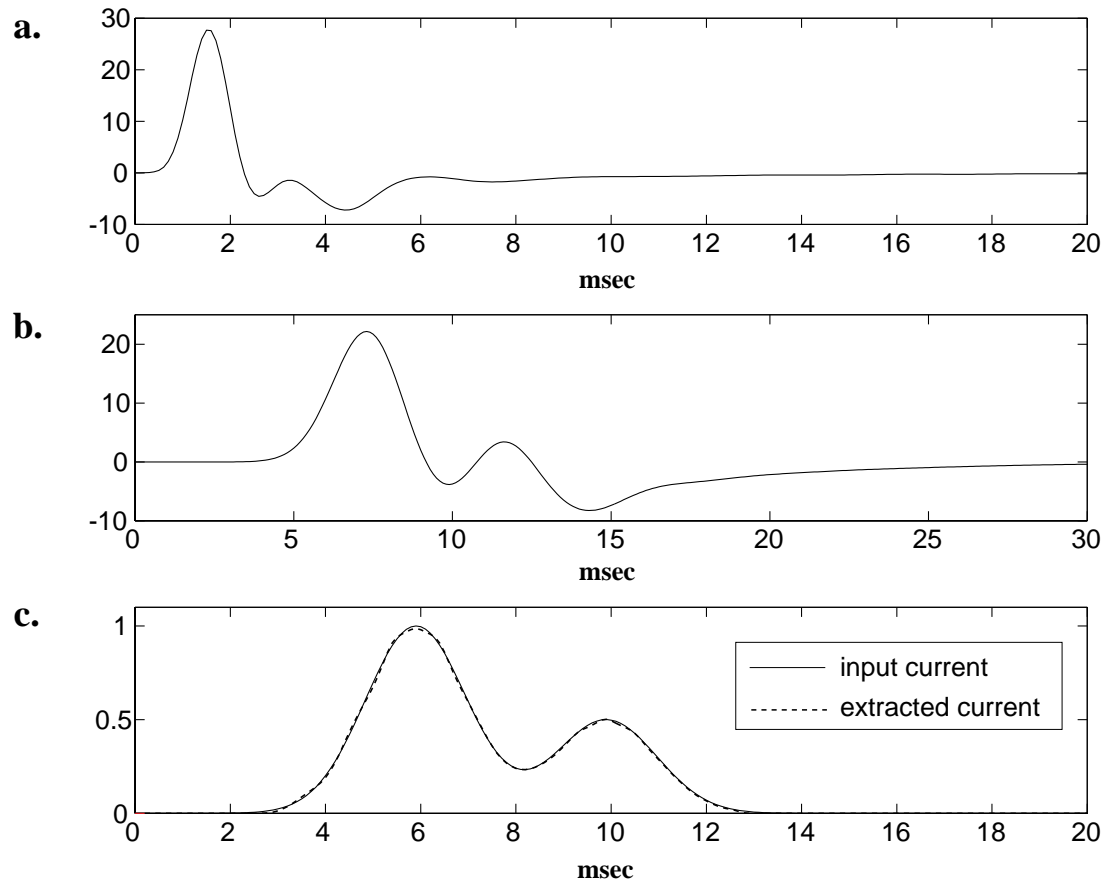


Figure 4.7: Testing the CLEAN-based deconvolution with a known slow source current. a: The modeled ELF impulse response. b: The simulated spheric c: The nearly identical simulated source and extracted source.

deconvolution algorithm has accurately reconstructed the slower variations of the source based on the information available from the spheric.

It is important to note that the elimination of these fast components does not affect the measurement of the total charge transferred, which is our ultimate objective. Let $i(t)$ be the simulated source, and let $i_{ex}(t)$ be the extracted source which is the equivalent of a low-pass filtered version of $i(t)$. The total charge moved in the simulated source is $q = \int_{-\infty}^{\infty} i(t)dt$, which is equal to the Fourier transform of $i(t)$ evaluated at $f = 0$. If $i(t)$ is low-pass filtered, then the Fourier transform of $i(t)$ does change, but not at $f = 0$. Therefore the Fourier transform of $i_{ex}(t)$ has the same

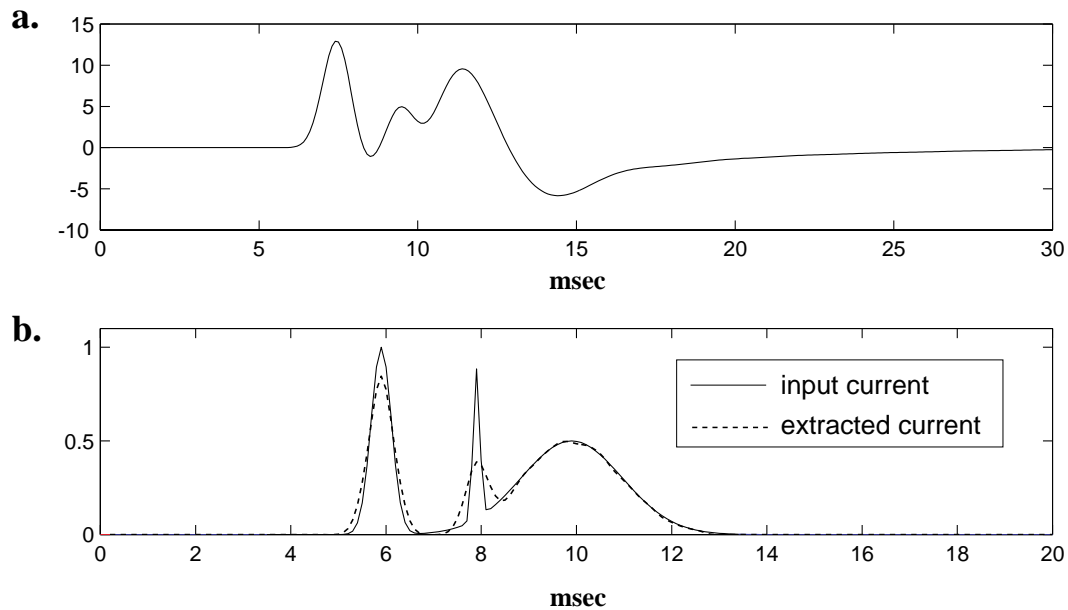


Figure 4.8: Testing the CLEAN-based deconvolution with a known fast source current. a: The simulated sferic b: The simulated and extracted source current waveforms, which are not identical but do move the same total charge.

magnitude at $f = 0$ as the Fourier transform of $i(t)$, and the two waveforms have the same total charge transfer. In short, the low-pass filtering slows the perceived rate of charge transfer but does not change the total area under the curve, which is the total charge transferred for the duration of the current. This is confirmed numerically by comparing the integrals of the two curves in Figure 4.7b, which agree to better than 0.5%. As mentioned in Section 4.1, this discarded fast time-scale information is probably not important in the production of sprites, as they are usually observed at least 1 ms after the onset of the discharge.

Nearly-Constant Currents

Just as there is an upper limit on frequency components that can be measured, there must be a lower limit as well because of the high-pass filtering of the sferic waveforms. Figure 4.9a shows a sferic produced with a current that is nearly constant over a 50 ms time scale, and Figure 4.9b shows this simulated current and the current waveform

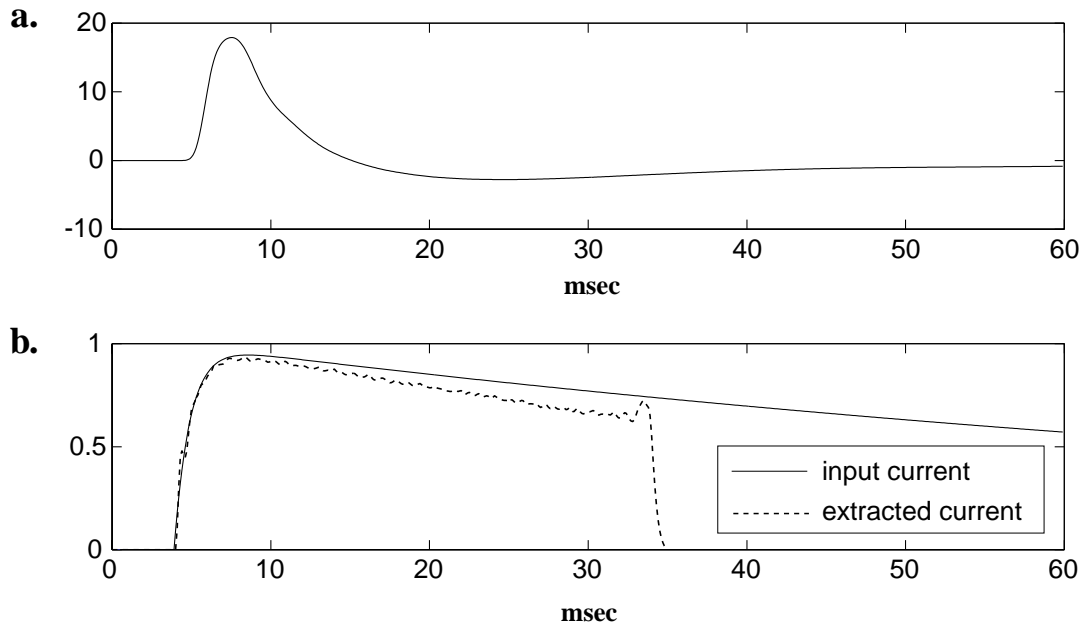


Figure 4.9: Testing the CLEAN-based deconvolution with a known nearly-constant source current. a: The simulated sferic b: The simulated and extracted source current waveforms, which, due to the slow source components, are not identical and do not move the same total charge.

extracted by the deconvolution algorithm from the simulated sferic. The extracted current turns off abruptly because the deconvolution algorithm only attempts to extract the current over a finite time window (~ 30 ms in this case).

The agreement is good over the first 15 ms of the two current waveforms. The latter portion of the extracted current after 25 ms is $\sim 15\%$ too low, which is an effect of the high-pass filtering on the sferic. The source current contains frequency components so slow that the system (controlled by the high-pass filtering) cannot respond and they are attenuated in the sferic, and thus cannot be completely restored in the extracted current. Unlike the low-pass filtering which does not affect total charge transfer, the high-pass filtering lowers the total charge measured. However, the error in the total charge transfer over the first 20 ms of the reconstruction is $\sim 5\%$, and is thus only slightly affected by the high-pass filtering. This $\sim 5\%$ error is the maximum reconstruction error over 20 ms without accounting for noise in the measurement.

Over a period shorter than 20 ms, this maximum error is proportionally lower.

Limits on Current Measurability

The last example above shows that approximately constant currents can be extracted fairly accurately at least 20 ms after the current onset, given the system bandwidth as imposed by the high pass filtering described in Section 4.3.3. However, since the system response does not extend to 0 Hz, there must be some time limit beyond which constant currents cannot be measured. The best way to investigate this is to examine the system *step* response, i.e. the output sferic produced by an instantaneous turn-on of a constant current.

The step response $u(t)$ of the system can be found from the impulse response $h(t)$ simply by $u(t) = \int_0^t h(\tau) d\tau$ [Bracewell, 1986, p. 181]. Figure 4.10 shows the theoretical response to a current-moment step with amplitude 10 kA·km, which is a value higher than most reported amplitudes of continuing current [Uman, 1987, p. 171] but is a reasonable value for the long-lasting currents observed in sprite-producing discharges, as measurements below will show. The figure shows that even in a noiseless system, the system stops responding to this constant current after ~ 70 ms, which establishes a theoretical upper limit to the duration of current measurable with the given system bandwidth.

In the presence of noise, however, the system performance is expected to be worse. Over long time periods (>20 ms), the noise level in the Stanford ELF observations is ~ 0.02 nT, primarily due to the non-stationary nature of the power line hum at 60 Hz. Looking at Figure 4.10, this level is reached in ~ 40 ms for a 100 kA·km current-moment, and beyond this time, the signal-to-noise ratio would be less than 0 dB and any measurement would be very inaccurate. Larger constant current-moments can be extracted accurately for a correspondingly longer time because of the higher output signal level, and smaller currents can be measured only for a shorter time. Subsequent sferics also contribute to the overall noise level and prohibit accurate single discharge current measurements over long time periods. The current-moment waveforms in the following sections will be extracted over a 10–20 ms period, which is short enough that neither the noise from successive sferics nor the fundamental limits discussed above

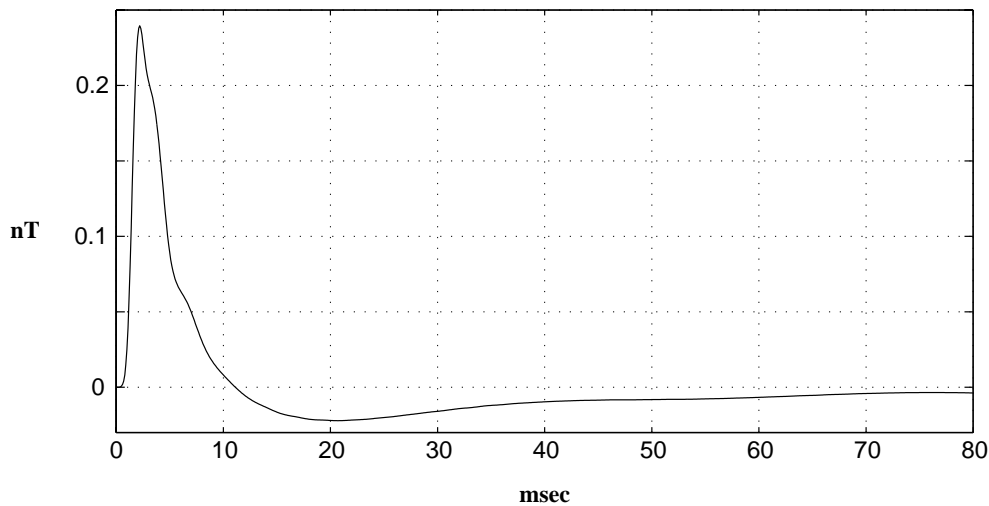


Figure 4.10: The theoretical step response of the ELF propagation system, including the high-pass filter described in Section 4.3.3.

should contribute any errors beyond the maximum $\sim 5\%$ error discussed in Section 4.4.2.

Summary

The CLEAN algorithm is effective in reconstructing the source current-moment waveform from an observed sferic within the limitations of the system frequency response as determined by the low- and high-pass filtering. The higher frequencies are effectively filtered out of the extracted source waveform, leading to a extracted source waveform that can be smoother than the actual source waveform. However, the measured total charge is not affected by this low-pass filtering.

The low frequencies removed by the high-pass filtering could have an effect on the charge-moment measurement. For nearly constant source currents lasting ~ 30 ms, it was shown that the loss of these lowest frequencies leads to an extracted source current-moment and charge-moment slightly lower than in the actual source. Because the CLEAN algorithm reconstructs the source by adding current only where it is required, we are assured that these slow currents are never overestimated. For time scales < 20 ms, the lower frequency cutoff in the sferic measurements is low enough that the source current-moment can be extracted to an accuracy of $\sim 5\%$. For

time scales >20 ms, the extracted current-moment and charge-moments should be viewed as a lower bound on these quantities, as longer-lasting currents which continue to remove charge will not produce a measurable response given the measurement bandwidth.

4.5 Current-Moment Waveforms Extracted from Sprite-Producing Sferics

The magnitude of vertical charge-moment change in sprite-producing discharges can now be extracted. First, three individual sprite-producing discharges are examined in detail, and then measurements are made from 15 different sprite-producing discharges which occurred during the July 24, 1996, 0400–0600 UT period of interest.

4.5.1 Sprite-Producing Discharge at 04:09:19.536 UT

Arguably the most spectacular sprite of the 1996 sprites observational campaign occurred in response to a positive discharge recorded by the NLDN at 04:09:19.536 UT, at 37.62°N 102.00°W , and with a peak current of $+158.0$ kA. An image-intensified video image of the sprite is shown in Figure 4.11a. The distance from the lightning location to the video camera is 422 km, and from the known angular field of view of the camera, the sprite is ~ 55 km wide. To calculate the absolute altitude of the sprite, we assume that the sprite is directly over the lightning discharge, and that it is roughly cylindrical in shape, so that the perceived top is closer to the video camera, and the perceived bottom is farther from the camera. Geometrical calculations show that the sprite extended vertically from 39 to 88 km altitude. The time stamp on the video frame corresponds to 33.3 ms after the start of the 50 ms integration time of the entire image, thus the integration time extends 16.7 ms after the marked time. The integration intervals of consecutive images overlap by 16.7 ms.

Figure 4.11b shows the ELF sferic launched by the associated cloud-to-ground discharge and received at Stanford. After applying the deconvolution technique with the appropriate modeled impulse response, the reconstructed sferic (also shown in Figure

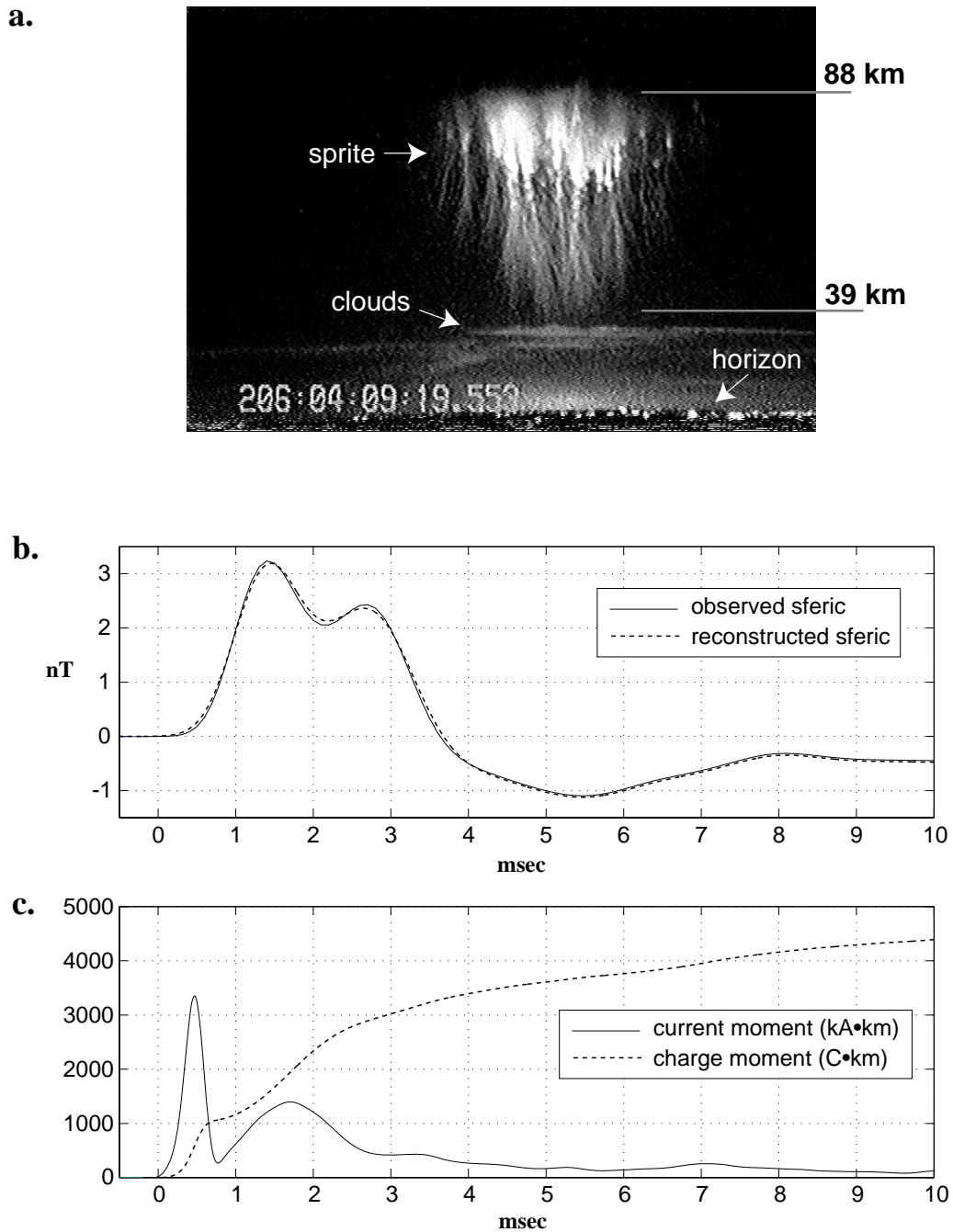


Figure 4.11: Observed sprite and sferic on July 24, 1996, at 04:09:19.536 UT. a: A video image of the sprite. b: The observed and reconstructed ELF sferics. c: The source current-moment and cumulative charge-moment waveforms.

4.11b) is obtained. The agreement between the two is good (let s_o be the observed sferic, s_r be the reconstructed sferic, and $\|\cdot\|_2$ be the L_2 norm [Golub and Van Loan, 1989, p. 53] then $\frac{\|s_o - s_r\|_2}{\|s_o\|_2} = 0.044$), implying that the deconvolution problem has been successfully solved.

Figure 4.11c shows the source current-moment waveform (in units of kA·km) extracted from the observed sferic, with a measured peak current-moment of ~ 3400 kA·km. Also in Figure 4.11c is a plot of the cumulative charge-moment transfer of the discharge, defined as $M_q(t) = \int_0^t I(\tau) d\tau$, which represents the charge-moment change in the discharge from the onset to the time in question. After 10 ms, ~ 4300 C·km were transferred. The magnitude of this discharge easily meets the theoretical threshold required to create a visible sprite at the upper altitudes under the previously discussed QE mechanism [Pasko et al., 1997], and is also sufficient to create emissions through the runaway electron models [Taranenko and Roussel-Dupre, 1996; Roussel-Dupre and Gurevich, 1996; Lehtinen et al., 1997].

The distinct emissions at altitudes near 40 km require $\sim 10^4$ C·km of charge-moment change according to the QE model [Pasko et al., 1997]. After 10 ms, the discharge current-moment appears to approach a nearly constant value of ~ 100 kA·km. If a current of this amplitude were to persist at this level for the duration of the image integration time (an additional 23 ms), an additional 2300 C·km would be moved in this time. This estimated total charge-moment change of 6600 C·km is still slightly lower than is necessary to produce the lowest-altitude optical emissions observed in this sprite, but the assumed continuing current-moment amplitude could easily have been larger by a factor of 2, thereby moving the theoretically expected amount of charge according to the QE model.

4.5.2 Sprite-Producing Discharge at 05:31:30.109 UT

Another relatively large sprite occurred in response to a positive discharge recorded by the NLDN at 05:31:30.109 UT, at 37.71°N 100.69°W , with a peak current of +80.6 kA. The first video frame which showed the sprite is shown in Figure 4.12, with a measured altitude extent from 57 to 91 km altitude. This sprite is especially interesting because

the acquisition of this video frame only lasted ~ 6 ms beyond the NLDN-recorded discharge time. Accounting for the ~ 1.5 ms speed-of-light propagation time for the sprite optical emissions to travel to the video camera, this image shows the extent and brightness of the sprite in response only to the first ~ 4.5 ms of the discharge.

Figure 4.12b shows the observed and reconstructed ELF sferics radiated by this discharge. The agreement between the two is good ($\frac{\|s_o - s_r\|_2}{\|s_o\|_2} = 0.052$). Figure 4.12c shows the reconstructed source current-moment and cumulative charge-moment transfer waveforms. The critical value in this case is the total charge-moment change ~ 4.5 ms after the discharge because only this charge transfer contributed to the optical emissions seen in the video image. This value is seen to be ~ 2000 C·km. Interpreted in the context of the QE model [Pasko *et al.*, 1997], ~ 2000 C·km is enough charge-moment transfer to create optical emissions to altitudes as low as ~ 70 km altitude, but roughly 4000 C·km are required to create the observed optical emissions at ~ 60 km altitude. The fact that the optical emissions are observed at lower altitudes indicates that factors not considered in the QE model may play a role in sprite creation. A charge-moment transfer of this magnitude is enough to create optical emissions at the observed low altitudes by the runaway processes described by Taranenko and Roussel-Dupre [1996] and Roussel-Dupre and Gurevich [1996]. It is worthy of mention is that the subsequent video image (integrated from 05:31:30.098–.148) shows a generally brighter sprite that extends to even lower altitudes (~ 50 km), demonstrating a clear downward propagation of the lowest altitude emissions.

4.5.3 Sprite-Producing Discharge at 05:25:17.063 UT

Figure 4.13a shows an image of a sprite associated with a +73.3 kA discharge at 05:25:17.063 UT and 37.03°N 101.92°W . This sprite is composed of a number of “carrot”-like elements extending from ~ 56 to 91 km. The ELF sferic radiated from this discharge is shown in Figure 4.13b. A noticeable feature is the apparent second peak at ~ 7.5 ms after the initial sferic onset, which will be discussed in Section 4.5.4. The reconstructed and observed sferics agree well ($\frac{\|s_o - s_r\|_2}{\|s_o\|_2} = 0.059$), and the extracted current- and charge-moment waveforms are shown in Figure 4.13c. Because

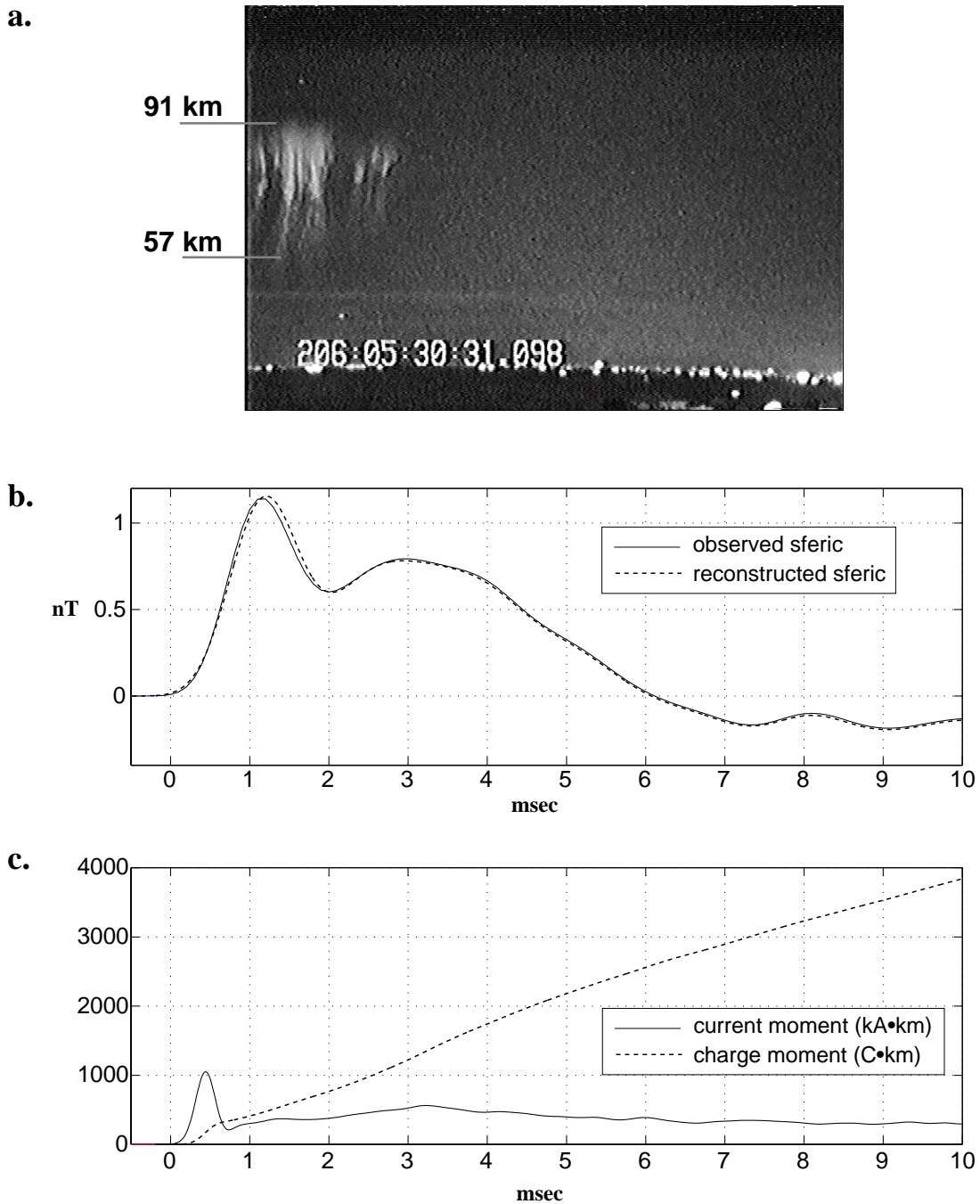


Figure 4.12: Observed sprite and sferic on July 24, 1996, at 05:31:30.109 UT. a: A video image of the sprite. b: The observed and reconstructed ELF sferics. c: The source current-moment and cumulative charge-moment waveforms.

the video integration time extended ~ 16 ms after the NLDN recorded discharge time, the current- and charge-moment waveforms are extracted for 20 ms.

This discharge produced a change of ~ 1600 C·km in the first 16 ms of the discharge, which according to the NLDN discharge time is the duration of the current that contributed to the video image. As in the previous case, this value is somewhat lower than necessary to account for the observed emissions at the lowest altitudes as predicted by the QE model [*Pasko et al.*, 1997], which requires ~ 4000 C·km of charge-moment change to produce emissions at 60 km. However, this discharge is also smaller than the magnitude required for sprite production by the runaway electron models [*Taranenko and Roussel-Dupre*, 1996; *Roussel-Dupre and Gurevich*, 1996; *Lehtinen et al.*, 1997]. This suggests that factors not considered in the QE and runaway electron models may contribute to the total sprite optical emissions, especially at the lower altitudes near 60 km.

4.5.4 Charge-Moment Change in 15 Sprite-Producing Discharges

Table 4.1 lists the NLDN-recorded parameters for 15 lightning strokes associated with sprites seen in the Yucca Ridge video observations between 0400 and 0600 UT on July 24, 1996, including the three sprites analyzed in detail above.

Figure 4.14 shows the cumulative vertical charge-moment transfer waveforms for the first 10 ms of the discharges for these 15 sprite-producing discharges. The majority of the discharges show remarkable similarity in their characteristics, moving from 400 to 700 C·km in the first 10 ms of the discharge. The charge-moment magnitude in these smaller sprite-producing discharges is significantly lower than that required to produce visible optical emissions with the runaway electron models [*Bell et al.*, 1995b; *Taranenko and Roussel-Dupre*, 1996; *Roussel-Dupre and Gurevich*, 1996; *Lehtinen et al.*, 1997]. In *Pasko et al.* [1997], the charge-moment movement necessary to create optical emissions at different altitudes through the QE model is explicitly calculated. This implies that the QE model can only be evaluated on the basis of simultaneous charge-moment measurements and high temporal and spatial resolution

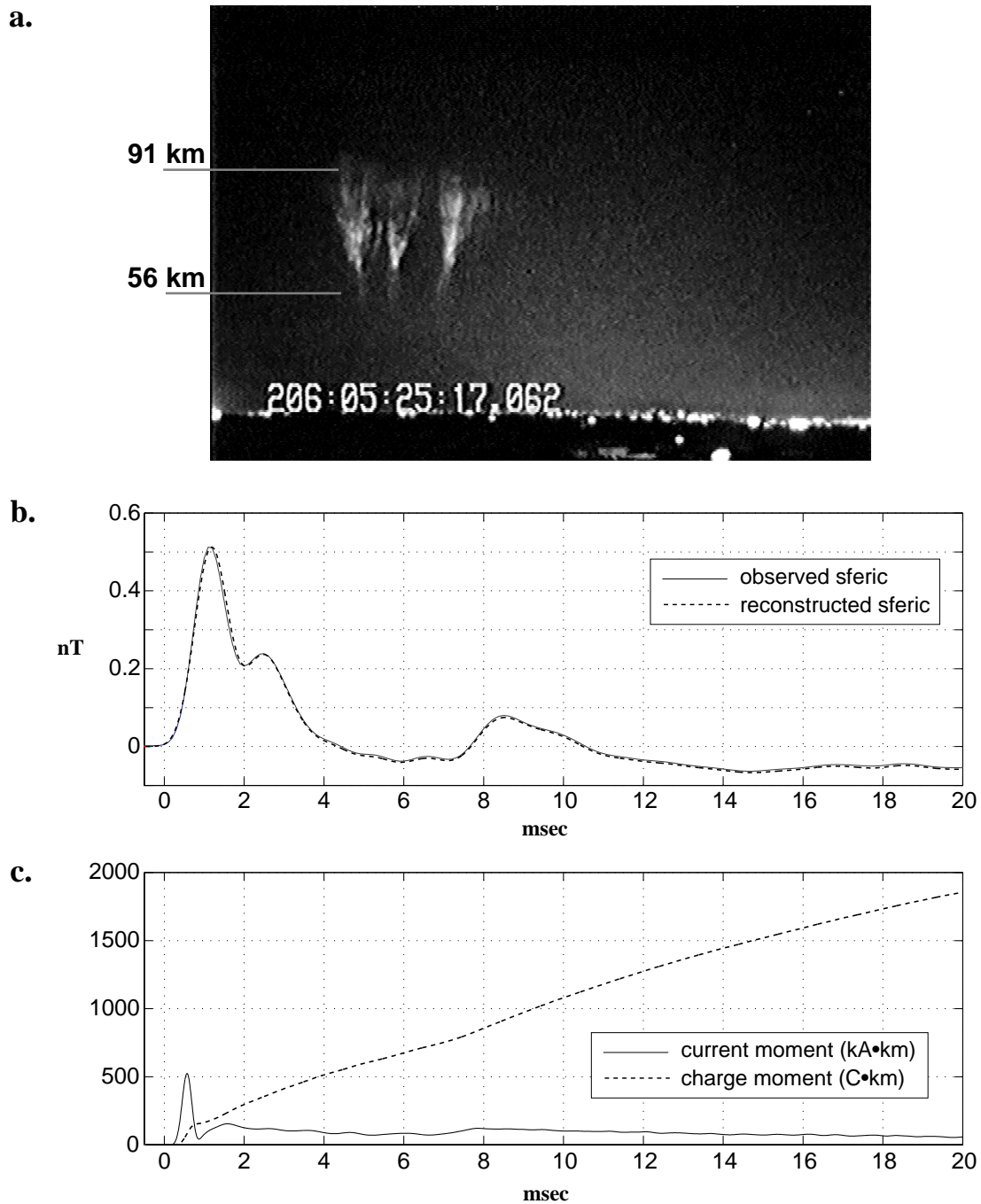


Figure 4.13: Observed sprite and sferic on July 24, 1996, at 05:25:17.063 UT. a: A video image of the sprite. b: The observed and reconstructed ELF sferics. c: The source current-moment and cumulative charge-moment waveforms.

Sprite Video Time	NLDN Time (UT)	Location	Peak Current (kA)
04:09:19.553	04:09:19.536	37.62°N 102.00°W	+158.0
04:24:47.619	04:24:47.596	37.67°N 102.02°W	+86.6
04:30:45.632	04:30:45.620	37.20°N 101.47°W	+107.8
05:05:32.185	05:05:32.175	37.47°N 101.29°W	+47.3
05:12:20.345	05:12:20.334	37.49°N 101.25°W	+154.2
05:25:17.062	05:25:17.063	37.03°N 100.92°W	+73.3
05:30:31.098	05:30:31.109	37.71°N 100.69°W	+80.6
05:32:12.796	05:32:12.784	37.04°N 101.13°W	+43.1
05:38:00.599	05:38:00.587	36.65°N 100.98°W	+26.5
05:38:00.999	05:38:01.005	37.46°N 100.86°W	+46.6
05:42:38.433	05:42:38.426	37.07°N 101.05°W	+58.2
05:46:15.676	05:46:15.666	36.48°N 101.00°W	+44.0
05:47:55.272	05:47:55.248	37.53°N 100.54°W	+28.5
05:50:24.015	05:50:23.994	36.60°N 101.23°W	+117.7
05:53:30.962	05:53:30.951	36.58°N 100.82°W	+48.3

Table 4.1: Video time and NLDN-recorded characteristics of 15 sprite-producing discharges.

optical observations in order to pinpoint the exact onset times of optical emissions at different altitudes of the sprite, which cannot be done based solely on the data presented in Figure 4.14. However, the latter two cases examined above do show that observed vertical charge-moment changes are somewhat smaller (by approximately a factor of 2) than is necessary to create the observed optical emissions with the QE model [Pasko *et al.*, 1997].

A notable feature in many of the charge-moment transfer curves in Figure 4.14 is a “kink” some 1–10 ms after the discharge onset, after which the charge-transfer rate increases somewhat abruptly. Remembering that the source current-moment waveform is the derivative of these charge-moment curves, these kinks indicate a sudden (~ 1 ms) increase in the source current-moment at least 1 ms *after* the lightning discharge. Figures 4.11c and 4.13c clearly show this second peak in the source current-moment, which corresponds to a second peak in the observed ELF sferics. Figure 4.12c also shows a peak, though it is significantly broader and less distinct than in the other two cases.

Using data from a different day (July 22, 1996), a careful time alignment of the

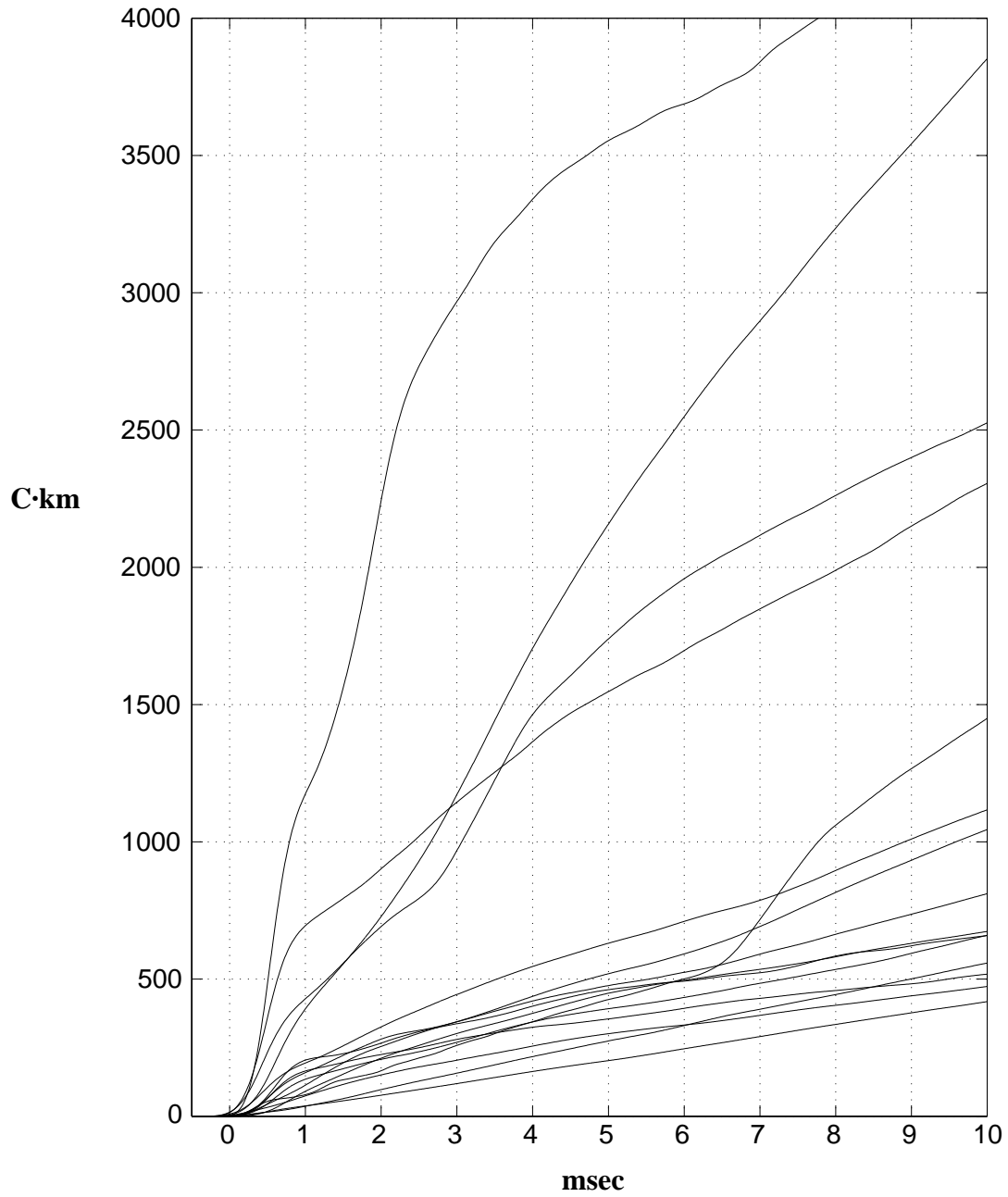


Figure 4.14: Extracted cumulative charge-moment change over 10 ms in 15 sprite producing discharges.

extracted source current-moment and high resolution optical measurements of large scale sprite brightness has shown that the rise, peak, and fall of this second current-moment peak is simultaneous with the same features of the sprite brightness [Cummer *et al.*, 1997]. This temporal alignment strongly suggests that currents in the sprite itself, which are roughly proportional to the sprite brightness, are radiating the observed ELF peak and are measured by this method.

The theoretical results of Pasko *et al.* [1997] show that these ELF-radiating sprite currents are not unexpected, and the expected magnitude of these currents is consistent with the magnitude estimated from the ELF sferic [Cummer *et al.*, 1997]. Thus some of the extracted charge-moment changes shown in Figure 4.14 may in fact be due to currents in the sprite. This would have the effect of reducing the lightning charge-moment change responsible for the creation of the sprites, which reinforces the conclusion of this work that observed charge-moments are often somewhat lower than would be expected on the basis of existing theories.

Chapter 5

Summary and Suggestions for Future Work

5.1 Summary

We have compared measurements of the characteristics of VLF and ELF radio atmospheric spherics with theoretical propagation predictions to infer two quantities: the nighttime D region electron density profile along the spheric propagation path in the Earth-ionosphere waveguide, and the vertical source current-moment in sprite-producing lightning discharges.

A general theoretical formulation for the propagation of single frequency VLF and ELF signals in the Earth-ionosphere waveguide developed by *Budden* [1962] and implemented in a computer code [*Pappert and Ferguson*, 1986, and references therein] was adapted to solve the problem of the propagation of transient VLF and ELF signals. The broadband, frequency-domain solution from this propagation model was converted to a time-domain waveform via the numerical inverse Fourier transform method described in Appendix A.

In an effort to understand the range of D region ionospheric parameters that can be inferred using observed VLF spherics, the effects of various ionospheric conditions and parameters on the characteristics of VLF (>1.5 kHz) spherics were theoretically investigated. Because the spheric spectrum was found to be a better indicator of these

parameters than the sferic waveform, all comparisons of theory and observation were made in the frequency domain. By assuming a two-parameter (height and sharpness) exponentially-increasing electron density profile, the sferic spectrum was shown to be strongly dependent on the height parameter but somewhat less so on the sharpness parameter for nighttime ionospheres. For a daytime ionosphere, the sferic spectrum was found to be much less dependent on these parameters.

The collision frequency profile and the ion density profile were found to have a substantially smaller effect on sferic characteristics than the electron density profile, indicating that the electron density profile could be inferred using measured VLF sferics. A comparison of propagation under homogeneous and inhomogeneous ionospheres showed that the observed sferic spectrum is primarily sensitive to the path-averaged electron density profile and that even strong inhomogeneities have little effect on our ability to infer this quantity from data. However, the uncertainty in the ion and collision frequency profiles and in the homogeneity of the ionosphere does limit the accuracy with which we can assess the sharpness of the electron density profile.

Observed sferics originating in lightning discharges occurring in a small geographic region (as documented by the National Lightning Detection Network) were temporally averaged to reinforce the propagation effects to be measured and reduce the effects of source variability and noise. The sferic time window was 30 minutes, long enough to provide enough sferics for effective averaging, but short enough that the temporal variation of the ionosphere was likely insignificant. Low-pass filtering over the late-time portion of the sferic waveforms was also used to improve the signal to noise ratio above 10 kHz in the measured average spectrum. The sferic propagation model was evaluated for a large number of different ionospheres, and the ionosphere which produced the best agreement (based on a quantitative criterion discussed in Section 3.3.3) between the theoretical and observed sferic spectra was deemed to be the inferred exponential ionosphere. The quality of agreement between the best-fit theoretical and observed spectra was measurably perturbed by a change in the ionospheric height parameter by as little as 0.2 km, demonstrating the precision of the measurement. Quantitative evaluation of the accuracy of this measurement will have to wait for the development of an independent technique for measuring large-scale D

region electron densities. It should be emphasized that this technique infers electron density profiles relative to the average ground altitude of a particular propagation path.

The *D* region measurement technique developed here was applied to two other cases. Simultaneous nighttime measurements using sferics from five different lightning locations (all received at Stanford) showed an ionospheric height change of 3 km from north to south across much of the United States. Also, sferics along a single propagation path were studied over an extended time period near sunset, when the ionosphere is known to be changing with time. This measurement showed the expected result that both the ionospheric height and sharpness increased with time. However, it is difficult to measure daytime ionospheres with this technique because of the lack of spectral features upon which the measurement depends.

Since the sferic waveform observed at a given site depends on the source current-moment waveform as well as the ionospherically-controlled propagation, the former quantity can be inferred for individual discharges from observed sferics. Of particular interest are those lightning discharges associated with sprites. Earlier work has shown that sprite-producing discharges radiate unusually strongly in the ELF band (<1.5 kHz) [Boccippio *et al.*, 1995; Reising *et al.*, 1997] and therefore contain large amplitude, slowly-varying current components. These large and slow currents can transfer a great deal of charge from the cloud to the ground, a fact which is in general agreement with current theories of sprite production [Pasko *et al.*, 1997; Bell *et al.*, 1995b; Roussel-Dupre and Gurevich, 1996; Taranenko and Roussel-Dupre, 1996; Lehtinen *et al.*, 1997] in which sprites are created by large quasi-static electric fields created by large vertical charge-moment changes.

The magnitude of the vertical charge-moment change was extracted quantitatively from observations of ELF (<1.5 kHz) sferics launched by sprite-producing lightning discharges. By focusing exclusively on the <1.5 kHz components, the propagation modeling was made simpler because only a single waveguide mode (the QTEM mode) needed to be considered. The discarded higher frequency sferic components provide information on the faster time scales (<0.5 ms) of the discharge current, which are relatively unimportant because of the well-documented >1 ms time delays between

the onset of the discharge to the appearance of the sprite [Rairden and Mende, 1995; Fukunishi et al., 1996; Winckler et al., 1996; Inan et al., 1997]. The total magnitude of the vertical charge-moment change in any fast component is measured accurately by this technique, but it is inferred to occur over a longer (>0.5 ms) period because of the filtering of the ELF sferic waveform.

Source current-moment waveforms were extracted from observed ELF sferics and a modeled ELF propagation impulse response by a robust deconvolution method [Teuber, 1993, p. 216] described and analyzed in detail in Section 4.4. This technique was applied to extract the source current-moment waveforms over the first 10 ms of the discharge (one was extracted for 20 ms) from 15 different sprite-producing sferics measured on July 24, 1996. Of the 15 discharges examined, 9 did not produce vertical charge-moment changes in 10 ms large enough to excite the runaway electron process to the levels required to create the observed optical emissions. The QE model can only be evaluated on the basis of simultaneous charge-moment measurements and high temporal and spatial resolution optical observations in order to pinpoint the exact onset times of optical emissions at different altitudes of the sprite, since the charge-moment change necessary to create optical emissions depends on the altitude in question. This was done for three different sprites, two of which clearly showed optical emissions at lower altitudes than predicted by the QE model for the measured vertical charge-moment change. One of these two also showed a charge-moment change insufficient to create optical emissions by the runaway electron models, which suggests that mechanisms not considered in these models may play a role in sprite production.

5.2 Suggestions for Further Work

5.2.1 Inhomogeneous VLF Propagation Modeling

While all of the measured sferic spectra presented in Chapter 3 could be explained on the basis of a homogeneous ionosphere, some observations were made which contain spectral details that cannot be reproduced with a homogeneous ionosphere. Figure

5.1 shows the average sferic spectrum and the average sferic waveform measured on July 24, 1996, from 0545–0600 UT, from discharges originating from 37.0–37.5°N and 99.3–99.6°W. The expected modal interference variations are present through the entire spectrum; however, there is a distinct drop in the amplitude of these variations near 4.2 kHz, and there is also a wide and deep null in the first mode at ~ 2.1 kHz. The average sferic waveform in Figure 5.1b shows a related effect; the individual ray-associated pulses disappear and reappear between 4.5 and 5.5 ms after the start of the sferic. Physically, these phenomena could both be produced by a strongly-absorbing ionospheric inhomogeneity over a small area of the path near (but not directly over) the source. The rays associated with paths undergoing reflection in the region of this inhomogeneity would be completely absorbed and not be seen at the receiver, while other rays would be undisturbed. Similarly, modes launched at a certain angle from the source would be most strongly absorbed by the inhomogeneity, resulting in the observed strong attenuation and the disappearance of the interference effects over a narrow frequency range. The existence of this feature in a 15 minute average waveform and spectrum from 36 individual sferics indicates that it is a persistent ionospheric perturbation. Observations made 1.5 hours earlier indicated no such inhomogeneity.

Spectral features such as this are not reproduced with a strongly inhomogeneous ionosphere with the FASTMC program, suggesting that effects ignored by FASTMC (such as mode reflection and ionospheric variations transverse to the propagation path) may be important in creating such features. Computer power and memory are rapidly approaching (if they have not yet arrived) the point at which VLF and ELF propagation can be solved with a finite-difference [Taflove, 1995] or finite-element [Jin, 1993] model which could easily include the effects ignored in the mode-theory model used in this work.

5.2.2 Sferic-Based Detection of Ionospheric Disturbances

With the right configuration of propagation paths and receivers, localized and transient ionospheric disturbances may be detectable using sferics. Such disturbances, caused by lightning-induced electron precipitation (LEP) [Inan, 1987], direct heating

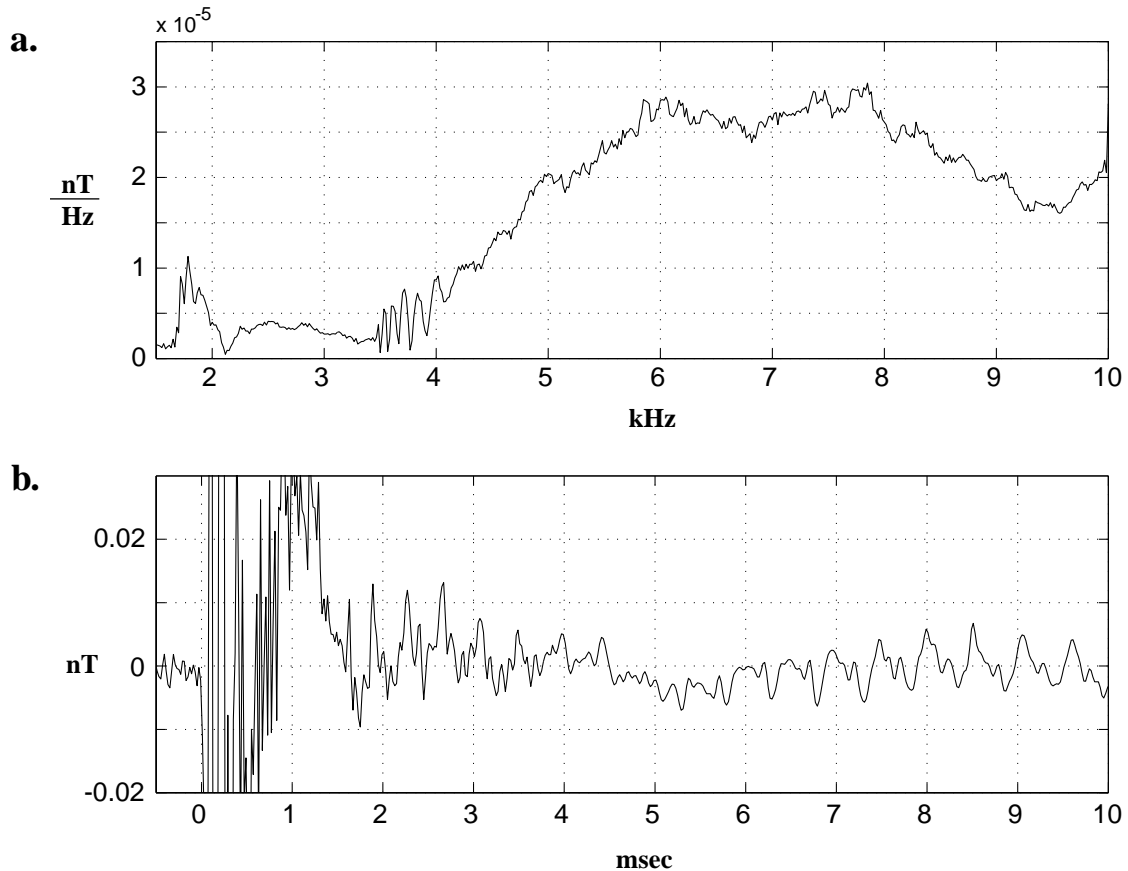


Figure 5.1: Sferic measurements which indicate a strongly inhomogeneous ionosphere. a: Average sferic spectrum. b: Average sferic waveform.

and ionization as a result of the electromagnetic pulse radiated by a lightning discharge [Taranenko *et al.*, 1993], or heating by high-power HF [Gurevich, 1978, p. 108] and VLF [Rodriguez and Inan, 1994] transmitters have been detected using narrow-bandwidth Navy VLF transmitters [Inan and Carpenter, 1987; Inan *et al.*, 1993; Bell *et al.*, 1995a; Inan *et al.*, 1992]. Since the source spectrum of an individual sferic is not known, propagation changes would be difficult to detect with sferics received at a single site. However, by comparing the propagation differences between a single sferic received at two different sites, the presence of a transient ionospheric perturbation over only one of the paths could be detected.

5.2.3 Fast Lightning Current Measurements

After the D region has been accurately inferred from an average VLF sferic spectrum, the average source current-moment spectrum can be extracted from the same observed spectrum. As discussed in Sections 3.3.3, such a measurement can be made (somewhat roughly) to match the broad variations of the observed VLF sferic spectra. With a more sophisticated approach to this problem, one should be able to produce reasonably accurate source current-moment spectra and waveforms from an average sferic or even an individual sferic. While this could perhaps be done using deconvolution to produce a completely general source waveform, a simpler measurement could be made by assuming a particular functional form for the source current-moment (such as that in Section 2.6.3) and varying the source parameters until good agreement is obtained. However, the extraction of physical lightning parameters (peak ground current, return stroke pulse velocity, etc.) from such a measurement would be strongly model-dependent.

5.2.4 E Region Ionospheric Measurements from ELF Sferics

As demonstrated in Chapter 4, ELF propagation is sensitive to electron densities at the E region peak near 110 km and in the E region valley near 150 km. Electron densities in these regions are difficult to measure with other radio techniques, especially on the large spatial scales possible using sferics.

By iteratively varying a parameterized model ionosphere in the ELF propagation model until the observations and model agree to a specified tolerance, E region electron densities could be inferred in much the same way as for the D region. Essentially the same technique was used in Section 4.3.2 to choose the proper ionosphere from which to calculate the model ELF impulse response. However, the IRI model [Rawer *et al.*, 1978] was used to produce the set of ionospheres, and experimentation has shown that some observations cannot be modeled using solely IRI-based ionospheres. Therefore an ionospheric parametrization spanning a larger set of possible ionospheres must be used. A good starting point for such an ionospheric model would be to connect smoothly a two parameter exponential D region to a gaussian-shaped E

region valley, with separate parameters defining the E region maximum and minimum electron densities, and perhaps even the altitude of this maximum and minimum.

To implement this method, the ELF propagation impulse response must be measured. In this work, we have estimated it from single sferics containing a large ELF component. However, a better signal-to-noise ratio can be achieved by using a similar averaging technique to that used in the D region measurements of Chapter 3. The ELF response depends much less strongly on propagation distance than does the VLF response, so a larger geographic area could be used for sferic collection. The VLF components would need to be filtered out after averaging to obtain the measured ELF impulse response.

5.2.5 More Refined D Region Measurements

It may be possible to extract more than two D region parameters from VLF sferic observations. In Figure 3.22, the observed and modeled spectra in the 16–20 kHz range disagree consistently in a way that would be improved by raising the ionosphere (thereby shifting the spectrum to the left). This change would, of course, destroy the good agreement from 3–14 kHz. However, Figure 3.7 shows that nighttime electron densities above $5 \times 10^2 \text{ cm}^{-3}$ have very little effect on frequencies above 12 kHz but do have a significant effect on lower frequencies. Thus a composite exponential profile with an effectively higher ionosphere for $N_e < 5 \times 10^2$ than for $N_e > 5 \times 10^2$ might be consistent with the VLF sferic observations over a wider frequency range. Sferic measurements over a wider bandwidth (~ 40 kHz) would help clarify the need for such a perturbation to the assumed exponential ionosphere.

Appendix A

Numerical Inverse Fourier Transform

The output of the spheric propagation model of Chapter 2 is a complex spectrum $G(f)$ defined only for positive frequencies. To convert this output to a time-domain waveform, a numerical scheme for calculating the inverse Fourier transform is needed.

The time-domain waveform $g(t)$ is defined through the inverse Fourier transform [*Bracewell*, 1986, p. 7] as

$$g(t) = \int_{-\infty}^{\infty} G(f) \exp(i2\pi ft) df \quad (\text{A.1})$$

$$= \int_{-\infty}^{\infty} \left[[G_r(f) + iG_i(f)] \cos(2\pi ft) + i[G_r(f) + iG_i(f)] \sin(2\pi ft) \right] df \quad (\text{A.2})$$

where $G_r(f)$ is the real part of $G(f)$ and $iG_i(f)$ is the imaginary part.

Since $G(f)$ is known only for positive frequencies, we make the reasonable assumption that $g(t)$ is strictly real (which it had better be if we hope to measure it). This implies that $G(f)$ has Hermitian symmetry (i.e. G_r is an even function and G_i is an odd function) [*Bracewell*, 1986, p. 14]. Because the infinite integral of a product of an even and an odd function must be zero, $g(t)$ can be rewritten as

$$g(t) = \int_{-\infty}^{\infty} [G_r(f) \cos(2\pi ft) - G_i(f) \sin(2\pi ft)] df. \quad (\text{A.3})$$

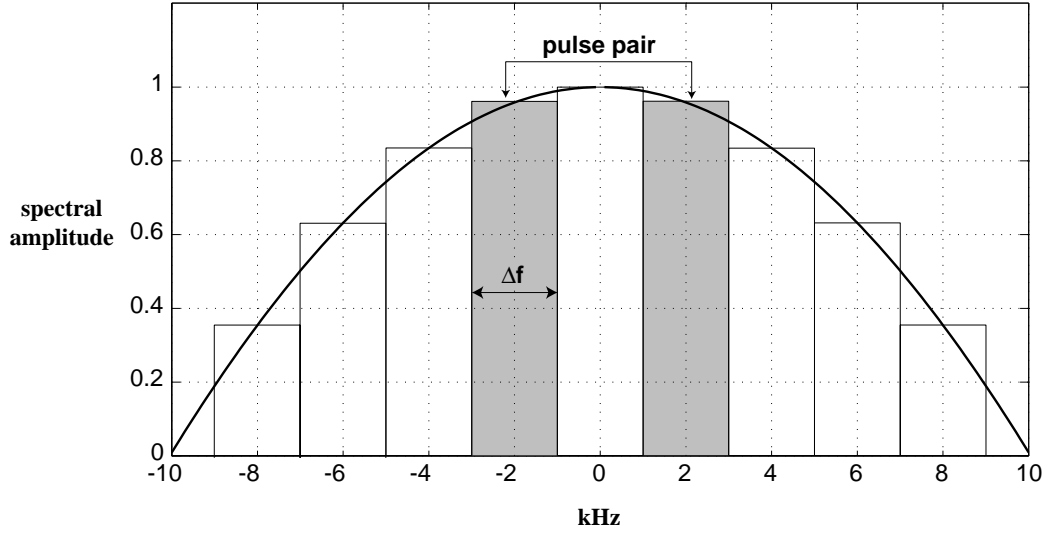


Figure A.1: Demonstration of approximation of smooth spectrum by a sum of piecewise-linear pulse pairs.

An efficient numerical method to evaluate this integral is as follows. Let $G_r(f)$ be approximated in a piecewise constant manner such as shown in Figure A.1, with Δf defining the width of the individual pieces. Since $G_r(f)$ is symmetric about $f = 0$ (an even function), the left hand term in the integral in (A.3) is the sum of the inverse Fourier transforms of individual pulse pairs like the one in Figure A.1 (except at $f = 0$ which will be treated separately).

The analytical inverse transform of such a pulse pair is given by

$$p_{rn}(t) = 2G_r(n\Delta f) \cos(2\pi n\Delta ft) \frac{\sin(\pi\Delta ft)}{\pi t}. \quad (\text{A.4})$$

At $f = 0$, there is only a single pulse whose transform is given by

$$p_{r0}(t) = G_r(0) \frac{\sin(\pi\Delta ft)}{\pi t}. \quad (\text{A.5})$$

Summing over all of the pulse pairs shows that

$$\int_{-\infty}^{\infty} G_r(f) \cos(2\pi ft) df \approx \frac{\sin(\pi\Delta ft)}{\pi t} \left[G_r(0) + 2 \sum_{n=1}^{\infty} G_r(n\Delta f) \cos(2\pi n\Delta ft) \right]. \quad (\text{A.6})$$

Since $G_i(f)$ is antisymmetric about $f = 0$ (an odd function), it can be approximated by a sum of antisymmetric pulse pairs with inverse Fourier transforms given by

$$p_{in}(t) = -2G_i(n\Delta f) \sin(2\pi n\Delta f t) \frac{\sin(\pi\Delta f t)}{\pi t}. \quad (\text{A.7})$$

Because $G_i(0)$ is odd, $G_i(0) = 0$ and $p_{i0} = 0$.

Putting this all together, and assuming a desired temporal sampling period for $g(t)$ of Δt , (A.3) can be approximated by

$$g(k\Delta t) \approx p_{r0}(k\Delta t) + \sum_{n=1}^{\infty} [p_{rn}(k\Delta t) + p_{in}(k\Delta t)] \quad (\text{A.8})$$

$$\begin{aligned} &\approx \frac{\sin(\pi\Delta f k\Delta t)}{\pi k\Delta t} \left[G_r(0) \right. \\ &\quad \left. + 2 \sum_{n=1}^{\infty} [G_r(n\Delta f) \cos(2\pi n\Delta f k\Delta t) + G_i(n\Delta f) \sin(2\pi n\Delta f k\Delta t)] \right]. \end{aligned} \quad (\text{A.9})$$

Equation (A.9) can be straightforwardly evaluated in this form for a completely arbitrary frequency spacing Δf and temporal sampling period Δt . Obviously, Δt must be chosen small enough to resolve accurately the fine temporal features in $g(t)$, Δf must be chosen small enough to resolve accurately all of the fine spectral features in $G(f)$, and the infinite summation must be truncated at a frequency above which the contribution to the sum is negligible.

However, the evaluation of this approximation can be made significantly faster by use of the Fast Fourier Transform (FFT) [Oppenheim and Schaffer, 1989, p. 514], defined for a sampled sequence x_n of length N by

$$X_k = \sum_{n=0}^{N-1} x_n \left[\cos\left(\frac{2\pi kn}{N}\right) - i \sin\left(\frac{2\pi kn}{N}\right) \right], \quad (\text{A.10})$$

which is nearly identical to the summation in (A.9) provided that $\Delta f\Delta t = N^{-1}$.

Thus (A.9) can be rewritten using the FFT as

$$g(k\Delta t) \approx \frac{\sin(\pi\Delta f k\Delta t)}{\pi k\Delta t} \left[-G_r(0) + 2 \sum_{n=0}^{N-1} [G_r(n\Delta f) \cos(2\pi nk/N) + G_i(n\Delta f) \sin(2\pi nk/N)] \right] \quad (\text{A.11})$$

$$\approx \frac{\sin(\pi\Delta f k\Delta t)}{\pi k\Delta t} \left[-G_{r0} + 2 \operatorname{Re}[\operatorname{FFT}(G_{rn})] + 2 \operatorname{Im}[\operatorname{FFT}(G_{in})] \right]. \quad (\text{A.12})$$

The parameter Δf is determined by the width of the spectral features in $G(f)$ and in this application must be <10 Hz. The parameter Δt must be chosen to resolve accurately the expected temporal features in the output waveform and must be $<20 \mu\text{s}$ for this application. This is equivalent to a 50 kHz sampling rate, which is sufficient to resolve the maximum frequency of ~ 22 kHz in this work. The total sampling time $N\Delta t$ must be long enough to contain all of the features of interest in the sferic (say >20 ms), and the total frequency width $N\Delta f$ must contain all of the frequency components of interest (say >25 kHz). If we choose $\Delta t = 10 \mu\text{s}$, and $\Delta f = 10$ Hz, then $N = 10^4$, $N\Delta t = 100$ ms, and $N\Delta f = 100$ kHz, which meets all of the criteria. Rather than use the propagation model to calculate the spectrum $G(f)$ to 100 kHz, $G(f)$ can be zero-padded to the proper length.

Bibliography

- [*Abramowitz and Stegun, 1972*] Abramowitz, M., and I. A. Stegun, *Handbook of Mathematical Functions*, Washington, DC: U.S. Government Printing Office, 1972.
- [*Arnold and Pierce, 1964*] Arnold, H. R., and E. T. Pierce, Leader and junction processes in the lightning discharge as a source of VLF atmospherics, *Radio Sci.*, *68D*, p. 771, 1964.
- [*Barkhausen, 1930*] Barkhausen, H., Whistling tones from the Earth, *Proc. IRE*, *18*, p. 1155, 1930.
- [*Barr, 1977*] Barr, R., The effect of sporadic-*E* on the nocturnal propagation of ELF waves, *J. Atmos. Terr. Phys.*, *39*, p. 1379, 1977.
- [*Bell et al., 1995a*] Bell, T. F., U. S. Inan, M. T. Danielson, and S. A. Cummer, VLF signatures of ionospheric heating by HIPAS, *Radio Sci.*, *30*, p. 1855, 1995a.
- [*Bell et al., 1995b*] Bell, T. F., V. P. Pasko, and U. S. Inan, Runaway electrons as a source of red sprites in the mesosphere, *Geophys. Res. Lett.*, *22*, p. 2127, 1995b.
- [*Berger, 1961*] Berger, K., Gewitterforschung auf dem Monte San Salvatore, *Elektrotechnik, Z-A82*, p. 249, 1961.
- [*Berger et al., 1975*] Berger, K., R. B. Anderson, and H. Kroninger, Parameters of lightning flashes, *Electra*, *80*, p. 23, 1975.

- [*Belrose and Burke*, 1964] Belrose, J. S., and M. J. Burke, Study of the lower ionosphere using partial reflection I: Experimental technique and method of analysis, *J. Geophys. Res.*, 69, p. 2799, 1964.
- [*Bernstein et al.*, 1996] Bernstein, R., R. Samm, K. Cummins, R. Pyle, and J. Tuel, Lightning detection network averts damage and speeds restoration, *IEEE Comp. App. Power*, 9, p. 12, 1996.
- [*Bickel et al.*, 1970] Bickel, J. E., J. A. Ferguson, and G. V. Stanley, Experimental observation of magnetic field effects on VLF propagation at night, *Radio Sci.*, 5, p. 19, 1970.
- [*Boccippio et al.*, 1995] Boccippio, D. J., E. R. Williams, S. J. Heckman, W. A. Lyons, I. T. Baker, and R. Boldi, Sprites, ELF transients, and positive ground strokes, *Science*, 269, p. 1088, 1995.
- [*Bracewell*, 1986] Bracewell, R. N., *The Fourier Transform and Its Applications*, New York: McGraw-Hill, 1986.
- [*Bracewell*, 1995] Bracewell, R. N., *Two-Dimensional Imaging*, Englewood Cliffs, N.J.: Prentice Hall, 1995.
- [*Bracewell et al.*, 1951] Bracewell, R. N., K. G. Budden, J. A. Radcliffe, T. W. Straker, and K. Weekes, The ionospheric propagation of long and very long radio waves over distances less than 1000 km, *Proc. Instn. Elect. Engrs.*, 98, p. 221, 1951.
- [*Brook et al.*, 1962] Brook, M., N. Kitagawa, and E. J. Workman, Quantitative study of strokes and continuing currents in lightning discharges to ground, *J. Geophys. Res.*, 67, p. 649, 1962.
- [*Bruce and Golde*, 1941] Bruce, C. E. R., and R. H. Golde, The lightning discharge, *J. Inst. Electr. Eng.*, 88, p. 487, 141.
- [*Budden*, 1961] Budden, K. G., *The Wave-Guide Mode Theory of Wave Propagation*, London: Logos Press, 1961.

- [Budden, 1962] Budden, K. G., The influence of the earth's magnetic field on radio propagation by wave-guide modes, *Proc. Roy. Soc. A*, 265, p. 538, 1962.
- [Budden, 1985] Budden, K. G., *The Propagation of Radio Waves*, Cambridge: Cambridge University Press, 1985
- [Burke and Jones, 1992] Burke, C. P., and D. L. Jones, An experimental investigation of ELF attenuation rates in the Earth-ionosphere duct, *J. Atmos. Terr. Phys.*, 54, p. 243, 1992.
- [Burke and Jones, 1996] Burke, C. P. and D. L. Jones, On the polarity and continuing currents in unusually large lightning flashes deduced from ELF events, *J. Atmos. Terr. Phys.*, 58, p. 531, 1996.
- [Burton and Boardman, 1933] Burton, E. T. and E. M. Boardman, Audio-frequency atmospherics, *Proc. IRE*, 21, p. 1476, 1933.
- [Chapman and Marcario, 1956] Chapman, F. W., and R. C. V. Marcario, Propagation of audio-frequency radio waves to great distances, *Nature*, 177, p. 930, 1956.
- [Chapman and Pierce, 1957] Chapman, J. and E. T. Pierce, Relations between the character of atmospherics and their place of origin, *Proc. IRE*, 45, p. 804, 1957.
- [Cheng, 1989] Cheng, D. K., *Field and Wave Electromagnetics*, Reading, Mass.: Addison-Wesley, 1989.
- [Cummer and Inan, 1997] Cummer, S. A., and U. S. Inan, Measurement of charge transfer in sprite-producing lightning using ELF radio atmospherics, *Geophys. Res. Lett.*, 24, p. 1731, 1997.
- [Cummer et al., 1997] Cummer, S. A., U. S. Inan, T. F. Bell, and C. P. Barrington-Leigh, ELF radiation produced by electrical currents in sprites, *Geophys. Res. Lett.*, in review, 1997.
- [Deeks, 1966] Deeks, D. G., D-region electron distributions in middle latitudes deduced from the reflection of long radio waves, *Proc. R. Soc. Lond. A*, 291, p. 413, 1966.

- [Dennis and Pierce, 1964] Dennis, A. S., and E. T. Pierce, The return stroke of the lightning flash to Earth as a source of VLF atmospherics, *Radio Sci.*, 68D, p. 777, 1964.
- [Eckersley, 1925] Eckersley, T. L., Musical atmospheric disturbances, *Phil. Mag.*, 49, p. 1250, 1925.
- [Evans, 1969] Evans, J. V., Theory and practice of ionosphere study by Thomson scatter radar, *Proc. IEEE*, 57, p. 496, 1969.
- [Ferguson and Snyder, 1980] Ferguson, J. A., and F. P. Snyder, Approximate VLF/LF mode conversion model, *Tech. Doc. 400*, Naval Ocean Systems Center, San Diego, Calif., 1980.
- [Ferguson et al., 1989] Ferguson, J. A., F. P. Snyder, D. G. Morfitt, and C. H. Shellman, Long-wave propagation capability and documentation, *Tech. Doc. 1518*, Naval Ocean Systems Center, San Diego, Calif., 1989.
- [Franz et al., 1990] Franz, R. C., R. J. Nemzek, and J. R. Winckler, Television image of a large electrical discharge above a thunderstorm system, *Science*, 249, p. 48, 1990.
- [Fraser-Smith and Helliwell, 1985] Fraser-Smith, A. C., and R. A. Helliwell, The Stanford University ELF/VLF Radiometer project: measurement of the global distribution of ELF/VLF electromagnetic noise, *Proc. 1985 IEEE Internat. Symp. Electromagnetic Compatability*, p. 305, 1985.
- [Fukunishi et al., 1996] Fukunishi, H., Y. Takahashi, M. Kubota, and K. Sakanoi, Elves: lightning-induced transient luminous events in the lower ionosphere, *Geophys. Res. Lett.*, 23, p. 2157, 1996.
- [Galejs, 1972] Galejs, J., *Terrestrial Propagation of Long Electromagnetic Waves*, Oxford: Pergamon Press, 1972.
- [Golub and Van Loan, 1989] Golub, G. H., and C. F. Van Loan, *Matrix Computations*, Baltimore: The Johns Hopkins University Press, 1989.

- [Gurevich, 1978] Gurevich, A. V., *Nonlinear Phenomena in the Ionosphere*, New York: Springer-Verlag, 1978.
- [Hargreaves, 1992] Hargreaves, J. K., *The Solar-Terrestrial Environment*, Cambridge: Cambridge University Press, 1992.
- [Hauser et al., 1969] Hauser, J. P., W. E. Garner, and F. J. Rhoads, A VLF effective ground conductivity map of Canada and Greenland with revisions from propagation data, *NRL Report 6893*, 1969.
- [Hayakawa et al., 1994] Hayakawa, M., K. Ohta, and K. Baba, Wave characteristics of tweek atmospherics deduced from the direction-finding measurement and theoretical interpretation, *J. Geophys. Res.*, *99*, p. 10733, 1994.
- [Hayakawa et al., 1995] Hayakawa, M., K. Ohta, S. Shimakura, and K. Baba, Recent findings on VLF/ELF sferics, *J. Atmos. Terr. Phys.*, *57*, p. 467, 1995.
- [Helliwell, 1965] Helliwell, R. A., *Whistlers and Related Ionospheric Phenomena*, Stanford, Calif.: Stanford University Press, 1965.
- [Hepburn, 1955] Hepburn, F., Atmospheric waveforms with very low-frequency components below 1 kc/s known as slow tails, *J. Atmos. Terr. Phys.*, *10*, p. 266, 1955.
- [Hines et al., 1965] Hines, C. O., I. Paghis, T. R. Hartz, and J. A. Fejer, Physics of the Earth's Upper Atmosphere, Englewood Cliffs, N.J.: Prentice Hall, 1965.
- [Horner and Clarke, 1955] Horner, F., and C. Clarke, Some waveforms of atmospherics and their use in the location of thunderstorms, *J. Atmos. Terr. Phys.*, *7*, p. 1, 1955.
- [Hubert et al., 1984] Hubert, P., P. Laroche, A. Eybert-Bernard, and L. Barret, Triggered lightning in New Mexico, *J. Geophys. Res.*, *89*, p. 2511, 1984.
- [Inan, 1987] Inan, U. S., Gyroresonant pitch angle scattering by coherent and incoherent whistler mode waves in the magnetosphere, *J. Geophys. Res.*, *92*, p. 127, 1987.

- [*Inan et al.*, 1997] Inan, U. S., C. P. Barrington-Leigh, S. Hansen, V. S. Glukhov, and T. F. Bell, Rapid lateral expansion of optical luminosity in lightning-induced ionospheric flashes referred to as ‘elves’, *Geophys. Res. Lett.*, *24*, p. 583, 1997.
- [*Inan and Carpenter*, 1987] Inan, U. S., and D. L. Carpenter, Lightning-induced electron precipitation events observed at L approximately 2.4 as phase and amplitude perturbations on subionospheric VLF signals, *J. Geophys. Res.*, *92*, p. 3293, 1987.
- [*Inan et al.*, 1993] Inan, U. S., J. V. Rodriguez, and V. P. Idone, VLF signatures of lightning-induced heating and ionization of the nighttime *D* region, *Geophys. Res. Lett.*, *20*, p. 2355, 1993.
- [*Inan et al.*, 1992] Inan, U. S., J. V. Rodriguez, S. Lev-Tov, and J. Oh, Ionospheric modification with a VLF transmitter, *Geophys. Res. Lett.*, *19*, p. 2071, 1992.
- [*Jean et al.*, 1960] Jean, A. G., W. L. Taylor, and J. R. Wait, VLF phase characteristics deduced from atmospheric wave forms, *J. Geophys. Res.*, *65*, p. 907, 1960.
- [*Jin*, 1993] Jin, J.-M., *The Finite Element Method in Electromagnetics*, New York: Wiley, 1993.
- [*Jones*, 1970] Jones, D. L., Electromagnetic radiation from multiple return strokes of lightning, *J. Atmos. Terr. Phys.*, *32*, p. 1077, 1970.
- [*Jones*, 1974] Jones, D. L., Extremely Low Frequency (ELF) ionospheric radio propagation studies using natural sources, *IEEE Trans. Comm.*, *22*, p. 477, 1974.
- [*Kane*, 1962] Kane, J. A., Re-evaluation of ionospheric electron densities and collision frequencies derived from rocket measurements of refractive index and attenuation, *J. Atmos. Terr. Phys.*, *23*, p. 338, 1962.
- [*Kim and Ling*, 1993] Kim, H., and H. Ling, Wavelet analysis of radar echo from finite-size targets, *IEEE Trans. Antennas Propagat.*, *41*, p. 200, 1993.

- [Kraus, 1992] Kraus, J., *Electromagnetics*, New York: McGraw-Hill, 1992.
- [Krehbiel et al., 1979] Krehbiel, P. R., M. Brook, and R. A. McCrory, An analysis of the charge structure of lightning discharges to ground, *J. Geophys. Res.*, *84*, p. 2432, 1979.
- [Kumar et al., 1994] Kumar, S., S. K. Dixit, and A. K. Gwal, Propagation of tweek atmospherics in the Earth-ionosphere waveguide, *Il Nuovo Cimento*, *17C*, p. 275, 1994.
- [Lehtinen et al., 1997] Lehtinen, N. G., T. F. Bell, V. P. Pasko, and U. S. Inan, A two-dimensional model of runaway electron beams driven by quasi-electrostatic thundercloud fields, *Geophys. Res. Lett.*, *in review*, 1997.
- [Lyons, 1996] Lyons, W. A., Sprite observations above the U.S. High Plains in relation to their parent thunderstorm systems, *J. Geophys. Res.*, *101*, p. 29641, 1996.
- [Mallinckrodt, 1949] Mallinckrodt, A. J., Relation of the ionosphere to the propagation of atmospherics, Engineer thesis, Stanford University, Stanford, Calif., 1949.
- [Mathews et al., 1982] Mathews, J. D., J. K. Breakall, and S. Ganguly, The measurement of diurnal variations of electron concentration in the 60–100 km ionosphere at Arecibo, *J. Atmos. Terr. Phys.*, *44*, p. 441, 1982.
- [Mechtly et al., 1967] Mechtly, E. A., S. A. Bowhill, L. G. Smith, and H. W. Knoebel, Lower ionosphere electron concentration and collision frequency from rocket measurements of Faraday rotation, differential absorption, and probe current, *J. Geophys. Res.*, *72*, p. 5239, 1967.
- [Milikh et al., 1995] Milikh, G. M., K. Papadopoulos, and C. L. Chang, On the physics of high altitude lightning, *Geophys. Res. Lett.*, *22*, p. 85, 1995.
- [Morfitt and Shellman, 1976] Morfitt, D. G., and C. H. Shellman, MODESRCH, An Improved Computer Program for Obtaining ELF/VLF/LF Mode Constants in an

Earth-Ionosphere Waveguide, *Interim Report 77T*, Naval Electronics Laboratory Center, San Diego, Calif., 1976.

[Narcisi, 1969] Narcisi, R. S., Discussion, in Meteorological and Chemical Factors in D-Region Aeronomy—Record of the Third Aeronomy Conference, *Aeronomy Rep. 34, Univ. of Illinois*, p. 284, 1969. Reproduced in *Handbook of Geophysics and the Space Environment*, Adolph S. Jursa, Ed., Air Force Geophysics Laboratory, Air Force Systems Command, U.S. Air Force, Springfield, VA, 1985, p. 21-55.

[Narcisi, 1971] Narcisi, R. S., Composition studies of the lower ionosphere, in *Physics of the Upper Atmosphere*, F. Verniani, Ed., Bologna, Italy: Editrice Compositori, 1971. Reproduced in *Handbook of Geophysics and the Space Environment*, Adolph S. Jursa, Ed., Air Force Geophysics Laboratory, Air Force Systems Command, U.S. Air Force, Springfield, VA, 1985, p. 21-56.

[Narcisi and Bailey, 1965] Narcisi, R. S., and A. D. Bailey, Mass spectrometric measurements of positive ions at altitudes from 64–112 kilometers, *J. Geophys. Res.*, *70*, p. 3687, 1965.

[Oppenheim and Schafer, 1989] Oppenheim, A. V., and R. W. Schafer, *Discrete-Time Signal Processing*, Englewood Cliffs, N.J. : Prentice Hall, 1989.

[Pappert, 1968] Pappert, R. A., A numerical study of VLF mode structure and polarization below an anisotropic ionosphere, *Radio Sci.*, *3*, p. 219, 1968.

[Pappert and Bickel, 1970] Pappert, R. A., and J. E. Bickel, Vertical and horizontal VLF fields excited by dipoles of arbitrary orientation and elevation, *Radio Sci.*, *5*, p. 1445, 1970.

[Pappert and Ferguson, 1986] Pappert, R. A., and J. A. Ferguson, VLF/LF mode conversion model calculations for air to air transmissions in the earth-ionosphere waveguide, *Radio Sci.*, *21*, p. 551, 1986.

- [Pappert and Moler, 1974] Pappert, R. A., and W. F. Moler, Propagation theory and calculations at lower extremely low frequencies (ELF), *IEEE Trans. Comm.*, *22*, p. 438, 1974.
- [Pappert and Moler, 1978] Pappert, R. A., and W. F. Moler, A theoretical study of ELF normal mode reflection and absorption produced by night-time ionospheres, *J. Atmos. Terr. Phys.*, *40*, p. 1031, 1978.
- [Pappert and Morfitt, 1975] Pappert, R. A., and D. G. Morfitt, Theoretical and experimental sunrise mode conversion results at VLF, *Radio Sci.*, *10*, p. 537, 1975.
- [Pasko et al., 1997] Pasko, V. P., U. S. Inan, T. F. Bell, and Y. N. Taranenkov, Sprites produced by quasi-electrostatic heating and ionization in the lower ionosphere, *J. Geophys. Res.*, *102*, p. 4529, 1997.
- [Phelps and Pack, 1959] Phelps, A. V., and J. L. Pack, Electron collision frequencies in nitrogen and in the lower ionosphere, *Phys. Rev. Lett.*, *3*, p. 340, 1959.
- [Pitteway, 1965] Pitteway, M. L. V., The numerical calculation of wave-fields, reflection coefficients and polarisations for long radio waves in the lower ionosphere I, *Phil. Trans. Royal Soc. Lond. A*, *257*, p. 219, 1965.
- [Press et al., 1986] Press, W. H., B. P. Flannery, S. A. Teukolsky, and W. T. Vetterling, *Numerical Recipes in FORTRAN: The Art of Scientific Computing*, Cambridge: Cambridge University Press, 1986.
- [Rafalsky et al., 1995] Rafalsky, V. A., A. V. Shvets, and M. Hayakawa, One-site distance-finding technique for locating lightning discharges, *J. Atmos. Terr. Phys.*, *57*, p. 1255, 1995.
- [Rairden and Mende, 1995] Rairden, R. L., and S. B. Mende, Time resolved sprite imagery, *Geophys. Res. Lett.*, *22*, p. 3465, 1995.
- [Rasmussen et al., 1980] Rasmussen, J. E., P. A. Kossey, and E. A. Lewis, Evidence of an ionospheric reflecting layer below the classical *D* region, *J. Geophys. Res.*, *85*, p. 3037, 1980.

- [Rawer, 1993] Rawer, K., *Wave Propagation in the Ionosphere*, Dordrecht: Kluwer Academic, 1993.
- [Rawer et al., 1978] Rawer, K., D. Bilitza, and S. Ramakrishnan, Goals and status of the International Reference Ionosphere, *Rev. Geophys. Space Sci.*, *16*, p. 177, 1978.
- [Reising et al., 1996] Reising, S. C., U. S. Inan, T. F. Bell, and W. A. Lyons, Evidence for continuing current in sprite-producing cloud-to-ground lightning, *Geophys. Res. Lett.*, *23*, p. 3639, 1996.
- [Richter, 1996] Richter, J. H., Application of conformal mapping to Earth-flattening procedures in radio propagation problems, *Radio Sci.*, *1*, p. 1435, 1966.
- [Rishbeth and Garriott, 1969] Rishbeth, H. and O. K. Garriott, *Introduction to Ionospheric Physics*, New York: Academic Press, 1969.
- [Rodriguez and Inan, 1994] Rodriguez, J. V., and U. S. Inan, Electron density changes in the nighttime *D* region due to heating by very-low-frequency transmitters, *Geophys. Res. Lett.*, *21*, p. 93, 1994.
- [Rodriguez et al., 1992] Rodriguez, J. V., U. S. Inan, and T. F. Bell, *D* region disturbances caused by electromagnetic pulses from lightning, *Geophys. Res. Lett.*, *19*, p. 2067, 1992.
- [Roussel-Dupre and Gurevich, 1996] Roussel-Dupre, R. A., and A. V. Gurevich, On runaway breakdown and upward propagating discharges, *J. Geophys. Res.*, *101*, p. 2297, 1996.
- [Ryabov, 1992] Ryabov, B. S., Tweek propagation peculiarities in the Earth-ionosphere waveguide and low ionosphere parameters, *Adv. Space Res.*, *12*, p. (6)255, 1992.
- [Schönland, 1956] Schönland, B. F. J., The lightning discharge, *Handbuch der Physik*, *22*, p. 576, 1956.

- [Sechrist, 1974] Sechrist, C. F. Jr., Comparisons of techniques for measurement of D-region electron densities, *Radio Sci.*, 9, p. 137, 1974.
- [Storey, 1953] Storey, L. R. O., An investigation of whistling atmospherics, *Phil. Trans. Roy. Soc. A*, 246, p. 113, 1953.
- [Stratton, 1941] Stratton, J. A., *Electromagnetic Theory*, New York: McGraw Hill, 1941.
- [Sukhorukov, 1992] Sukhorukov, A. I., On the excitation of the Earth-ionosphere waveguide by pulsed ELF sources, *J. Atmos. Terr. Phys.*, 54, p. 1337, 1992.
- [Taflove, 1995] Taflove, A., *Computational Electromagnetics: Finite-Difference Time-Domain Method*, Boston: Artech House, 1995.
- [Taranenko et al., 1993] Taranenko, Y. N., U. S. Inan, and T. F. Bell, Interaction with the lower ionosphere of electromagnetic pulses from lightning: heating, attachment, and ionization, *Geophys. Res. Lett.*, 19, p. 1815, 1993.
- [Taranenko and Roussel-Dupre, 1996] Taranenko, Y. N., and R. A. Roussel-Dupre, High altitude discharges and gamma-ray flashes: a manifestation of runaway air breakdown, *Geophys. Res. Lett.*, 23, p. 571, 1996.
- [Taylor, 1960] Taylor, W. L., VLF attenuation for east-west and west-east daytime propagation using atmospherics, *J. Geophys. Res.*, 65, p. 1933, 1960.
- [Teuber, 1993] Teuber, J., *Digital Image Processing*, New York: Prentice Hall, 1993.
- [Thomas and Harrison, 1970] Thomas, L., and M. D. Harrison, The electron density distributions in the D-region during the night and pre-sunrise period, *J. Atmos. Terr. Phys.*, 32, p. 1, 1970.
- [Thomson, 1993] Thomson, N. R., Experimental daytime VLF ionospheric parameters, *J. Atmos. Terr. Phys.*, 55, p. 173, 1993.

- [*Thottappillil et al.*, 1997] Thottappillil, R., V. A. Rakov, and M. A. Uman, Distribution of charge along the lightning channel: Relation to remote electric and magnetic fields and to return-stroke models, *J. Geophys. Res.*, *102*, p. 6987, 1997.
- [*Uman*, 1987] Uman, M. A., *The Lightning Discharge*, Orlando, Fla.: Academic Press, 1987.
- [*U. S. Naval Observatory Web Site*] U. S. Naval Observatory Sunrise/Sunset Computation, <http://tycho.usno.navy.mil/srss.html>
- [*Wait*, 1962] Wait, J. R., On the propagation of E.L.F. pulses in the Earth-ionosphere waveguide, *Canadian J. Phys.*, *40*, p. 1360, 1962.
- [*Wait*, 1970] Wait, J. R., *Electromagnetic Waves in Stratified Media*, Oxford: Pergamon Press, 1970.
- [*Wait and Spies*, 1964] Wait, J. R., and K. P. Spies, Characteristics of the Earth-ionosphere waveguide for VLF radio waves, *Tech. Note 300*, National Bureau of Standards, Boulder, Colo., 1964.
- [*Wait and Walters*, 1963] Wait, J. R., and L. C. Walters, Reflection of VLF radio waves from an inhomogeneous ionosphere part I: Exponentially varying isotropic model, *J. Res. Nat. Bureau Stand.*, *67D*, p. 361, 1963.
- [*Watt*, 1967] Watt, A. D., *VLF Radio Engineering*, Oxford: Pergamon Press, 1967,
- [*Weidman et al.*, 1986] Weidman, C. D., and E. P. Krider, The amplitude spectra of lightning radiation fields in the interval from 1 to 20 MHz, *Radio Sci.*, *21*, p. 964, 1986.
- [*Wilson*, 1925] Wilson, C. T. R., The electric field of a thundercloud and some of its effects, *Proc. Phys. Soc.*, *37*, p. 320, 1925.
- [*Winckler et al.*, 1996] Winckler, J. R., W. A. Lyons, T. E. Nelson, and R. J. Nemzek, New high-resolution ground-based studies of sprites, *J. Geophys. Res.*, *101*, p. 6997, 1996.

- [*Yamashita*, 1978] Yamashita, M., Propagation of tweek atmospherics, *J. Atmos. Terr. Phys.*, 40, p. 151, 1978.
- [*Yedemsky et al.*, 1992] Yedemsky, D. Ye., B. S. Ryabov, A. Yu. Shehokotov, and V. S. Yarotsky, Experimental investigation of the tweek field structure, *Adv. Space Res.*, 12, p. (6)251, 1992.
- [*Zauderer*, 1989] Zauderer, E., *Partial Differential Equations of Applied Mathematics*, New York: Wiley, 1989.